A Search for $H \rightarrow WW$ using a Matrix Element Discriminant and a WW Cross Section Measurement at ATLAS

Gemma Wooden
Jesus College, University of Oxford

Thesis submitted in partial fulfilment of the requirements for the degree of Doctor of Philosophy at the University of Oxford

Trinity Term, 2011

A Search for $H \rightarrow WW$ using a Matrix Element Discriminant and a WW Cross Section Measurement at ATLAS

Gemma Wooden, Jesus College, University of Oxford

Thesis submitted in partial fulfilment of the requirements for the degree of Doctor of Philosophy at the University of Oxford. Trinity Term, 2011

Abstract

One of the main motivating factors for the construction of the Large Hadron Collider (LHC) was the search for the Higgs boson, postulated to explain the origin of fundamental gauge boson masses. This thesis presents the results of the first search for the Higgs boson at the LHC, using 35 pb^{-1} of proton-proton collision data with a centre of mass energy of 7 TeV collected by the ATLAS experiment throughout 2010.

The search is performed in the $H \rightarrow WW$ channel, since the branching ratio for Higgs boson decays to W bosons is large for a wide range of Higgs boson masses. Two different search methods are presented: a straightforward cut-based method and a method using a matrix-element-based discriminant to provide additional separation between signal and background. The matrix element method is shown to give better expected sensitivity at all Higgs boson masses. Using these methods, a SM-like Higgs boson with a mass of 160 GeV with a production rate of 1.2 times the SM rate is excluded at 95% Confidence Level and limits are placed on the production rate of the SM Higgs boson in the range of masses from $120 < m_H < 200$ GeV.

In addition, a measurement of the SM WW cross section is performed. It is essential to understand this channel since it is the major background to the $H \rightarrow WW$ search. SM WW production is also sensitive to new physics processes, which would enhance its cross section. The SM WW cross section is measured to be $\sigma_{WW} = 40^{+20}_{-16}$(stat.)$\pm$7(syst.) pb, which is consistent with the NLO SM expectation of 46 ± 3 pb.

To Chris and Bill, my Mum and Dad.

Acknowledgements

I would like to take this opportunity to thank the Science and Technology Facilities Council for their financial support throughout my DPhil and, in particular, for giving me the opportunity to spend over two years at CERN.

My gratitude goes to my supervisor, Chris Hays, for his help and encouragement and for reassuring me when I had concerns. I would also like to the thank the rest of the Oxford ATLAS group for their help and the useful comments and ideas I received when presenting work at the weekly group meetings. I would especially like to thank Sinead Farrington for the useful discussions during the Oxford Higgs meetings. I am also very grateful for the help I received from the Oxford IT support team as well as James Ferrando for helping me get started with the grid. Many thanks also go to the wonderful team of secretaries: Sue Geddes, Kim Proudfoot and Laura Nevay, who were always very helpful.

Jesus College has supported me as both an undergraduate and a postgraduate so I am very grateful for the fabulous four course dinners which helped raise my spirits in times of need as well as the financial support which allowed me to spend a month working at Fermilab during my first year and to attend a workshop on LHC physics at Berkeley. It has been very reassuring knowing that my college advisor, Philip Burrows, has always been available if I had any concerns and I would particularly like to thank him for reading through my thesis at very short notice.

Since ATLAS is a collaboration of thousands, there have been many people along the way who have helped during the course of my DPhil. Steve McMahon and Koichi Nagai helped immensely during the course of my service work. I have worked in various different groups so I would like to thank the convenors of these groups for their guidance throughout my work: Bill Murray, Sandra Kortner and Ketevi Assamagan as Higgs convenors, Bruce Mellado and Bill Quayle as the $H \rightarrow WW$ subgroup convenors and Mohamed Aharrouche and Joao Guimaraes da Costa as electroweak convenors. I also found the support of Olya Igonkina and Brian Petersen, the trigger menu coordination convenors, essential throughout my term as Higgs trigger contact person.

I am very thankful to the entire WW and $H \rightarrow WW$ analysis teams for their useful comments and I would like to take the opportunity to thank a few individuals who were particularly helpful. Throughout the course of the WW cross section measurement, Marc-Andre Pleier was very patient, especially during the acceptance challenge, and very encouraging when I was finalising my results for the measurement so I thank him for that. Tatsuya Masubuchi and Aaron Armbruster helped enormously to get consistent results when undertaking the cut-based $H \rightarrow WW$ search so I thank them for that, as well as the many useful suggestions and discussions. It has been a pleasure working with all of you.

It would not have been possible to perform the matrix element based Higgs boson search without the invaluable help of Shih-Chieh Hsu, so I am extremely grateful to him for his support, advice and help. I am also very thankful to Daniel Whiteson who helped immeasureably when setting up this analysis at the very beginning. I would also like to thank Jianming Qian for his help in coordinating the $H \rightarrow WW$ multivariate-based effort as well as his many insightful comments throughout the course of these analyses.

My thanks go to the other Oxford ATLAS students, especially Aimee, Carly and James for the support in first year (and the wine and fondue in subsequent years). I also really appreciated the many lunch and tea breaks with Alex P, Alex D, Caterina, Chris B, Dan, David, Jacob, Lucy, Sam and Phil in my final year, which helped me retain my sanity. It would have been much less enjoyable without you this last year. I should also mention the physics help many of you gave me, which I am very thankful for as well.

I am also extremely grateful to the other UK LTA students I met while at CERN, for the useful physics discussions but also for the skiing and snowboarding, as well as the many beer o'clocks which made my time at CERN unforgettable.

I'm very thankful to my friends from home for always being there for me, being such fun to be around and for coming to visit me in Geneva (and not talking about computers!).

Finally, my deepest thanks go to my parents, without whom this would never have been possible. You have listened when I needed someone to talk to, advised me when I needed advice and supported me unquestioningly and I cannot express how grateful I am for everything you have done for me. I would also like to thank Alex for his unfailingly upbeat attitude and for always believing in me.

Preface

The ATLAS collaboration is made up of over 3000 people worldwide, including over 1000 graduate students. ATLAS is such a complex experiment that all these people are truly necessary to properly understand the data, operate and maintain the detector and produce physics results. I have tried to concentrate on the aspects of the measurements presented in this thesis that I performed myself but there are certain parts which other people have contributed to, and these have been referenced as far as possible.

I helped cross-check the WW and $H \rightarrow WW$ event selection with multiple members of the SM WW and $H \rightarrow WW$ analysis teams to ensure that each group member could completely reproduce all the numbers and distributions consistently, and to check that all the selections were applied in the same way.

For the SM WW cross section measurement, I determined the electron trigger scale factor and the event-based trigger scale factor myself. For this measurement, I also calculated the jet veto efficiency which was used to correct the calculation of the expected number of events from Monte Carlo.

Within the cut-based $H \rightarrow WW$ analysis, my focus was primarily on the VBF, $H+2j$, channel where I produced the Z+jets and top background estimates as well as all the final plots and numbers, which were used as inputs to the limit setting procedure. The results pf the $H \rightarrow WW$ search using the matrix element discriminant are entirely my own work, including the calculation of the discriminant, the estimation of systematic uncertainties and the limits on Higgs boson production.

Contents

List of Figures

List of Tables

Chapter 1

Introduction

The Standard Model of particle physics (SM) is an extremely successful theory. It has been probed extensively over the past 30 years and describes a whole range of phenomena with startling accuracy [1]. However, there are some questions to which it provides no answer. Among these are the abundance of matter with respect to antimatter in the universe, the origin of dark matter and whether there is an underlying unification of the fundamental forces of nature.

The origin of massive fundamental gauge bosons is one question the SM attempts to address. Within the SM, this arises from the interaction of particles with an underlying Higgs field, whose oscillations correspond to a particle known as the Higgs boson [2–7]. If it exists, this field causes spontaneous electroweak symmetry breaking, allowing certain particles to gain mass. Without the Higgs boson, or something similar, all particles in the SM would be massless, so it is clear that there must be some as-yet undiscovered mechanism that causes the symmetry breaking necessary for particles to gain mass. Thus, regardless of the outcome, the search for the Higgs boson will help elucidate the nature of electroweak symmetry breaking and the origin of massive gauge bosons.

Spontaneous electroweak symmetry breaking via the Higgs mechanism in the SM is only one hypothesis. Symmetry breaking via the Higgs mechanism would also occur if supersymmetry [8] is realised in nature and it is possible that it may proceed by other mechanisms entirely, such as technicolor [9].

The first step to understanding the true nature of electroweak symmetry breaking is the search for evidence of new physical particles, in the form of a SM Higgs boson or otherwise. This will constrain the possible mechanisms of symmetry breaking until one mechanism is identified as the true origin of massive gauge bosons. Of course, it may be that none of the current theories accurately describes the true nature of electroweak symmetry breaking. This would also be an exciting result, suggesting that a completely new view of the universe and its interactions is required.

The discovery of the Higgs boson was a major motivation for the construction of the Large Hadron Collider (LHC) and the ATLAS experiment. This thesis reports on the first data analysis aiming to discover or exclude the Higgs boson using the decay mode $H \rightarrow WW$ at ATLAS. In order to gain sensitivity to the Higgs boson and new physics processes, it is vital to understand the SM processes which may mimic their signatures. In particular, Higgs boson decays suffer from a range of SM backgrounds, each of which must be modelled correctly and measured with data where possible to ensure that any observed

excess of events is truly a signal of new physics. Therefore it is interesting to study SM WW production, since it is an irreducible background to $H \to WW$. This thesis includes a measurement of the cross section of WW production, which is also sensitive to new physics.

The ATLAS detector collected a dataset of 45 pb^{-1} of integrated luminosity at a centre of mass energy of 7 TeV during the course of 2010. The entirety of the dataset collected with the full working detector, corresponding to 35 pb^{-1} of integrated luminosity, is analysed in this thesis.

The structure is as follows: Chapter 2 describes the LHC and the ATLAS detector. The theoretical motivation for the Higgs boson is put into context in Chapter 3. Chapter 4 describes the selection of WW and $H \to WW$ events. The measurement of selection efficiencies and the determination of scale factors to correct the Monte Carlo (MC) simulated data so that it more accurately models the observed data is discussed in Chapter 5. The main backgrounds, and the methods used to estimate them, are detailed in Chapter 6. An in-depth discussion of the matrix element discriminant, which is used to select Higgs boson events, is provided in Chapter 7. The results of the WW cross section measurement and the search for the Higgs boson using a cut-based method are presented in Chapters 8 and 9 respectively. The results of the search for the Higgs boson using a matrix-element-based discriminant are discussed in Chapter 10. Finally, the conclusions which may be drawn from these studies, as well as ideas for future work, are discussed in Chapter 11.

Chapter 2

Experimental setup

The data used in this thesis were collected with the ATLAS experiment, a large general purpose particle detector based at the LHC, a proton-proton collider, at CERN near Geneva, Switzerland. This chapter provides an overview of the experimental setup, with a description of the LHC in Section 2.1 and the ATLAS detector itself in Section 2.2.

2.1 The Large Hadron Collider

The LHC is situated in the 27 km tunnel which the Large Electron Positron (LEP) collider occupied from 1989 to 2000. This tunnel straddles the French-Swiss border and lies between 45 m and 170 m underground. The LHC accelerates bunches of protons to 99.999999% of the speed of light and brings them to collision at the centres of four particle detectors, which are spaced around the ring. These detectors reconstruct the collision events and search amongst them for evidence of new physics, as well as using the data to perform detailed studies of physics processes which are already known.

There are four particle physics detectors based at the LHC: ALICE, ATLAS, CMS and LHCb, as shown in Figure 2.1. Of these, ATLAS and CMS are general purpose detectors, while ALICE and LHCb were designed with more specific aims in mind, respectively the study of the quark-gluon plasma which is postulated to have existed during the early universe using lead ion collisions and the decays of B hadrons in order to better understand the matter-antimatter asymmetry of the universe. All the experiments collect data supplied from the same beams within the LHC with the differences in their functionality arising solely from their different designs.

2.1.1 LHC design

The LHC consists of eight straight sections and eight arcs housing two separate rings of counter-rotating beams. To reduce costs, the LEP tunnel was used. Since LEP was an electron-positron machine which suffered from high synchroton radiation losses during the curved sections of the tunnel, the LEP tunnel required RF cavities in long straight sections to provide acceleration to compensate for these losses. The LHC, being a proton-proton collider, does not suffer from the same radiation losses and therefore would have benefitted from longer arced sections had costs allowed. However, the use of the LEP tunnel also had the advantage of allowing two of the underground caverns used for previous experiments

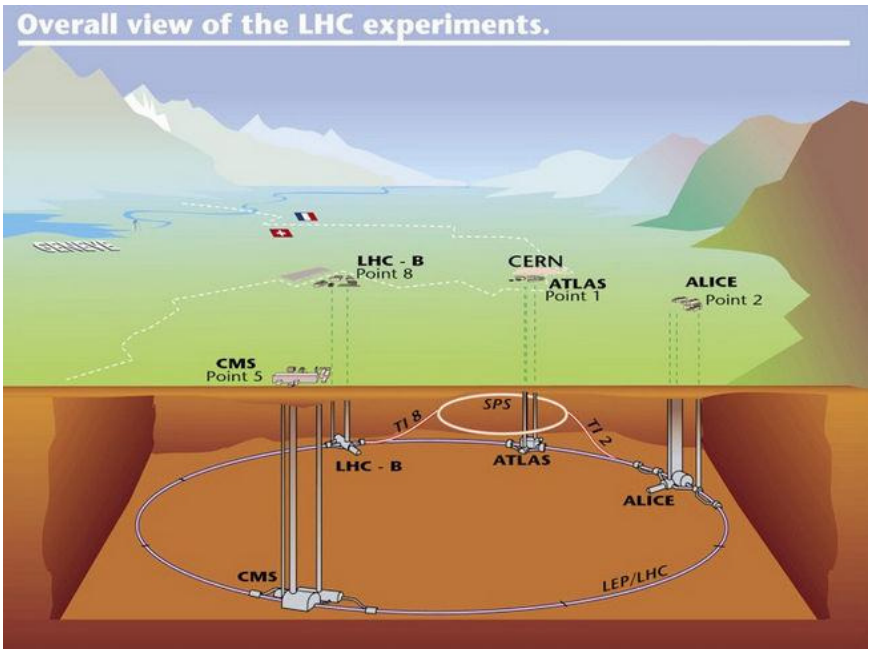

Figure 2.1: The LHC site with the positions of the four particle detectors shown [10], ATLAS Experiment © 2011 CERN.

to be re-used since the same crossing points are used at the LHC. The ATLAS and CMS detectors required new caverns due to their enormous size.

The energy of the particles is increased gradually before collisions occur. This is performed by a series of accelerators on the CERN site, as shown in Figure 2.2. Initially, 50 MeV protons are generated by the linear accelerator LINAC 2, which are then directed to the Proton Synchroton Booster (PSB) where they are accelerated to 1.4 GeV. At this stage, they are injected to the Proton Synchroton (PS) which further accelerates them to 26 GeV. The final stage before injection to the main ring of the LHC is the Super Proton Synchrotron (SPS) which accelerates the protons to 450 GeV. The LHC itself provides the final boost to the protons' energy, accelerating them until they reach the required centre of mass energy. The nominal LHC centre of mass energy is 14 TeV however, due to the various technical problems discussed in Section 2.1.2, the maximum centre of mass energy achieved so far is 7 TeV, with each beam having an energy of 3.5 TeV. Full details of the LHC design are given in Ref. [11].

The LHC was designed to provide sensitivity to processes with small production cross sections, such as SM Higgs boson production. This may be achieved by producing a large number of events per second, N, given by:

$$N = \mathcal{L}\sigma \tag{2.1}$$

where σ is the cross section for a given process. This equation shows that the number of events per second of a given type with cross section σ may be maximised by maximising the instantaneous luminosity $\mathcal{L}$. The luminosity depends solely on beam parameters and is given by:

$$\mathcal{L} = \frac{N_b^2 n_b^2 f_{rev} \gamma}{4\pi\epsilon_n \beta^*} F \tag{2.2}$$

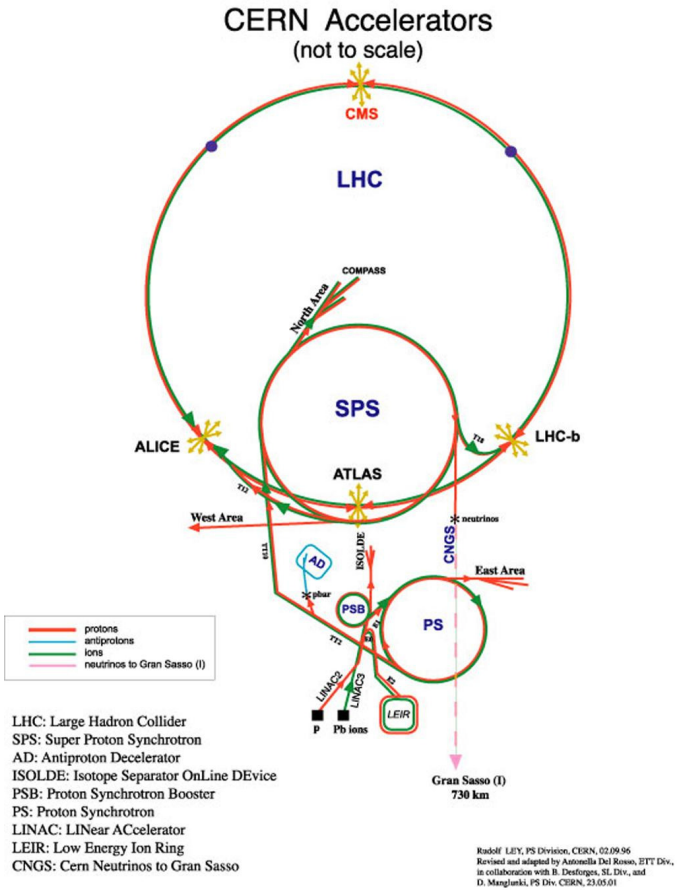

Figure 2.2: Accelerators used to achieve the 7 TeV centre of mass collision energy [12], ATLAS Experiment © 2011 CERN.

where N_b is the number of particles per bunch, n_b is the number of bunches per beam, f_{rev} is the revolution frequency, γ is the gamma factor for particles in the beam, ϵ_n is the beam emittance which gives a measure of how much the particles depart from the ideal trajectory, β^* is the beta function at the collision point giving the envelope for the particles' motion and F is the luminosity reduction factor due to the crossing angle at the interaction point. These parameters may all be controlled to maximise the instantaneous luminosity. At ATLAS, the peak luminosity is expected to reach 10^{34} cm^{-2}s^{-1} for proton beams although the highest luminosity achieved during the dataset used here is of the order 10^{32} cm^{-2}s^{-1}.

The protons are bunched together with a bunch spacing which varies with instantaneous luminosity. For the dataset used for this thesis, the bunch spacing used was 150 ns.

2.1.2 Timeline

It has taken many years to get from the conception of the LHC to the construction stage and finally to the current data-taking phase. The building of the LHC was initially approved in 1994 [13] in two stages: first at a centre of mass energy of 10 TeV with a planned upgrade to 14 TeV. After the procurement of additional funding from non-

member states, this plan was changed to involve one single building phase, with the LHC intended to run at 14 TeV right from the start. Unfortunately this was not to be.

Proton beams were successfully circulated around the main ring of the LHC for the first time on the 10th of September 2008. However, just 9 days later, there was a large helium leak into the tunnel believed to be due to a faulty electrical connection between neighbouring magnets which melted at high current and caused a mechanical failure [14]. Because of this, it was necessary to warm the damaged sector of the LHC up for repairs. At this time, additional protection systems were also put into place to ensure that this type of problem could not happen in the future. This process took most of 2009 and it was not until the 20th of November 2009 that beams were circulated again, with first collisions at 450 GeV occurring on the 23rd of November 2009.

From this point onwards, the beam energies were ramped up over a period of time until the 30th of March 2010, at which point the beam energies reached 3.5 TeV, creating a centre of mass energy of 7 TeV. Data were collected at 7 TeV from this point until November 2010, and it is this dataset which is analysed here.

Since November 2010, there has been a run with lead ions, which has already shown glimpses of interesting new phenomena [15] as well as a shutdown over the winter. Running began again on the 13th of March 2011 and is expected to continue until the end of 2012. The cumulative data recorded by ATLAS during 2010, which is used in this thesis, is shown in Figure 2.3.

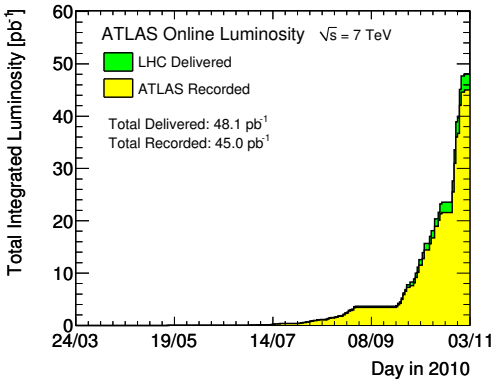

Figure 2.3: Cumulative luminosity delivered by the LHC and recorded by ATLAS during stable beams and *pp* collisions at a 7 TeV centre of mass energy during 2010 [16], ATLAS Experiment © 2011 CERN.

2.2 A Toroidal LHC Apparatus (ATLAS)

The design of the ATLAS detector has been performed with the objective of being able to undertake a wide range of different physics analyses, from SM measurements to searches for exotic new particles, the Higgs boson and supersymmetry. In order to be able to perform all of these measurements, the detector must be able to identify the full range of particles which may be produced in these interactions. This requires the ability to

reconstruct electrons, photons, muons, tau leptons, jets, b-jets and missing E_T from undetected neutrinos. When considering the components required for the ATLAS detector, the accurate identification of all these different objects has been the main aim to allow the full range of physics measurements to be performed with precision.

The detector must be able to identify particles from low energy, from particles produced in low mass B-hadron processes for example, to the very highest energy, as would be necessary to reconstruct leptons from heavy new gauge bosons such as W' and Z' if they exist. Hermeticity must be achieved as well, ensuring the maximum possible coverage and minimising the energy loss through crack regions. This not only improves the acceptance but also allows accurate calculation of any missing E_T which may be present in the event. To identify the decays of B-hadrons and tau leptons, as required by Higgs boson searches in multiple channels as well as many other measurements, excellent vertex detection must be ensured to allow secondary vertices to be identified with high efficiency.

Recognition of events containing interesting physics is performed using the ATLAS trigger system, which must make a decision very rapidly about whether the event should be stored. So that the rate at which data are stored is not too high, the trigger must provide the ability to identify low energy objects quickly, while providing good background rejection to remove events which are uninteresting.

In addition, the detector itself must be robust in an extremely radiation-heavy environment. There must also be a certain amount of in-built redundancy to ensure that data-taking can continue even if some parts of the detector are damaged or fail since warming the detector up to undertake repairs is extremely costly in terms of time.

2.3 The ATLAS coordinate system

The coordinate system used within the ATLAS experiment is described here and used throughout this thesis. The origin of the coordinate system is defined by the nominal interaction point with the beams defined as travelling in the z-direction. The y-axis points upwards from the beam direction, away from the centre of the earth, while the x-axis is defined as pointing towards the centre of the LHC ring.

The angular coordinates are defined as follows. The azimuthal angle, ϕ, is measured in the x-y plane and the polar angle, θ, is between the z-axis and the x-y plane. This gives the following relations:

$$\begin{aligned} \phi &= \tan^{-1}(x/y) \\ \theta &= \tan^{-1}(\sqrt{x^2+y^2}/z) \end{aligned} \tag{2.3}$$

A further angular quantity known as pseudorapidity, η, is defined as:

$$\eta = -\ln[\tan(\theta/2)] \tag{2.4}$$

The transverse momentum of particles, p_T, a quantity which is used throughout to select energetic objects which are likely to have originated from interactions with high momentum transfer is defined using:

$$p_T = \sqrt{p_x^2 + p_y^2} = |p| \sin\theta \tag{2.5}$$

The transverse energy E_T may be similarly defined as $E_T = E \sin\theta$.

In addition, the η-ϕ distance between particles, ΔR, is calculated as:

$$\Delta R = \sqrt{\Delta\phi^2 + \Delta\eta^2} \tag{2.6}$$

where $\Delta\phi$ and $\Delta\eta$ are respectively the ϕ and η differences between the particles. This quantity is often used to remove overlap between objects, as sometimes the same object may be reconstructed as multiple different particle types.

2.4 Structure of the ATLAS detector

A cut-away view of the ATLAS detector is shown in Figure 2.4. The detector is 25 m high and has a length of 44 m, occupying a cavern the size of a cathedral. The performance goals of the ATLAS detector are shown in Table 2.1. A detailed description of the ATLAS detector may be found in Ref. [17].

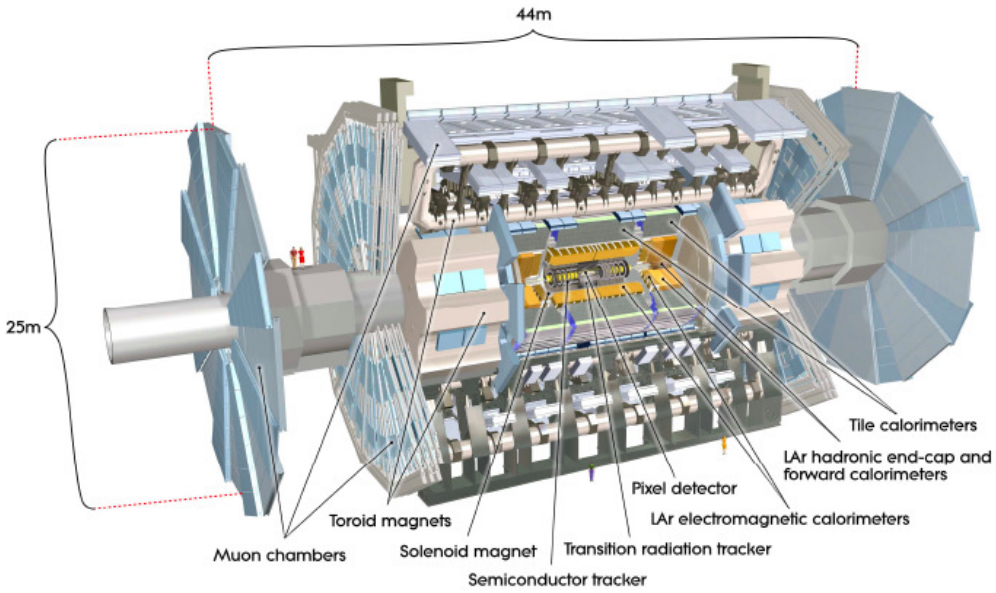

Figure 2.4: The ATLAS detector [17].

The magnetic field structure of the ATLAS detector is an important aspect of its design. The inner detector is surrounded by a superconducting solenoid which produces a field of 2 T. Particle tracking is performed by the inner detector, through pattern recognition to measure p_T and trajectory. Outside the inner detector lie the electromagnetic and then the hadronic calorimeters which measure the deposited energy. Further beyond this lies the muon spectrometer which measures momentum and energy of particles within a toroidal magnetic field.

2.4.1 Inner detector

The function of the inner detector (ID) is primarily to provide excellent momentum resolution and precision pattern recognition, providing the ability to reconstruct both primary

Detector component	**Target resolution**	$\lvert\eta\rvert$ **coverage**	
		Measurement	Trigger
ID tracking	$\sigma_{p_T}/p_T = 0.05\%\ p_T \oplus 1\%$	< 2.5	
EM calorimetry	$\sigma_E/E = 10\%/\sqrt{E} \oplus 0.7\%$	< 3.2	< 2.5
Hadronic calorimetry (jets)			
Barrel and endcap	$\sigma_E/E = 50\%/\sqrt{E} \oplus 3\%$	< 3.2	< 3.2
Forward	$\sigma_E/E = 100\%/\sqrt{E} \oplus 10\%$	$3.1 < \lvert\eta\rvert < 4.9$	$3.1 < \lvert\eta\rvert < 4.9$
Muon spectrometer	$\sigma_{p_T}/p_T = 10\%$ at $p_T = 1$ TeV	< 2.7	< 2.4

Table 2.1: Performance goals of the ATLAS detector [17]. Energy and momentum are given in GeV unless otherwise stated.

and secondary vertices. Charged particles within the region $|\eta| < 2.5$ leave 'hits' as they traverse the ID. Multiple hits may be joined up to reconstruct the path of a charged particle through the volume of the ID, from which the momentum and origin of the particle may be calculated. In order to accurately reconstruct these charged particle tracks, fine granularity detectors are required. Within ATLAS, pixel and silicon microstrip tracking detectors, as well as the transition radiation tracker (TRT), are used to achieve the required accuracy. The structure of the inner detector is shown in Figure 2.5.

The highest precision measurements are performed by the silicon **pixel detector** which lies closest to the beam pipe. It consists of three layers parallel to the beam within the central (barrel) region and three disks perpendicular to the beam lying in the forward (endcap) region and reads out over 80 million channels. These individual channels (or 'pixels') are arranged into 1744 pixel modules, which measure on average three hits per track within $|\eta| < 2.5$. Each module is around 250 μm thick and consists of 47232 pixels. When charged particles traverse a pixel, electron-hole pairs proportional to the energy loss are created. The pixel sensors operate at a bias voltage of 150 V, which causes separation of the pairs before they have the chance to recombine, inducing a current which may be amplified and compared to a given threshold. If this signal lies above the threshold, a hit is recorded along with a time stamp and the location of the pixel.

Lying immediately outside the pixel detector is the **semiconductor tracker (SCT)** which consists of silicon strips. As a charged particle crosses the SCT, eight strip layers corresponding to four space-points are crossed by each track. The eight strip layers are arranged into four double layers, with one at a stereo angle of 40 mrad with respect to the other, at a pitch of 80 μm. This allows the determination of the precise position of the hit within the strip. The SCT has a total of 6.3 million readout channels.

The final part of the ID is the **transition radiation tracker (TRT)**. This is made up of cylindrical drift tubes (straws) with a diameter of 4 mm interleaved with radiators and provides coverage up to $|\eta| < 2$. It utilises the principles of transition radiation (TR), whereby radiation is emitted when relativistic charged particles cross a boundary between media with differing dielectric constants. Since electrons are highly relativistic, they have a high probability of creating TR. This may be used to improve the identification of electrons since other more massive particles, for example pions, are generally less relativistic and hence emit less TR. In addition, as charged particles cross the straws, they ionise the gas within them, generating an electric signal which may be used for tracking. For track

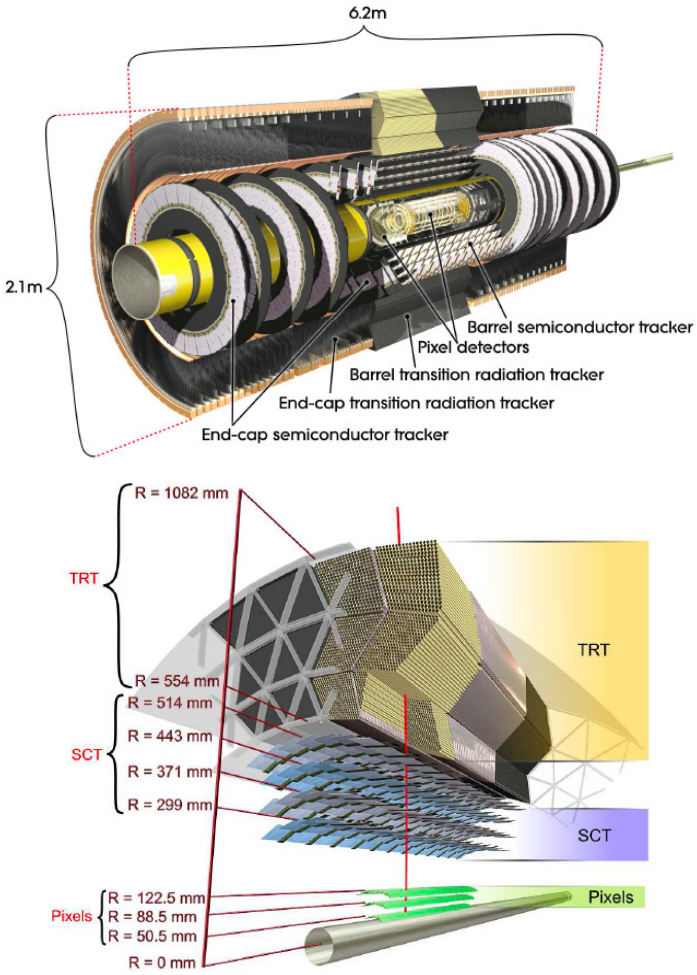

Figure 2.5: The ATLAS inner detector [17].

reconstruction, this ionisation is more important than the transition radiation which is produced. The readout of the TRT comprises two discriminators: one acting at a low threshold to detect ionisation and one acting at a high threshold to identify transition radiation. In addition, a measurement of the drift-time is made which may be used to separate ionising radiation, which has a long drift-time, from transition radiation. Within the barrel, the straws lie parallel to the beam while in the endcaps the straws are arranged radially, in wheels. Whereas the pixels and SCT provide measurements in both the $R-\phi$ and z directions, the TRT measures positions in the $R-\phi$ plane and is around 10 times less accurate than the pixels and SCT. However, as the straws are arranged to give up to 36 hits per track, the large number of hits compensates for the lack of intrinsic precision, ensuring that the TRT contributes significantly to momentum measurement.

2.4.2 Calorimeters

The ATLAS calorimeters cover the range $|\eta| < 4.9$ and provide precise measurement of the energy of electrons, photons and hadrons using an electromagnetic calorimeter for electron and photon reconstruction and a hadronic calorimeter to improve the measurement of jets

and missing E_T. A forward calorimeter (FCal) is used for particles at $3.1 < |\eta| < 4.9$. The structure of the calorimeter system is shown in Figure 2.6.

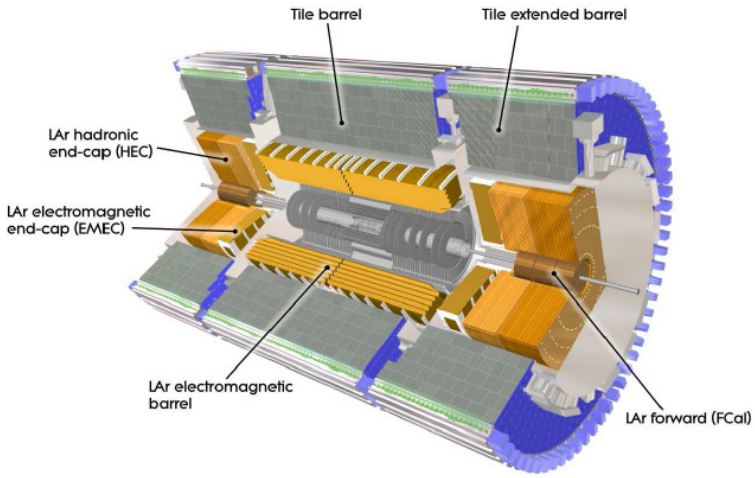

Figure 2.6: The ATLAS calorimeters [17].

All of the ATLAS calorimeters are sampling calorimeters and work using the same principle. Sampling calorimeters separate the functions of particle absorption and signal readout; their structure consists of sheets of absorbers alternated with layers of active material to perform the energy measurement. When a particle is incident on the calorimeter, it produces a shower of particles. At each stage in the showering, the particles have less and less energy until finally the shower is completely absorbed. As this process occurs, energy is deposited within the calorimeter which may be summed to provide a measurement of the initial particle's energy. The calorimeter is designed to completely absorb incident particles to ensure that the full particle energy is deposited within the calorimeter so that no energy is lost by escaping particles. This also helps reduce radiation damage to the muon chambers which may be caused if it was bombarded by many high energy hadrons. Only the fraction of shower energy absorbed in the active material is measured so, in order to get back to the correct incident energy, it is vitally important that the calorimeter system is properly calibrated.

The first part of the calorimeter system is the **liquid argon (LAr) electromagnetic (EM) calorimeter**, which is targeted to accurately measure the energy of incoming electrons and photons. It provides coverage up to $|\eta| < 3.2$ and is split into a barrel part within $|\eta| < 1.475$ and two endcap parts for the remaining coverage. The active material within the calorimeter is liquid argon, while lead provides the absorption. The thickness of lead in the absorber plates has been optimised as a function of $|\eta|$ to provide the best energy resolution. Accordion-shaped geometry is used to provide complete coverage in ϕ with no cracks. Within the central region of $|\eta| < 1.8$, the energy lost by electrons and photons before reaching the calorimeter is corrected for by using a presampler detector consisting of an active LAr layer.

Directly outside the EM calorimeter are the **hadronic calorimeters**, which are designed to determine the energy of hadrons. The hadronic calorimeters consist of the tile

calorimeter which uses steel as the absorber and scintillating tiles as the active material and covers $|\eta| < 1.7$. Additional coverage up to $|\eta| < 3.2$ is provided by the LAr hadronic endcap calorimeter which is constructed from the same materials as the EM calorimeter. Further coverage in the very forward region is given by the LAr forward calorimeter which also uses the same technology as the EM calorimeter and extends to $|\eta| < 4.9$.

2.4.3 Muon system

The structure of the muon system is shown in Figure 2.7. Within the muon spectrometer, measurements of muon momentum are performed utilising the deflection of muon tracks within the magnetic field provided by the large barrel toroid in $|\eta| < 1.4$, by two smaller endcap magnets in $1.6 < |\eta| < 2.7$ and by a combination of both fields in the transition region of $1.4 < |\eta| < 1.6$. Particle hit positions are measured in the barrel region by chambers arranged in three cylindrical layers; in the transition and endcap regions, the chambers lie perpendicular to the beam and are also in three layers. Pattern recognition algorithms are applied to these hits to reconstruct tracks. Monitored drift tubes (MDTs) are used to precisely measure the hit positions for particles with $|\eta| < 2$ in the innermost layer and $|\eta| < 2.7$ in all the other layers. Cathode strip chambers (CSCs) consisting of multiwire proportional chambers with cathodes split into strips with higher granularity provide additional coverage for $2 < |\eta| < 2.7$.

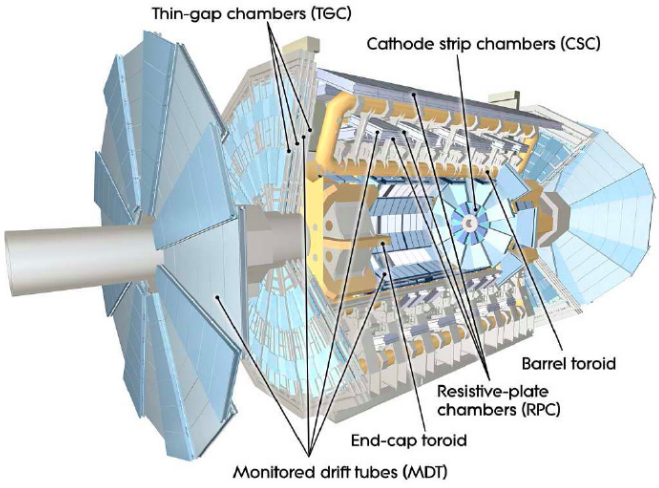

Figure 2.7: The ATLAS muon system [17].

2.5 The ATLAS trigger system

The bunch crossing rate at ATLAS is higher than at any previous collider at around 40 MHz. Most of these crossings result in uninteresting processes with low momentum transfer which do not merit further study; it is not sensible or feasible to store these events. The ATLAS trigger system has been designed to reduce the rate from 40 MHz to a much more manageable 200 Hz. To do this, the trigger searches for evidence of

interesting physics processes such as the production of high-p_T leptons, jets, tau leptons or large missing E_T. If nothing of interest is found by the trigger, the event is discarded.

The ATLAS trigger system consists of three stages, shown in Figure 2.8: the hardware-based Level 1 (L1) trigger and the software-based Level 2 (L2) and Event Filter (EF) triggers, with L2 and EF triggers referred to collectively as the High Level Trigger (HLT).

The L1 trigger selects events containing specific physics objects, with the regions of the detector containing these interesting objects known as regions of interest (RoIs). For events with electromagnetic clusters, the E_T is measured at L1 by trigger towers in a region of 0.1×0.1 in $\Delta\eta \times \Delta\phi$. These towers are shown in Figure 2.9, which is discussed in more detail in Section 2.6.2.

The L1 muon trigger utilises a measurement of particle trajectories made by two parts of the muon detector: the resistive plate chambers (RPCs) in the barrel region and the thin gap chambers (TGCs) in the endcap region. The L1 muon trigger uses different detectors from the offline muon detectors. This is because the L1 trigger must rapidly make a decision about whether an event should be stored or discarded and the MDTs and CSCs used for offline muon reconstruction are not fast enough for this purpose. They are, however, extremely precise, which is exactly what is desired for the offline muon reconstruction. The RPCs and TGCs used for the L1 muon trigger are less accurate, but provide a precision which is adequate for trigger purposes and are, crucially, fast enough to cope with the high bunch crossing rate.

The RoIs identified by the L1 trigger are used to seed the L2 trigger. Events passing the L2 trigger are passed to the EF trigger, which performs a full offline analysis to accurately select events containing the physics objects of interest. At L2 and EF, further requirements on the E_T of the objects must be satisfied and electron candidates must pass additional quality criteria.

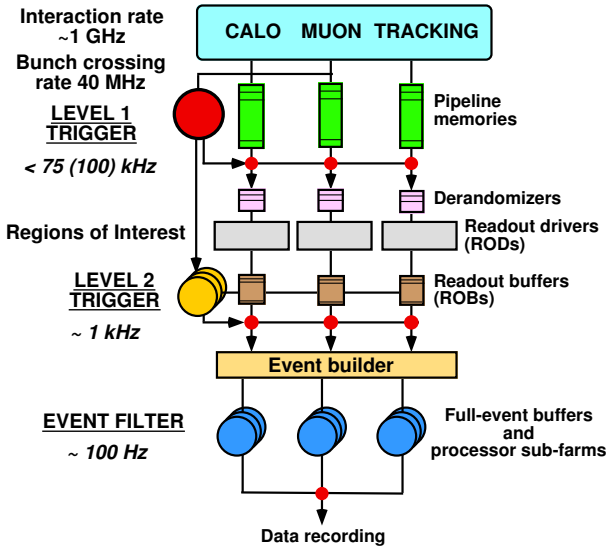

Figure 2.8: The ATLAS trigger system [18], ATLAS Experiment © 2011 CERN.

2.6 Event reconstruction

The measurements performed by the ATLAS detector as described in the previous sections produce raw electrical signals which must be processed in order to reconstruct the objects required for physics analysis, including tracks, particles, missing E_T and vertices. This section describes the methods used to reconstruct these objects from the raw data obtained by the ATLAS detector.

2.6.1 Track reconstruction

The reconstruction of tracks at ATLAS is performed using data obtained by the inner detector described in Section 2.4.1. Reconstruction occurs in three steps:

- Raw data from the pixel and SCT detectors are converted into clusters and then space-points. Timing information from the TRT is converted into calibrated drift circles.
- The next stage involves running various track-finding algorithms with the aim of finding tracks arising from the interaction region. Space-points from the three pixel layers and the first SCT layer are combined to form track seeds. These seeds are then extended, outliers are removed and fake tracks are rejected by applying various quality cuts. Then, these track candidates are extended into the TRT and a final refitting using information from the pixels, SCT and TRT is performed to reconstruct the tracks. The converse strategy, extending TRT tracks back into the SCT and pixel detectors is used in addition to search for tracks arising from particles which may not necessarily have been produced at the primary vertex such as those produced by the decay of long-lived particles.
- Once these tracks have been reconstructed, a vertex finding algorithm is used to reconstruct the primary vertices in the event.

2.6.2 Electron reconstruction

Electrons traversing the LAr calorimeter, described in Section 2.4.2, deposit their energy in calorimeter cells. The energy deposited in these various cells must be summed to give a total measurement of the electron's energy. This is done using clustering algorithms. At ATLAS, the 'sliding window' algorithm [19] is used.

The first step of this algorithm is to divide the η-ϕ space of the EM calorimeter into a grid of $N_\eta \times N_\phi$ 'tower' elements with size $\Delta\eta \times \Delta\phi = 0.025 \times 0.025$ as indicated in Figure 2.9. The transverse energy of each cell within an element is summed to give a tower E_T. A window with fixed size $N_\eta^{window} \times N_\phi^{window} = 5 \times 5$ in units of tower size is moved across each element of the tower grid in steps of $\Delta\eta$ and $\Delta\phi$. If the window E_T, defined as the vector sum of the E_T of the towers within the window is larger than the threshold value of 3 GeV and is a local maximum, a precluster is formed.

Seeds are formed from these preclusters, with electromagnetic clusters centred on these seeds. The clusters contain the energy deposited within a window size which depends on the hypothesized particle type and the location of the seed. The window sizes used for

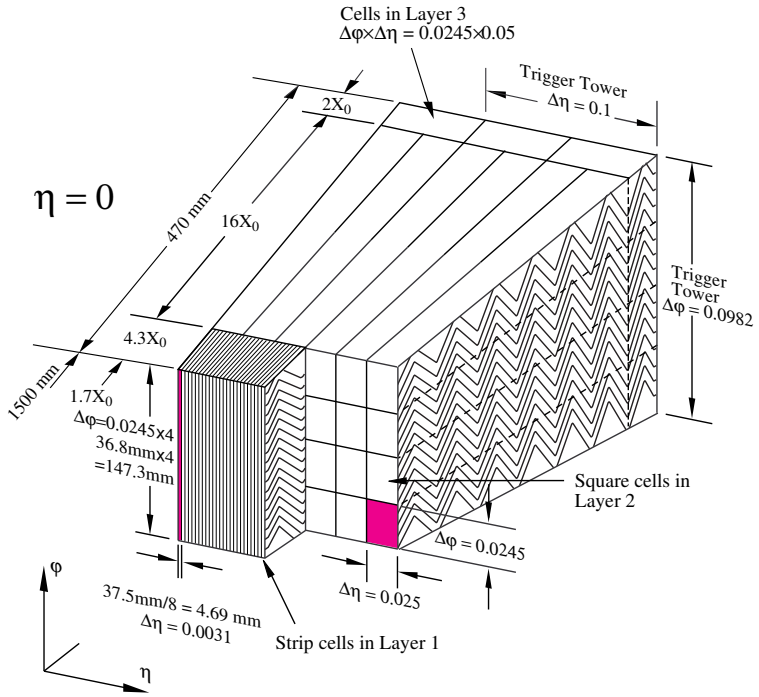

Figure 2.9: Diagram showing the structure of a barrel module of the electromagnetic calorimeter. An electromagnetic trigger tower is shown as shaded, with its η and ϕ dimensions indicated [17].

different particle types are shown in Table 2.2. The windows are larger in the ϕ direction in the barrel for electrons and photon conversions, which produce electron-positron pairs, than for unconverted photons due to the curvature of the charged electrons and positrons in the magnetic field which causes their energy to be deposited in a larger ϕ region. The effect of the magnetic field is smaller in the endcaps, therefore all the particle types have the same window size in this region.

Particle type	Barrel	Endcap
Electron	3×7	5×5
Converted photon	3×7	5×5
Unconverted photon	3×5	5×5

Table 2.2: Sizes of sliding windows used in electron and photon reconstruction in terms of $N_{\eta}^{window} \times N_{\phi}^{window}$, where $\Delta\eta \times \Delta\phi = 0.025 \times 0.025$ gives the dimensions of $N_{\eta}^{window} \times N_{\phi}^{window} = 1 \times 1$.

Finally, corrections are applied to account for various effects including the ϕ-dependence of the amount of absorber material traversed by incident particles, the finite granularity of the cells and the possibility that the shower is not entirely contained within the cluster window.

To identify electromagnetic clusters as arising from electrons rather than photons, matching is performed between the electromagnetic cluster and inner detector tracks. If $\Delta\eta < 0.5$ and $\Delta\phi < 0.1$ between a track and cluster, the cluster is considered matched

and is therefore identified as an electron candidate. This has the effect of suppressing the incorrect reconstruction of photons as electrons although there may be cases where converted photons are identified as electron candidates. In these cases, the application of further identification criteria at the trigger and offline stages, tailored to select electrons arising from high momentum transfer processes rather than those originating from photon conversions, help separate converted photons from primary electron candidates.

2.6.3 Muon reconstruction

There are multiple ways in which muons may be reconstructed at ATLAS. These are described below.

- Standalone muons produce tracks solely in the muon spectrometer, which is described in Section 2.4.3. These tracks are formed from track segments in various parts of the muon spectrometer which are linked together. The tracks are extrapolated back to the beam line so that the initial momentum and energy of the muon may be calculated, accounting for multiple scattering and energy loss as the muon traverses the inner detector and calorimeters in order to give an accurate measurement.

- Inner detector muons produce tracks solely in the inner detector. These tracks are reconstructed using the method described in Section 2.6.1.

- Combined muons are formed from the combination of inner detector and muon spectrometer muons. This combination is performed using a statistical combination algorithm, Staco [20], which calculates the match χ^2 to determine if the match between the standalone and inner detector muon candidate tracks is significant enough to identify the candidate as a combined muon. If so, the inner detector and muon spectrometer tracks are combined to form a combined muon track. Combined muons are used in this thesis.

2.6.4 Jet reconstruction

Jets at ATLAS may be reconstructed in different ways as long as the following theoretical constraints are satisfied:

- **Infrared safety:** Additional low p_T radiation between high p_T jets or, conversely, lack of such radiation between jets, should not affect the reconstruction of the jets.

- **Collinear safety:** A jet should be reconstructed in the same way regardless of whether it remains as one jet or splits into more jets.

In addition, the jet algorithm should not depend on the exact detector geometry, should be highly efficient and the same underlying process should be reconstructed equally well at parton level, particle level or detector level.

Bearing these considerations in mind, the jet algorithm used here is the anti-k_T algorithm [21–23]. This is a type of sequential recombination algorithm. A quantity d_{ij} is calculated for all possible pairs of input objects:

$$d_{ij} = min(1/p_{T,i}^2, 1/p_{T,j}^2)\frac{\Delta R_{ij}^2}{R^2} = min(1/p_{T,i}^2, 1/p_{T,j}^2)\frac{\Delta\eta_{ij}^2 + \Delta\phi_{ij}^2}{R^2} \tag{2.7}$$

where $p_{T,i}$ is the transverse momentum of object i and R is a fixed cone size (chosen to be 0.4 for this thesis). A further d_i is calculated as $d_i = 1/p_{T,i}^2$. d_{ij} and d_i are calculated for all objects and the minimum, d_{min}, is found. If $d_{min} = d_{ij}$, objects i and j are combined into a new object. However, if $d_{min} = d_i$, object i is considered to be a jet and is removed from the list of objects. This process continues until all objects are combined into jets. Therefore, all the objects from the initial list are either combined together to form jets or are already considered to be a jet. This procedure is entirely infrared and collinear safe, unlike other jet algorithms.

This algorithm may be understood more intuitively by considering certain cases. If an event has a few well-separated high-p_T particles as well as many low-p_T particles, the d_{1j} between a high-p_T particle 1 and a low-p_T particle j depends on the p_T of particle 1 and the ΔR separation of the particles. For two low-p_T particles with a similar separation, the d_{ij} will be larger than the d_{1j} between a high- and low-p_T particle. Thus, low-p_T particles will tend to cluster preferentially with high-p_T particles rather than amongst themselves. If there are no high-p_T particles within $2R$ of particle 1, the algorithm will combine particle 1 with all the low-p_T particles surrounding it to form a perfectly conical jet. If there is another high-p_T particle in the event, particle 2, this will be combined with particle 1 if $d_{12} < R$ to form a single jet. If $d_{12} > 2R$, particle 1 and 2 will form separate jets. If $R < d_{12} < 2R$, there will also be two jets which will share a boundary. The shape of the boundary, and hence of the two jets, depends on the ratio of energy of the two particles.

The calorimeters at ATLAS contain around 200,000 cells with different sizes. In order to reconstruct jets, it is necessary first to combine these cells into larger objects, with larger momentum. Topological cell clusters are used in this case as an input to the anti-k_T algorithm. These clusters are reconstructed starting from seed cells with a signal to noise ratio above a certain threshold. All neighbouring cells are included and neighbours of neighbours are included if they have a signal to noise ratio above a second (lower) threshold, with guard cells finally added to the cluster if they have a positive signal to noise ratio. These clusters are then subject to a splitting algorithm which further splits the clusters if they contain local signal maxima. The anti-k_T algorithm is then applied to these clusters to reconstruct the jets.

The ATLAS calorimeter has been calibrated using test-beam measurements with electrons and muons to ensure that the response of the calorimeter is correct for electromagnetic showers. Thus, the basic calorimeter scale is known as the electromagnetic scale. Hadrons have a lower response than electrons therefore explicit calibration must be applied to jets reconstructed in the calorimeter to determine the original parton energy.

There are two different schemes which may be used to calibrate jets: global calibration, which calculates corrections at the jet level, and local calibration, which aims to correct the topological clusters before the jets are reconstructed. For the results described here,

the local calibration scheme is used, which involves the following steps:

- Topological cell clusters are identified as electromagnetic or hadronic. Electromagnetic clusters only use calibration from the test-beam and no additional calibration is applied over and above that determined using test-beam data. The cells within hadronic clusters are weighted to obtain the calibrated energy deposit. Weights are location, energy and signal dependent.
- Corrections are applied to account for energy belonging to the cluster which may not be included if it lies below the threshold used in the clustering procedure.
- A further correction is included to account for energy deposited outside the calorimeter, for example in gap regions.

After this calibration is applied, the clusters are formed into jets using the anti-k_T algorithm.

2.6.5 Missing E_T reconstruction

The partons participating in the collisions at the LHC tend to carry very little momentum in the transverse plane. Thus, the total transverse momentum of the system is expected to be zero. If the total transverse momentum of the system is summed to be non-zero, a quantity known as missing E_T is assumed to be equal and opposite to the measured system p_T such that the total p_T is zero once this missing E_T is included. Certain particles, such as neutrinos, do not interact with the detector; their existence must be inferred by observing large missing E_T.

Missing E_T is reconstructed using the energy deposited in the electromagnetic and hadronic calorimeters, with corrections applied for the muons measured in the muon spectrometer. In addition to the energy deposited by particles arising from the high momentum transfer process, there are many other possible sources of extra energy deposition including noise as well as the underlying event and pileup interactions, which are described in Section 3.2.1. If high-p_T objects pass through dead regions or gaps in the calorimeters, this could also lead to the mismeasurement of missing E_T.

In order to ensure the accurate calculation of the missing E_T, it is essential that the calculation of the energy deposited in the calorimeter is as precise is possible. The application of calibrations, as described in Section 2.6.4, improve the accuracy of the energy measurements made by the calorimeters. Noise suppression is also applied to reduce the effect of noise contributing to the measured missing E_T. The topological cell clustering method, which is used to create clusters which may then be merged into jets, helps suppress noise since only cells with energies above a certain threshold are included, as described in Section 2.6.4.

2.6.6 Luminosity determination

Van der Meer scans are used to determine the luminosity at ATLAS [24]. During these scans, the position of one beam is moved in steps with respect to the other and the hit rates in a detector in the forward region, LUCID (luminosity measurement using a Cerenkov

integrating detector) [25], are measured. LUCID is located at 17m from the interaction point and counts the average number of particles per bunch crossing to determine the number of inelastic *pp* interactions per bunch crossing providing a measurement of the instantaneous luminosity at a given time. LUCID consists of sixteen C_4F_{10} gas filled aluminium tubes with reflective walls. When charged particles enter the gas, Cerenkov photons are created and reflected by the walls until they reach PMTs at the back of the tubes. If the signal measured by the PMTs is larger than a given threshold, a 'hit' is recorded. Timing signals are received from the LHC clock allowing the number of hits to be counted for each bunch crossing.

In addition to LUCID, there is a beam conditions monitor (BCM) which is located 2m away from the interaction point and monitors beam losses and provides feedback to the team operating the LHC. The BCM makes histograms of the single-sided and coincidence rate per bunch crossing. It has excellent timing resolution of 0.7 ns, ensuring accurate determination of the bunch-by-bunch rates.

Chapter 3

Higgs and diboson physics at ATLAS

Currently, the Standard Model (SM) of particle physics describes all the known particles in existence to a remarkable degree of accuracy. However, there is one remaining particle within the SM which has not yet been experimentally observed: the Higgs boson, postulated to explain the existence of massive gauge bosons. This chapter is arranged into two main sections: Section 3.1 provides an overview of the underlying theory and Section 3.2 discusses the experimental environment and status. Within Section 3.1, Section 3.1.1 describes the SM and Section 3.1.2 details the Higgs mechanism, the simplest way by which mass may be generated within the SM. Within Section 3.2, the hadron collider environment is discussed in Section 3.2.1, with a description of WW production in Section 3.2.2. The differences between Higgs boson and SM WW event kinematics are detailed in Section 3.2.3 and, finally, Section 3.2.4 provides a review of the current experimental status of Higgs boson searches.

3.1 Theoretical overview

3.1.1 The Standard Model

The SM aims to explain the fundamental forces of nature and all the particles which interact via these mechanisms. All of the SM particles are assumed to be fundamental, with no internal substructure. The majority of the SM particles are matter particles, with spin-1/2, and are shown in Table 3.1. The fermions are organised in families, or generations. Natural units, with $c = 1$, are used in Table 3.1 and throughout this thesis.

Antiparticles also exist, which have the opposite charge to their particle partners as well as inverted internal quantum numbers. The internal quantum numbers which are inverted include baryon number, which is defined as $B = \frac{1}{3}(n_q - n_{\overline{q}})$, where n_q and $n_{\overline{q}}$ are the number of quarks and antiquarks respectively. Charm, strangeness, beauty and truth, which represent the difference in the number of quarks and antiquarks of a certain flavour within a particle for charm, strange, bottom and top quarks respectively, are also inverted. The quantum number lepton number is also opposite for leptons and antileptons; it is 1 for leptons and -1 for antileptons. The quarks combine together in pairs to form mesons or in threes to form baryons, with mesons and baryons collectively known as hadrons. The quarks cannot exist freely and must exist within bound states as hadrons. Their existence has been inferred experimentally by studying the spectra of hadrons [26–29] as

Particle	Electric charge	Generation	Mass	Interactions
		Leptons		
ν_e	0	I	-	Weak
e	e	I	0.511 MeV	EM, weak
ν_μ	0	II	-	Weak
μ	e	II	105.7 MeV	EM, weak
ν_τ	0	III	-	Weak
τ	e	III	1.78 GeV	EM, weak
		Quarks		
u	2/3e	I	1.7-3.3 MeV	Strong, EM, weak
d	-1/3e	I	4.1-5.8 MeV	Strong, EM, weak
s	-1/3e	II	101 MeV	Strong, EM, weak
c	2/3e	II	1.27 GeV	Strong, EM, weak
b	-1/3e	III	4.19 GeV	Strong, EM, weak
t	2/3e	III	172 GeV	Strong, EM, weak

Table 3.1: Particles of the SM. The neutrinos can be taken to be approximately massless since their mass is much smaller than that of the other particles. The electric charge is given in terms of e, the electric charge of an electron.

well as performing deep inelastic scattering of leptons on proton targets [30, 31].

Quarks carry colour charge in addition to electric charge, with antiquarks carrying anticolour charge. Gluons, the gauge bosons which carry the strong force, couple to colour charge thus quarks may interact via the strong interaction. The coupling between quarks and gluons is governed by the strong coupling constant α_S. This is a bit of misnomer: α_S is not a constant but rather varies with the energy of the interaction. At high energies and short distances, for example when quarks are close together within a hadron, α_S is small and the quarks are quasi-free. However, as the distance between neighbouring quarks increases, α_S rapidly increases, acting to bring the quarks back together. At this stage, it may be energetically more favourable for the quarks to produce a new quark-antiquark pair. This may happen many times at high energies, forming a 'jet' of hadrons. These jets are a common feature within hadron colliders. This is described formally by the theory of QCD, which was formulated by Gross, Politzer and Wilczek [32–34].

In addition to the strong force, there is the electromagnetic force which is mediated by the photon and couples to electric charge. This was the first of the fundamental forces to be discovered experimentally and all of the matter particles in the SM may interact via it except the neutrinos which have no electric charge. However, quarks preferentially decay via the strong force due to the fact that the coupling constant to gluons is much larger than that to photons. This means that hadrons decaying via the strong interaction have a lifetime which is significantly shorter than those which decay electromagnetically.

For the neutrinos, there is only one possible way to interact: via the weak interaction, so-called because it is much weaker than the other forces. This leads to much longer particle lifetimes for weakly decaying particles than would be observed if they could decay via the strong or electromagnetic interactions. The weak interaction is mediated by $W^\pm$ and Z^0 bosons, where the $W^\pm$ bosons may mediate flavour-changing interactions such as the decay of top quark to a bottom quark via the production of a W boson which may

then decay to quarks or leptons. No flavour changing neutral currents are observed.

These fundamental forces should not be viewed as entirely separate entities. Glashow, Salam and Weinberg [35, 36] succeeded in unifying the electromagnetic and weak forces to give a unified theory of electroweak interactions. The subsequent discovery of neutral currents provided further evidence that their theory was correct. There have since been proposals that in fact all the fundamental forces may become unified at some high energy scale [37].

The final fundamental force which is known to exist is gravity. This is not accounted for at all within the SM at present, although the existence of a graviton to carry the gravitational force has been postulated. Searches at CDF [38, 39] and D0 [40] have placed the most stringent limits to date on excited graviton production in the context of extra dimensions and have revealed no evidence for gravitons yet but it is possible that they exist at energies which are so far inaccessible to human experiment. There have been many attempts to incorporate gravity into a unified picture, with the electroweak, strong and gravitational interactions all evolving to a single point in terms of coupling strength at the grand unified theory (GUT) scale, postulated to be around 10^{16} TeV [37] although more observations are necessary to understand whether this unification exists.

Particle	**Electric charge**	**Mass**	**Width**	**Interactions**
g (gluon)	0	0	-	Strong
γ (photon)	0	0	-	EM
$W^{\pm}$	$\pm$ e	80.4 GeV	2.09 GeV	Weak
Z^0	0	91.2 GeV	2.50 GeV	Weak

Table 3.2: Gauge bosons of the SM. All these particles have spin-1. Masses and widths are taken from Ref. [1].

The spin-1 gauge bosons within the SM are listed in Table 3.2 along with their charge, mass, width and the interactions they mediate. The widths of the massive gauge bosons are related to their production cross section by the relativistic Breit-Wigner resonance formula [1]:

$$\sigma(E^2) \propto \frac{1}{(E^2 - E_0^2)^2 + E_0^2\Gamma^2} \tag{3.1}$$

where E is the centre of mass energy, E_0 is the centre of mass energy at the resonance and Γ is the full width at half maximum of the resonance. The decays of W bosons to leptons are investigated in this thesis; the branching ratio of the W boson to one lepton species is $\sim$11% [1], giving a total branching ratio for decays $W \to l\nu_l$ of $\sim$33% [1], where $l = e, \mu, \tau$. Tau leptons may also decay hadronically or leptonically and have a branching ratio for decays $\tau \to \ell\nu_\ell\nu_\tau$ of $\sim$17% [1], where $\ell = e$ or μ.

This thesis focuses on the interactions within the electroweak sector, specifically the production and decay of pairs of W bosons. While the electroweak theory performs spectacularly well in terms of describing the observed interactions as well as the relative rates at which different processes occur, there is one rather dramatic shortcoming: all the gauge bosons mediating the electroweak interaction are predicted to be massless. The W

and Z bosons were first observed experimentally at the SppS at CERN [41–43], a proton-antiproton collider with a centre of mass energy of 540 GeV. Their properties have since been extensively measured at LEP, the Tevatron and the LHC and they are known to be massive therefore there is obviously something missing from our current understanding of particle physics, in which these gauge bosons are predicted to be massless.

One possible way to generate particle masses is the Higgs mechanism, which would give rise to an observable, massive Higgs boson. This is discussed in the following section.

3.1.2 Spontaneous symmetry breaking

The Higgs mechanism [2–7] postulates the existence of a Higgs matter field which occupies the entirety of space. This field, which is postulated to be a scalar with spin-0 quanta known as Higgs bosons, is proposed to couple symmetrically to massive gauge bosons and break the local gauge symmetry, $SU(2)_L \otimes U(1)_Y$, of the electroweak interaction. This spontaneous electroweak symmetry breaking occurs under the assumption that the ground state of the system, given by its vacuum expectation value, is asymmetric in field space, causing mass to be generated when particles interact with the Higgs field. This phenomenon is also seen in other areas of physics, for example in the generation of ferromagnetism [44].

An analogy to the Higgs field may be made by considering the field as a room full of people at a glitzy showbusiness party. When a celebrity such as Lady Gaga walks into the room, she cannot walk from one side of the room to the other without being stopped by people eager to talk to her: these people are analogous to the spontaneously appearing and disappearing Higgs bosons constituting the Higgs field. Her progress through the room is significantly slowed: she has gained mass. Conversely, when an average particle physicist walks through the room, the people at the party ignore her and she can continue through the room unimpeded: she is massless. This same mechanism occurs with the particles in the SM. Those which interact with the Higgs field have their journey through the vacuum impeded, gain mass and travel at a velocity less than the speed of light. Particles which do not couple to the Higgs field, such as photons and gluons, travel at the speed of light and remain massless.

Before considering the Higgs mechanism it is instructive to first consider the Goldstone theorem [45–47], which describes the spontaneous breaking of a continuous symmetry of a scalar field. This is covered in the following section.

The Goldstone theorem

The properties of a complex scalar field given by:

$$\phi = \frac{1}{\sqrt{2}}(\phi_1 + i\phi_2) \tag{3.2}$$

may be described by the following Lagrangian:

$$\mathcal{L} = (\partial_\mu \phi)^\dagger (\partial^\mu \phi) - \mu^2 \phi^\dagger \phi - \lambda(\phi^\dagger \phi)^2 \tag{3.3}$$

This possesses $U(1)$ global gauge symmetry and hence is invariant under the transformation $\phi \rightarrow \phi' = e^{i\alpha}\phi$ where α is a constant.

The Lagrangian may be rewritten in terms of ϕ_1 and ϕ_2 as:

$$\mathcal{L} = \frac{1}{2}(\partial_\mu \phi_1)^2 + \frac{1}{2}(\partial_\mu \phi_2)^2 - V(\phi_1, \phi_2) \tag{3.4}$$

where the potential $V(\phi_1, \phi_2)$ is given by:

$$V(\phi_1, \phi_2) = \frac{1}{2}\mu^2(\phi_1^2 + \phi_2^2) + \frac{1}{4}\lambda(\phi_1^2 + \phi_2^2)^2 \tag{3.5}$$

This potential has a Mexican hat shape when $\mu^2 < 0$ and $\lambda > 0$, as shown in Figure 3.1. $V(\phi_1, \phi_2)$ has a ring of minima on the circle $\phi_1^2 + \phi_2^2 = f^2$, where $f^2 = \frac{-\mu^2}{\lambda}$. Thus, any of these minima is a valid solution for the ground state of this system and choosing one specific solution from among the infinitely many solutions breaks the symmetry of the system so it is no longer rotationally symmetric in the ϕ_1-ϕ_2 plane.

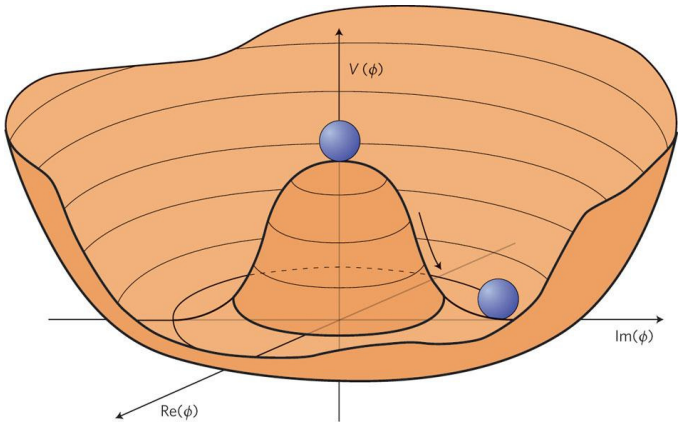

Figure 3.1: A diagram showing the Mexican hat potential, $V(\phi_1, \phi_2)$ for a complex scalar field. Re(ϕ) corresponds to ϕ_1 and Im(ϕ) corresponds to ϕ_2 in Equation 3.2.

The symmetry is said to be spontaneously broken since there is no external influence causing the symmetry breaking; it is a direct consequence of the form of the potential. If μ^2 were larger than zero, the potential would have a bowl shape with a single minimum at the origin instead of the Mexican hat shape, giving one possible solution for the ground state and retaining the rotational symmetry.

Choosing a specific minimum at $\phi_1 = f$, $\phi_2 = 0$ and introducing new fields, χ_1 and χ_2, such that:

$$\begin{aligned} \phi_1(x) &= f + \chi_1(x) \\ \phi_2(x) &= \chi_2(x) \end{aligned} \tag{3.6}$$

gives:

$$\phi(x) = \frac{1}{\sqrt{2}}[f + \chi_1(x) + i\chi_2(x)] \tag{3.7}$$

This allows $\chi_1(x)$ and $\chi_2(x)$ to be interpreted as fluctuations around the ground state of $\phi_1 = f$, $\phi_2 = 0$. Substituting ϕ_1 and ϕ_2 back into the original Lagrangian given by

Equation 3.4 and using the relation $\mu^2 = -\lambda f^2$ gives:

$$\begin{aligned}\mathcal{L} &= [\tfrac{1}{2}(\partial_\mu \chi_1)^2 - \lambda f^2 \chi_1^2] \\ &\quad +[\tfrac{1}{2}(\partial_\mu \chi_2)^2] \\ &\quad -[\lambda f(\chi_1^3 + \chi_1 \chi_2^2)] - [\tfrac{\lambda}{4}(\chi_1^4 + \chi_2^4 + 2\chi_1^2\chi_2^2)] \\ &\quad +\tfrac{\lambda}{4} f^4\end{aligned} \tag{3.8}$$

This equation may be understood term by term. The first term is the standard Klein-Gordon Lagrangian for a scalar field. This is physically interpreted as radial oscillations around the minimum with a mass term of $m_{\chi_1} = \sqrt{2\lambda f^2}$. In terms of the Mexican hat analogy, these oscillations occur from the brim of the hat towards the centre of the hat via the ring of minima, giving rise to a restorative force towards the minima. The second term represents oscillations with zero mass, χ_2, around the ring of minima illustrated in Figure 3.1. This time, there is no restorative force and the oscillations are considered to be 'resistanceless'. This corresponds to a scalar field with a massless field quantum with the oscillations around the minima known as a Goldstone boson. The last two terms are less interesting; the third term represents cubic and quartic field interactions while the fourth term is just a constant.

Thus, the Goldstone theorem may be summarised as such: spontaneous symmetry breaking always generates one or more massless scalar bosons. This theorem may be extended further with the addition of extra potentials. In these cases, it is possible to generate not just massless scalars but also massive scalars. This is the idea of the Higgs mechanism, which is discussed in the next section.

The Higgs mechanism

The previous section considered the spontaneous breaking of a continuous symmetry of a scalar field. This section covers the breaking of a local gauge symmetry, specifically $U(1)$, the symmetry of the electromagnetic sector of the SM. This is just an example; in nature it is the $SU(2)_L \otimes U(1)_Y$ symmetry of the electroweak sector which is broken.

If the electromagnetic interaction is added in with gauge field A_μ, the Lagrangian from Section 3.1.2 becomes:

$$\mathcal{L} = [(\partial_\mu + ieA_\mu)\phi]^\dagger[(\partial^\mu + ieA^\mu)\phi] - \frac{1}{4}F_{\mu\nu}F^{\mu\nu} + V(\phi) \tag{3.9}$$

where $F_{\mu\nu} = \partial_\mu A_\nu - \partial_\nu A_\mu$. $V(\phi)$ is taken here to be:

$$V(\phi) = \frac{1}{2}\mu^2\phi^\dagger\phi - \frac{1}{2}\lambda^2(\phi^\dagger\phi)^2 \tag{3.10}$$

It is useful to parameterise the complex scalar field ϕ, which is defined as in Equation 3.6, in terms of its modulus and phase as:

$$\phi = \frac{1}{\sqrt{2}}(f + \rho(x))e^{i\theta(x)/f} \tag{3.11}$$

with real fields $\rho(x)$ and $\theta(x)$.

As previously, the Lagrangian must be invariant under a local $U(1)$ gauge transformation:

$$\phi \rightarrow \phi' = e^{-ie\chi(x)}\phi \tag{3.12}$$

In order to achieve this invariance, a corresponding transformation of A_μ must be applied:

$$A_\mu \rightarrow A'_\mu = A_\mu + \partial_\mu \chi \tag{3.13}$$

Invariance is only achieved under a combined transformation of Equations 3.12 and 3.13.

When the first transformation, described by Equation 3.12, is applied, the ρ and θ fields transform as:

$$\begin{array}{l} \rho \rightarrow \rho \\ \theta \rightarrow \theta - ef\chi \end{array} \tag{3.14}$$

Thus, if the arbitrary field χ is chosen to be $\chi = \theta/ef$, θ is zero and ϕ is real. With this choice and the application of the second transformation, described by Equation 3.13, the following values are obtained for ϕ' and A'_μ:

$$\begin{array}{l} \phi' = \frac{1}{\sqrt{2}}(f + \rho) \\ A'_\mu = A_\mu + \frac{1}{ef}\partial_\mu \theta \end{array} \tag{3.15}$$

Since the theory is gauge invariant, these lead to the same equations of motion as the original fields ϕ and A_μ so it is possible to choose a gauge such that ϕ shows no dependence on θ. Using these primed fields in the Lagrangian gives:

$$\begin{array}{rcl} \mathcal{L}(\phi', A'_\mu) & = & [\frac{1}{2}\partial_\mu \rho \partial^\mu \rho - \frac{1}{2}\mu^2 \rho^2] \\ & + & \frac{1}{2}e^2 f^2 A'_\mu A'^\mu - \frac{1}{4}F'_{\mu\nu}F'^{\mu\nu} + ... \end{array} \tag{3.16}$$

where the extra terms are interaction terms. As in the Goldstone case, the field ρ oscillates in a restoring potential with mass μ. However, the massless mode θ appears to have vanished so there is no longer a massless Goldstone boson. While θ does not appear explicitly in the Lagrangian, it is nevertheless present in A'_μ, which gives the field for a massive spin-1 particle with mass ef. This is the basis of the Higgs mechanism: the massless gauge field A_μ is transformed into a massive spin-1 field A'_μ by 'eating' the original massless field θ.

In addition to the appearance of a massive spin-1 boson with mass ef in the Lagrangian, given by the second term, the first term may also be recognised as a massive scalar, spin-0, boson with mass given by μ. In the case of electroweak symmetry breaking, this is the Higgs boson.

This section has described a simplified version of the Higgs mechanism based only on the electromagnetic interaction, known as the Abelian Higgs mechanism. In the SM, the same mechanism must be applied to a local $SU(2)_L \otimes U(1)_Y$ symmetry instead of a simpler $U(1)$ gauge symmetry. It is applied to a complex scalar doublet, consisting of four components, which after spontaneous symmetry breaking gives rise to three massive particles, the $W^\pm$ and Z^0 bosons, and one massless particle, the photon, as well as a massive scalar particle, the Higgs boson. Exactly the same method may be used in this case and is described fully in various textbooks [48, 49].

3.2 Experimental overview

3.2.1 The hadron collider environment

To develop a strategy to search for a specific signal within a hadron collider environment like the LHC, it is important to understand the event properties so that any factors which

may affect the search are identified.

The LHC collides two beams of protons, which consist of partons which carry a certain fraction of the proton's momentum, x. Partons may be either the valence quarks (uud) which make up the proton, the gluons (which are radiated from the quarks) or the sea quarks ($q\bar{q}$ pairs which are spontaneously produced and rapidly annihilated within the proton). The parton distribution functions (PDFs), $f_i(x, Q^2)$, give the probability that parton i has momentum fraction x at the energy scale $\sqrt{Q^2}$ of the event. These are determined experimentally by fits to deep inelastic scattering data at a given Q^2 and evolved to all values of Q^2 using the DGLAP evolution equations [50–52].

For the production of a heavy new particle, such as a Higgs boson, the part of the event of interest is the hard scatter, where two partons interact with a high enough centre of mass energy to produce a new massive particle. This is shown in Figure 3.2.

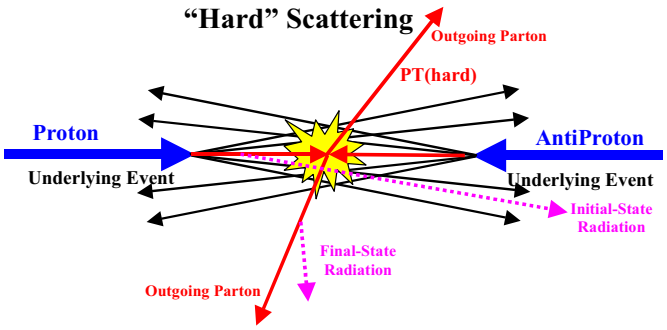

Figure 3.2: A diagram showing the type of hard scattering process which occurs at a hadron collider. At the LHC, two protons are collided instead of a proton and antiproton but the event characteristics are otherwise exactly the same.

There are other characteristics of hadron collider events which are also shown in Figure 3.2. As the partons which take part in the hard scatter approach the point of collision, they may emit initial state radiation. Additionally, after scattering has occurred, they may emit final state radiation. This can lead to a number of high-p_T jets being reconstructed in the detector in addition to the decay products of whatever is produced in the hard scatter.

There will also be proton remnants remaining after the hard scatter. These will primarily travel in the direction of the beams and mainly escape down the beam pipe, but some portion of the remnant jets may enter the detectors, particularly in the more forward regions. This contributes to the underlying event.

Since protons are collided in bunches, there is also the possibility of both multiple parton and multiple proton interactions within the same bunch crossing which may have different properties, such as different z position of the interaction vertices. These additional interations may lead to multiple hard scattering processes and many collision vertices. This is known as pileup and is an increasing problem for analysis at the LHC as the instantaneous luminosity increases. It may be corrected for during the offline analysis and this is covered in Chapter 4.

Cosmic rays may also pass through the detector. The requirement that events must

occur in time with bunch crossings as well as selecting only particles which have originated from the measured primary vertex reduces this effect to negligible levels. Further backgrounds to pp collisions arise from beam halo and cavern backgrounds, since it is impossible to create a complete vacuum within the LHC. There will always be a small amount of particles present which may interact with the beam to produce something which may be falsely identified as a signal in the detector. However, this is expected to be a small effect and may be suppressed in the same way cosmic ray backgrounds are reduced.

3.2.2 WW production at hadron colliders

At hadron colliders such as the LHC, pairs of W bosons are produced primarily via the mechanisms shown in Figure 3.3, in which two quarks from the colliding protons are in the initial state. WW pairs may also be produced via gluon-gluon fusion, which is expected to contribute around 3% to the total rate of WW production at ATLAS and is shown in Figure 3.4.

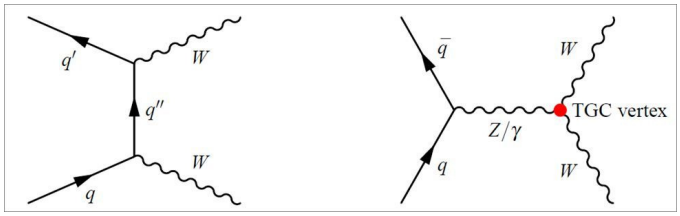

Figure 3.3: Feynman diagrams showing $q\bar{q}'$ production mechanisms for W boson pairs. The diagram on the right shows a triple gauge coupling (TGC) vertex, which involves trilinear gauge boson couplings between WWZ or $WW\gamma$.

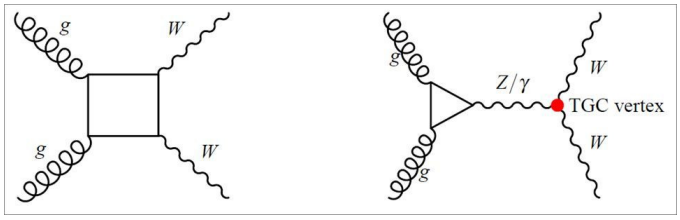

Figure 3.4: Feynman diagrams showing gluon-gluon fusion production mechanisms for W boson pairs. The diagram on the right shows a triple gauge coupling (TGC) vertex, which involves trilinear gauge boson couplings between WWZ or $WW\gamma$.

The measurement of WW production is particularly interesting because it is not only a dominant background to $H \rightarrow WW$ production, it is also a probe of potential new physics. The SM predicts vector boson self-couplings as a result of the non-Abelian nature of the $SU(2)_L \otimes U(1)_Y$ gauge symmetry [36], which was verified experimentally at LEP by precise measurements of WW and ZZ production [1]. Within the SM, only $WW\gamma$ and WWZ vertices are allowed. However, extensions to the SM may produce some relative deviation from the measured vertex couplings, generally at the 10^{-3}- 10^{-4}

level [53], from these allowed couplings at a high energy scale. Deviations such as this would be observed experimentally as an enhanced cross section for WW production, particularly at high values of p_T^W. Hence, precision measurements of the W boson pair production cross section could provide a hint of interesting new physics. To investigate the deviation of the TGCs from the SM predictions, it is necessary to compare the shape of the measured p_T or mass distributions to MC predictions and determine any deviation of TGCs from expectation. This is not covered here, however recent results may be found in Ref. [54].

3.2.3 Differences between $H \to WW$ and SM WW kinematics

The Higgs boson is a spin-0 particle so, to conserve spin, the overall spin of the system must be zero when it decays to two W bosons. W bosons are spin-1 massive particles, giving them three possible values for the z-component of spin: -1, 0 or 1. Thus, there are multiple combinations of W-pair spins which give an overall spin-0 system in the z-direction. These combinations are shown in Figure 3.5 with the helicity of the W bosons indicated. Helicity, λ, is defined as the projection of a particle's spin along its direction of motion. This diagram indicates that there are three helicity states allowed by spin conservation: $+1, +1$; $-1, -1$ or $0, 0$. Both W bosons produced via $H \to WW$ must have the same helicity.

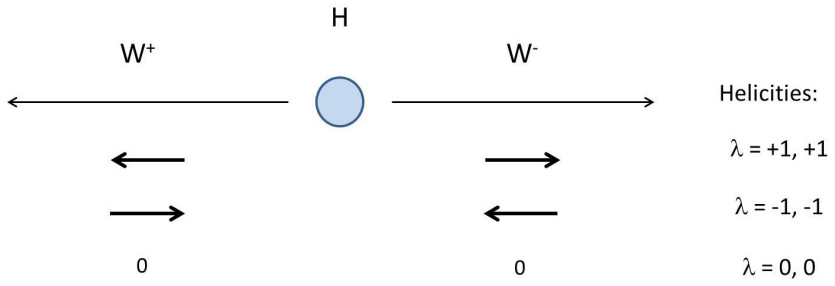

Figure 3.5: Diagram showing the decay of a spin-0 Higgs boson to two spin-1 W bosons. The directions of the z-components of the W bosons' spins are indicated on the diagram by small, bold arrows and the directions of motion of the W bosons shown by the longer arrows.

Investigating the allowed decays of the W bosons from these three allowed WW states gives the diagrams illustrated in Figure 3.6. Due to the V-A structure of the weak interaction, only neutrinos with negative helicity exist and no positive helicity neutrinos are allowed. Similarly, only positive helicity antineutrinos are observed. This constrains the helicities of the leptons such that each of the three allowed WW states has only one possible helicity structure.

Looking at the allowed decays of the pairs of W bosons produced in Higgs boson decays, it can be seen that, due to the electroweak couplings and requirement of spin conservation, the charged lepton and charged antilepton are preferentially emitted in the same direction. This leads to a small opening angle between the charged lepton pair and a small invariant mass of the dilepton pair.

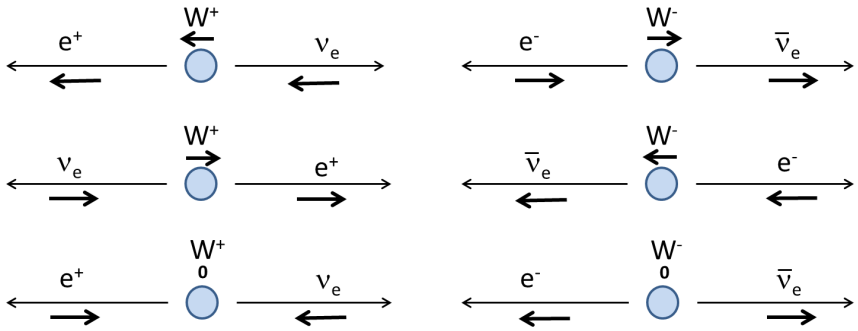

Figure 3.6: Diagram indicating the three possible WW decays which are allowed by spin conservation (from top to bottom) where the W bosons have been produced by the decay of a Higgs boson: both W bosons having negative helicity, both W bosons having positive helicity and finally both W bosons having helicity zero. As in Figure 3.5, helicity is shown by short, bold arrows and direction of motion is indicated using longer arrows.

This may be seen by looking at the invariant mass of the dilepton pair, M_{ll}:

$$\begin{aligned} M_{ll} &= \sqrt{(E_{l_1} + E_{l_2})^2 - (\mathbf{p_{l_1}} + \mathbf{p_{l_2}})^2} \\ &= E_{l_1}^2 - p_{l_1}^2 + E_{l_2}^2 - p_{l_2}^2 + 2E_{l_1}E_{l_2} - 2p_{l_1}p_{l_2}\cos\theta \\ &\simeq 2E_{l_1}E_{l_2}(1 - \cos\theta) \text{ for } M_{l_{1,2}} \ll E_{l_{1,2}} \end{aligned} \tag{3.17}$$

where M_{l_i} and E_{l_i} are the mass and energy respectively of lepton i. Thus, selecting events with small values of M_{ll} is one way to remove backgrounds from non-Higgs boson processes, which tend to have larger M_{ll}.

The dominant background to the $H \to WW$ process arises from SM $q\bar{q}' \to WW$ production, as illustrated in Figure 3.3. The $q\bar{q}'$ system which produces the WW pair has an overall z-component of the spin of -1, 0 or 1 since quarks are spin-1/2. If the z-component of the spin of the system is zero, the W bosons have the same relative spin as those from the decay of a Higgs boson. However, when the z-component of the spin of the system is ± 1, different relative spins are allowed, with one W boson in a zero helicity state and one W boson with helicity $\pm$ 1. When an average over the spin states observed in $q\bar{q}'$ pairs is taken, significant differences in $\Delta\phi_{ll}$ and M_{ll} can be observed when a comparison between $H \to WW$ and SM WW distributions is performed. These distributions may be utilised to reduce the continuum WW background to $H \to WW$ production. This is discussed further in Section 4.8.4.

3.2.4 Current limits on Higgs boson production cross section

There are many possible ways to search for the Higgs boson experimentally at the LHC. The expected production cross section for the Higgs boson via various production mechanisms is shown in Figure 3.7.

For this thesis, a search is performed in the zero, one and two jet channels where the zero and one jet channels arise mainly from the $gg \to H$ (gluon-gluon fusion, ggF) production mechanism. Events in the two jet channel are primarily produced via vector

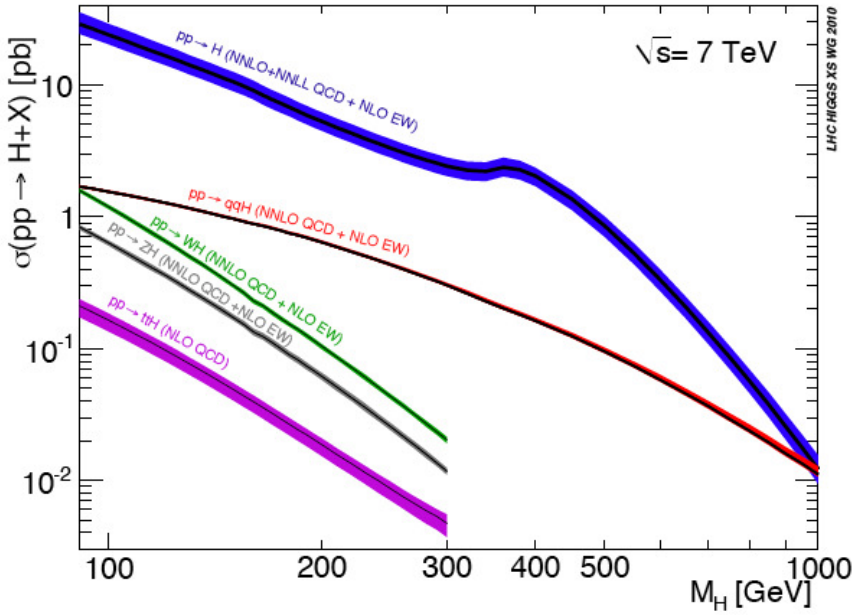

Figure 3.7: Cross section for Higgs boson production at the LHC at 7 TeV centre of mass energy [55]. The $pp \to H$ production mechanism corresponds to $gg \to H$ production. The vector boson fusion (VBF) mechanism is shown here as $pp \to qqH$, ATLAS Experiment © 2011 CERN.

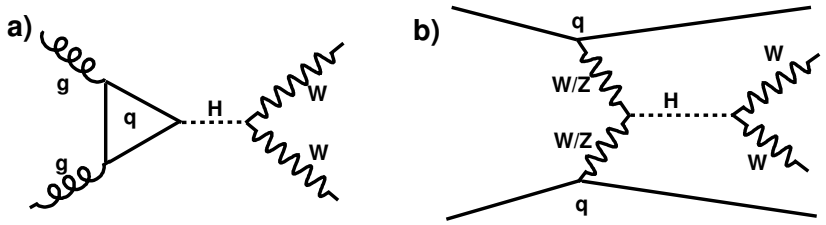

Figure 3.8: Gluon-gluon fusion (ggF) Higgs boson production mechanism (a) and vector boson fusion (VBF) Higgs boson production mechanism (b).

boson fusion (VBF) and are allowed to have two or more jets. The Feynman diagrams for these processes are shown in Figure 3.8.

There are also many ways in which the Higgs boson may decay. As described in Section 3.1.2, the Higgs boson couples to all massive particles, as well as to itself. Thus, it may decay to any massive particles allowed by the conservation laws of the SM. For a given Higgs boson mass, m_H, the couplings to fermions and gauge bosons are fixed and therefore production cross sections, decay widths and branching ratios may be calculated. The total width is shown in Figure 3.9 and Figure 3.10 shows the branching ratios of the Higgs boson to various final states as a function of m_H as calculated by HDECAY [56, 57]. These branching ratios are used in conjunction with the production cross sections in Figure 3.7 and the branching ratio for W decays to $\ell\nu_\ell$ (where $\ell = e\mu$) to calculate the expected cross section of Higgs boson production at the LHC. This is covered in more detail in Chapter 8.

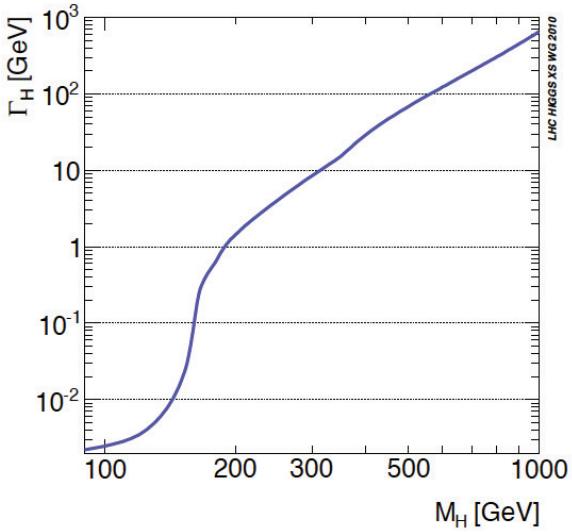

Figure 3.9: Higgs boson total width as a function of m_H [55], ATLAS Experiment © 2011 CERN.

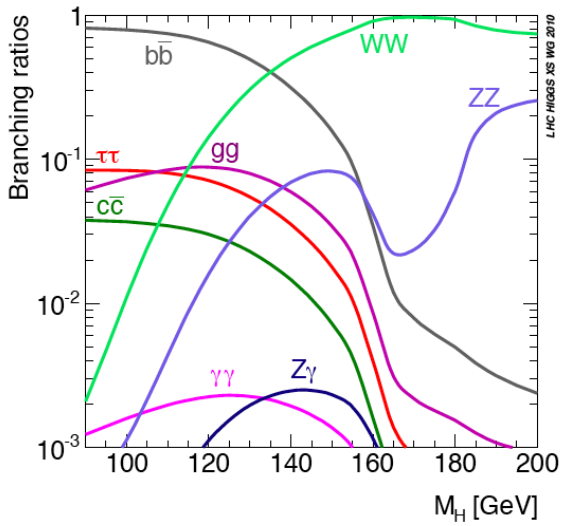

Figure 3.10: Higgs boson decay branching ratios as a function of m_H [55], ATLAS Experiment © 2011 CERN.

Figure 3.10 shows that at high m_H the Higgs boson decays dominantly to pairs of W bosons, suggesting that this search channel provides excellent sensitivity to the Higgs boson. This sensitivity may be further supplemented by additionally using the ZZ decay channel. This is an interesting channel since, in the mode $H \to ZZ \to 4\ell$, the Higgs boson mass may be fully reconstructed. However, the low branching ratio of $ZZ \to 4\ell$ leads to a low overall cross section so a significant amount of data must be analysed to obtain a signal.

At low m_H, $b\bar{b}$ decays are dominant. This channel is overwhelmed by the QCD background, although approaches using the VBF $H \to b\bar{b}$ decay mode, with the use of two 'tag' jets which are well separated in η to separate the signal from the background are being

studied. Associated production in the $ttH, H \to b\bar{b}$ channel, with the top quarks decaying via $t\bar{t} \to W^+bW^-\bar{b}$ and one of the W bosons decaying leptonically, are also under investigation since this channel has a high-p_T lepton which may be triggered on and used to separate signal from the large QCD background. Similarly, searches may be performed in the associated production channels $W/ZH, H \to b\bar{b}$, which provide reasonable sensitivity in the low mass region due to the charged leptons from the W and Z decays, which allow the QCD background to be reduced. There is also a reasonably large branching ratio for decays in the $H \to \tau\tau$ channel. This be may searched for in different sub-channels: hh, ℓh and $\ell\ell$, where h represents a hadronic τ decay and ℓ indicates a leptonic τ decay. The searches with leptons in the final state suffer from less QCD background although are subject to the smaller branching ratio of taus to leptons compared to hadrons. QCD background may be problematic for the hh channel, although studies have indicated that searches in this channel may be approximately as sensitive as those in the $\ell\ell$ channel [58]. If the Higgs boson does exist with low mass it is likely that the combination of many channels will be used to gain sufficient evidence for its discovery. The WW channel may also give a useful contribution at low m_H, although it will be necessary to re-optimise cuts for a low mass Higgs boson to maximise signal acceptance while still adequately rejecting background processes.

Figure 3.11 summarises the expected contribution of each search channel to the limits on Higgs boson production which may be obtained with 1 fb^{-1}.

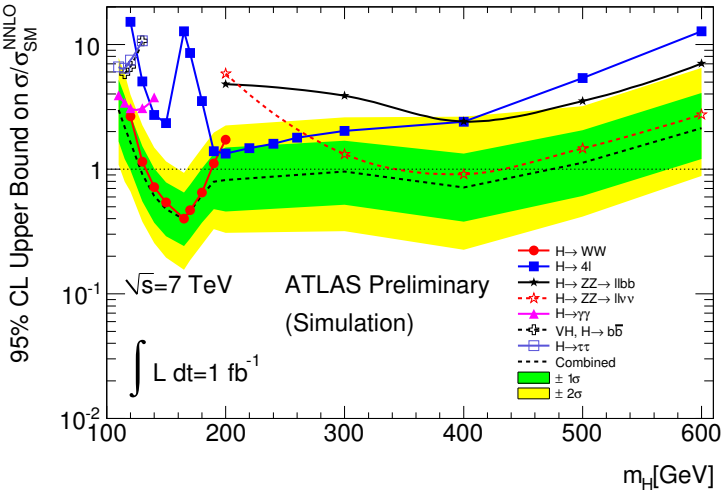

Figure 3.11: Higgs boson cross sections, as a ratio of the SM, which may be excluded with 1 fb^{-1} of data at ATLAS [59]. The channels expected to contribute to the search are shown separately, and a combination of all the channels is also shown, ATLAS Experiment © 2011 CERN.

Many searches for the Higgs boson have been performed at previous collider experiments. At LEP-II, an electron-positron collider, searches for the Higgs boson were performed mainly in the ZH production channel. No significant signal was seen, so a limit was set on the mass of the Higgs boson of $m_H > 114.4$ GeV at 95% C.L. using a combination of all search channels at all the LEP experiments [60].

More recently, experiments at the Tevatron proton-antiproton collider which runs at a centre of mass energy of 1.96 TeV, have also set limits on Higgs boson production. Using a combination of results from the CDF and D0 collaborations, the Higgs boson has been excluded at 95% C.L. in the mass range $158 < m_H < 173$ GeV [61].

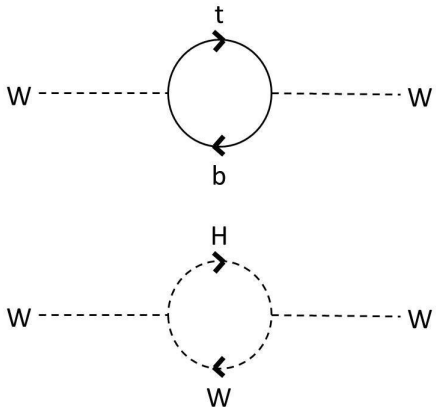

Figure 3.12: Examples of top quark (top) and Higgs boson (bottom) loop corrections to the mass of the W boson.

There are additional indirect constraints on the mass of the Higgs boson since, if it exists, the Higgs boson is expected to provide a correction to the tree-level masses of SM particles in loop processes, such as those shown in Figure 3.12. The masses of particles such as the W boson and the top quark have been measured very precisely at LEP [62] and the Tevatron [63, 64] and can be combined with other electroweak parameters to indirectly constrain the Higgs boson mass to lie within $114.4 < m_H < 144$ GeV at 95% C.L. [65]. The fit to electroweak precision data given in Figure 3.13 shows that these data actually prefer a very low Higgs boson mass, at less than the LEP constrained minimum of 114.4 GeV. This highlights the importance of searches covering the full range of Higgs boson masses, particularly in the low mass region, since electroweak data suggest that if the SM Higgs boson does exist it is likely to have a low mass.

This is an exciting time for Higgs physics. Projections, shown in Figure 3.14, suggest that with 1 fb^{-1} of data the ATLAS experiment will be able to exclude the SM Higgs boson between $125 < m_H < 460$ GeV if its mass is outside this range, leaving only a small range of allowed values of m_H. If ATLAS is able to collect 3 fb^{-1} of data, the Higgs boson could be excluded in the full mass range from 114.4 GeV to 500 GeV if its mass is not in this range. It is expected that ATLAS will collect between 1 and 3 fb^{-1} of data before the end of 2011 therefore the SM Higgs boson could be completely excluded this year. If this occurs, an alternative method of electroweak symmetry breaking must be sought.

However, if the SM Higgs boson exists, ATLAS also provides excellent prospects for its discovery. Figure 3.15 shows that, depending on the mass of the Higgs boson, ATLAS should be able to gain tantalising 3σ evidence for its existence with the 2011 data. It is clear that the landscape of Higgs physics will be changed incontrovertably by the end of 2011, whether the SM Higgs boson exists or not, which will have far-reaching consequences for our understanding of the SM and particle physics.

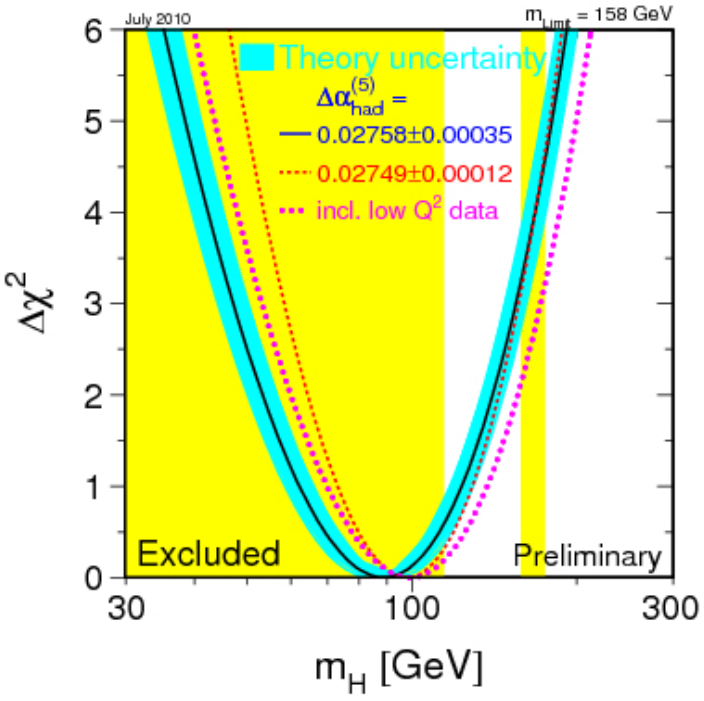

Figure 3.13: The preferred value of Higgs boson mass as extracted from electroweak precision measurements [66].

This thesis presents the results of the first publicly released search for the Higgs boson using LHC data, describing the first step towards the goal of either discovering the Higgs boson or completely ruling out its existence at the LHC.

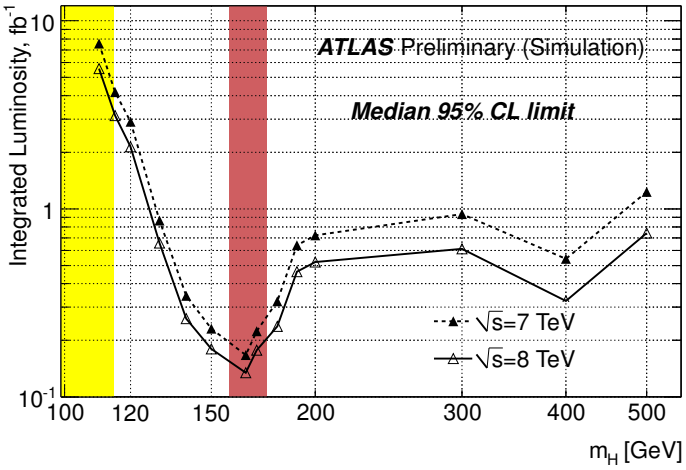

Figure 3.14: The integrated luminosity required to exclude the SM Higgs boson at 95% C.L. as a function of m_H. Curves are shown assuming a centre of mass energy of both 7 and 8 TeV [59], ATLAS Experiment © 2011 CERN.

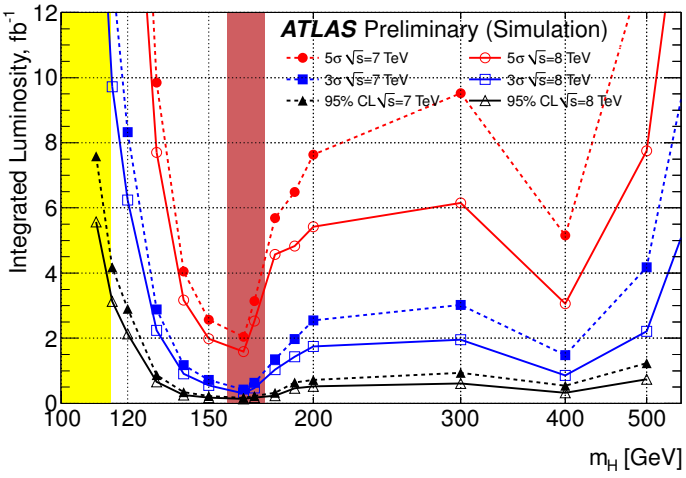

Figure 3.15: The integrated luminosity required to exclude, provide evidence for and discover the SM Higgs boson at 95% C.L. as a function of m_H. Curves are shown assuming a centre of mass energy of both 7 and 8 TeV [59], ATLAS Experiment © 2011 CERN.

Chapter 4

Event selection

The processes investigated in this thesis are the SM production of WW pairs and the production of WW pairs via the decay of a Higgs boson. W bosons may decay leptonically or hadronically. In this thesis, the leptonic decays of W bosons are used to reduce the background from processes containing jets, which is expected to be significant at the LHC. The event topology contains two W bosons, each of which is required to decay leptonically, giving three possible final states: $e\nu_e e\nu_e$, $\mu\nu_\mu\mu\nu_\mu$ and $e\nu_e\mu\nu_\mu$, referred to as ee, $\mu\mu$ and $e\mu$ respectively throughout the rest of this thesis. Additionally, there may be jets in the final state due to the VBF production mechanism or due to gluon radiation. The SM WW cross section measurement is performed in the zero jet channel to avoid the increasing contamination from background processes, such as top, with increasing jet multiplicity. It is important to maximise the signal acceptance for a search for a new, low cross section physics process therefore the Higgs boson search is performed in three jet channels: zero, one and at least two jets, giving a total of nine channels overall.

The signal and background processes are modelled primarily with MC, although some backgrounds are estimated using data-driven methods as covered in Chapter 6. Section 4.1 details the MC samples used as well as the cross sections of the signal and main backgrounds. The same MC samples are used for both WW and $H \to WW$ searches.

The requirements on the quality of the data which must be satisfied before applying any further selection are described in Section 4.2. WW and $H \to WW$ events with leptonically decaying W bosons typically have high-p_T leptons so lepton triggers as described in Section 4.3 are used to select events in data which may be consistent with this signature. In order to detect WW and $H \to WW$ events, it is necessary to accurately reconstruct both leptons and jets. The selection of leptons and jets is described in Sections 4.4 and 4.5 respectively. It is also necessary to determine the missing E_T arising from undetected neutrinos in these events to a high degree of accuracy in order to select the signal efficiently. Missing E_T selection is discussed in Section 4.6.

Objects are selected using almost identical criteria for the WW and $H \to WW$ analyses. Where there are differences, these are explicitly stated. The trigger and data requirements are also exactly the same for the two different analyses. The event selection for the SM WW measurement is provided in Section 4.7. The Higgs boson search is split into a cut-based approach and a matrix-element-based approach. Identical object selection is used for these two cases, but the global event selection differs and is described in Section 4.8 for the cut-based analysis and Section 4.9 for the matrix-element-based

Process	Generator	σ (pb) [$\times$ BR]	N_{ev}
Inclusive $W \to \ell\nu$	ALPGEN	10.5×10^3 [67, 68]	3.8M
Inclusive $W \to \tau\nu$	PYTHIA	10.5×10^3 [67, 68]	1M
Inclusive $Z/\gamma^* \to \ell\ell$ ($M_{\ell\ell} > 40$ GeV)	ALPGEN	10.7×10^2 [68, 69]	800K
Inclusive $Z/\gamma^* \to \tau\tau$ ($M_{\tau\tau} > 60$ GeV)	PYTHIA	9.9×10^2 [68, 69]	600K
Inclusive $Z/\gamma^* \to \ell\ell$ ($10 < M_{\ell\ell} < 40$ GeV)	ALPGEN	3.9×10^3 [69]	4M
Inclusive $Z/\gamma^* \to \tau\tau$ ($10 < M_{\ell\ell} < 60$ GeV)	PYTHIA	4.0×10^3 [69]	200K
$t\bar{t}$	MC@NLO	164.6	200K
Single top Wt	MC@NLO	13.1	13K
Single top s-channel	MC@NLO	3.9	25K
Single top t-channel	MC@NLO	58.7	18K
WZ	MC@NLO	18.0	250K
ZZ	MC@NLO	5.6	275K
$qq/qg \to WW \to \ell\nu\ell\nu(\ell = e, \mu, \tau)$	MC@NLO	4.7	320K
$gg \to WW \to \ell\nu\ell\nu(\ell = e, \mu, \tau)$	gg2WW	0.14	90K
$W\gamma \to \ell\nu\gamma(\ell = e, \mu, \tau)$	PYTHIA,MADGRAPH	135.4	200K
Dijet ($8 < p_T < 1120$ GeV)	PYTHIA	1.1×10^{10}	10M

Table 4.1: Cross sections for signal and background processes for SM WW production and background processes to $H \to WW$ production. All cross sections are given for a centre of mass energy of 7 TeV. The quoted cross sections for $W \to \ell\nu$ and $Z/\gamma^* \to \ell\ell$ are for each lepton flavour. The number of events in each sample, N_{ev}, is also shown.

analysis.

Unless otherwise stated, contributions to plots labelled as $H \to WW$ are a combination of ggF and VBF Higgs boson samples.

4.1 Monte Carlo modelling

The various MC generators used to model the signal and backgrounds for SM WW production and the background processes to $H \to WW$ are shown in Table 4.1.

The backgrounds due to W+jets, $Z \to \ell\ell$+jets, $Wb\bar{b}$+jets, and $Zb\bar{b}$+jets are modelled using ALPGEN [70] interfaced to HERWIG [71] for hadronisation. ALPGEN was chosen for these backgrounds because it appears to model the jet multiplicity distribution more accurately than other generators, such as PYTHIA. QCD backgrounds, including $b\bar{b}$ and dijets, are modelled using PYTHIA [72]. No events remain for these backgrounds after the selection of two opposite sign leptons, therefore these backgrounds are not shown in any of the plots or tables henceforth. PYTHIA is also used to model the $Z \to \tau\tau$ background, with the use of TAUOLA [73] to decay the taus. ALPGEN is not used for the $Z \to \tau\tau$ background since the τ polarisation is not correctly included in these samples due to an incorrect interface between ALPGEN and TAUOLA at the time the samples were produced.

The SM WW signal is modelled using MC@NLO [74] for the $q\bar{q}$ production mechanism and gg2WW [75] for the ggF production mechanism. MC@NLO is also used to model the ggF Higgs boson signal production mechanism. VBF Higgs boson production is handled by Sherpa [76].

All of these processes are generated at a centre of mass energy of 7 TeV. Detector

simulation, to model the detector response to the incident particles, is performed using GEANT4 [77, 78], which provides a full simulation of the ATLAS detector. Databases containing all the information about the physical construction and conditions are used to build the ATLAS detector geometry in order to accurately represent the detector for the simulation with GEANT4. Once an event has been propagated through the detector within GEANT4, the simulated energy deposits may be digitised into voltages and currents so that they can be compared to the readout of the detector. The output may be stored in a format indentical to that of the ATLAS data acquisition system and then run through the trigger and reconstruction software in exactly the same way as real data. Events may then be stored in a variety of different data formats, containing more or less information depending on their intended users. For the analyses presented in this thesis, both MC and data events were selected from ntuples produced by the SM WW group from larger, more detailed data formats, containing information at the object level as well as global quantities such as missing E_T and trigger decisions.

4.2 Data selection

In order to select data events which are consistent with a collision, the requirement of a primary vertex with at least three tracks consistent with the beam spot position is imposed. This reduces the contamination from events arising from cosmic ray muons traversing the detector or beam-related backgrounds. These effects, as well as noise in the calorimeters are further reduced by rejecting events containing hadronic jets which are consistent with these non-collision processes. In addition, quality criteria are applied to the data to remove events collected when parts of the detector were not functioning. ATLAS data are divided into periods, with each period containing data obtained with a coherent detector and trigger configuration.

4.3 Trigger selection

WW candidate events with dilepton final states are recorded using single muon and single electron triggers. The trigger p_T thresholds are different in different run periods due to the rapid increase in luminosity during the first year of LHC operation. Initially the HLT was not enabled, therefore only the L1 trigger could be used at the start of data-taking.

The triggers used in data and MC for events containing electrons in the final state are:

- Periods A-E3: L1_EM14
- Periods E4-I2: EF_e15_medium

where periods A-E3 correspond to 0.78 pb^{-1} and periods E4-I2 correspond to 34.4 pb^{-1} of integrated luminosity. For events with muons in the final state, the following triggers are used in data and MC:

- Periods A-E3: L1_MU10

- Periods E4-G1: EF_mu10_MG
- Periods G2-I1 (up to run 167576): EF_mu13_MG
- Periods I1 (from run 167607)-I2: EF_mu13_MG_tight

where periods A-E3, E4-G1, G2-I1 (up to run 167576), I1-I2 (from run 167607) correspond to 0.78 pb^{-1}, 3.0 pb^{-1}, 15.8 pb^{-1} and 15.6 pb^{-1} respectively. An OR is made between the electron and muon triggers for the $e\mu$ channel.

4.4 Lepton selection

To select electrons, liquid argon (LAr) electromagnetic calorimeter clusters matched to tracks [79] are used. Electron candidates are excluded if they lie in the pseudorapidity range $1.37 < |\eta| < 1.52$ where there is a crack region in the EM calorimeter. They are also required to be within the acceptance region of the EM calorimeter, which corresponds to $|\eta| < 2.47$. Electron candidates in regions where the optical transmitters used to record the events were malfunctioning are removed. Standard ATLAS tight identification requirements are imposed on the electron candidates [79]. The variables used for these tight requirements are detailed in Table 4.2.

These variables were optimised using a comparison of the distributions obtained in MC samples containing true electrons and jets faking electrons to try to maximise the rejection of hadrons falsely reconstructed as electrons. There are a few ways in which real electrons may be distinguished from fakes; real electrons will tend to have narrower shower widths and should deposit most of their energy within the EM calorimeter whereas jets reconstructed as electrons will have larger showers with more leakage into the hadronic calorimeter. Some relevant distributions are shown in Ref. [80].

In order to select electrons rather than photons, electron candidates are required to have an associated track, consistent with originating from the primary vertex. This consistency includes a requirement on the transverse impact parameter significance, defined as the ratio of the transverse impact parameter to its measured error, to be less than 10. In addition, the position of the track origin on the z-axis must be within 10 mm of the primary vertex. During further calculations of electron properties, the energy of the candidate is taken from the calorimeter cluster. Its angular variables, η and ϕ are taken from the track associated with the electron candidate.

To reduce the chance that jets are falsely reconstructed as electrons, electron candidates are required to be isolated. Requirements are placed on the scalar sum of the transverse momentum calculated using tracks (denoted by p_T^{track}) and calorimeter clusters (given by p_T^{calo}) lying within a cone defined by $\Delta R < 0.3$. For the SM WW cross section measurement, the calorimeter isolation is required to satisfy $p_T^{calo} < 6$ GeV. The requirements $p_T^{track}/p_T < 0.1$ and $p_T^{calo}/p_T < 0.15$ must be satisfied for the electron candidate to be considered for the $H \to WW$ search, where the p_T is measured by the EM calorimeter as described in Section 2.6.2.

It is sometimes possible for two electron candidates arising from the same original electron to be reconstructed separately. In this case, if two electrons are found to lie within $\Delta R < 0.1$, the candidate which is lower in p_T is discarded.

Detector acceptance
$\|\eta\| < 2.47$
Hadronic leakage
Ratio of E_T in the first sampling of hadronic calorimeter to the E_T of the EM cluster
Second layer of EM calorimeter
Ratio in η of cell energies in 3×7 versus 7×7 cells
Ratio in ϕ of cell energies in 3×7 versus 7×7 cells
Lateral width of shower
First layer of EM calorimeter
Difference between second largest energy deposit and minimal energy in between 1st & 2nd maxima
Second largest energy deposit normalised to cluster energy
Total shower width
Shower width for three strips around maximum strip
Fraction of energy outside core of three central strips but within seven strips
Track quality
At least one hit in the pixel detector
At least nine hits in the pixels and SCT
Transverse impact parameter < 1 mm
Isolation
Ratio of transverse energy in $\Delta R < 0.2$ to the total cluster E_T
Vertexing-layer
At least one hit in the vertexing-layer (first layer of the pixels)
Track matching
$\Delta\eta < 0.005$ between cluster and track
$\Delta\phi < 0.02$ between cluster and track
Ratio of the cluster energy to the track momentum
TRT
Total no. of hits in the TRT
Ratio of the no. of high-threshold hits to the total no. of hits in the TRT

Table 4.2: Variables used in the tight selection for electron candidates. For the sake of brevity, no cut values are shown for those variables which have E_T and η dependent cuts.

Muons are reconstructed by combining tracks in the Inner Detector (ID) and Muon Spectrometer (MS) to produce combined muons. To ensure a good match between ID and MS tracks in the WW analysis, the momentum measured by these detectors, after accounting for muon energy loss as it traverses the calorimeter, is required to be consistent. Specifically, the absolute difference between the p_T measured by the MS and the p_T measured by the ID divided by the p_T in the ID is required to be less than 0.5: $|(p_T^{MS} - p_T^{ID})/p_T^{ID}| < 0.5$, where the p_T^{MS} is required to be larger than 10 GeV. For the $H \to WW$ search, a good match is ensured by requiring the χ^2 of the spatial match between ID and MS tracks to be less than 150. A further requirement on the transverse momentum is applied in the $H \to WW$ analysis to remove muons occurring from π/K decays-in-flight: if the p_T measured by the MS only is less than 50 GeV, $p_{MS}^{extrapol.} - p_{ID}$ must be larger than $-0.4 \times p_{\mathrm{ID}}$. $p_{MS}^{extrapol.}$ refers to the transverse momentum as measured by the muon spectrometer and extrapolated back to the interaction point taking into account the energy loss due to ionisation inside the calorimeter. An additional requirement of a sufficiently large number of hits in the SCT and TRT ensures that the muon tracks are well identified in both analyses. Muons must also be within $|\eta| < 2.4$ for both the SM WW cross section measurement and the Higgs boson search. The isolation requirement

for the SM WW analysis is $p_T^{calo}/p_T < 0.1$ for muons, with a cone size of $\Delta R < 0.2$ where the p_T in the denominator is the combined muon p_T. Muons are required to satisfy the same impact parameter and isolation requirements as electrons for the $H \to WW$ search.

Both electrons and muons must have p_T larger than 20 GeV for the WW analysis. For the $H \to WW$ search, the requirement on the subleading lepton p_T is relaxed to 15 GeV to increase the kinematic acceptance. This is necessary to achieve sensitivity since the Higgs boson production cross section is small so the expected number of events with 35 pb^{-1} of data is small.

4.5 Jet selection

Topological clusters in the hadronic calorimeter are used to select jets. The reconstruction is performed using the anti-k_{T} algorithm [21–23] where the size parameter is set to 0.4. Jets must lie within $|\eta| < 4.5$ and have $p_T > 25$ GeV for the Higgs boson search. For jets within $|\eta| < 2.1$, the ratio of the sum of the p_T of tracks pointing back to the primary vertex with respect to the p_T sum of all the tracks in the jet must be larger than 0.75 to ensure that the hadronic activity registered in the event has originated from the primary interaction and is not from pileup or secondary interactions in the underlying event. b-jets are identified by the presence of a displaced secondary vertex as reconstructed using the SV0 algorithm [81]. This algorithm gives a weight to jets, with higher weights corresponding to jets with more prominent secondary vertices. In this case, b-jets are required to have an SV0 weight of more than 5.72, which gives a 50% efficiency for correctly identifying b-jets in $t\bar{t}$ events. For the WW cross section measurement, jets must have calibrated $p_T > 20$ GeV at the hadronic energy scale and $|\eta| < 3$.

4.6 Missing E_T selection

To reconstruct missing transverse energy, all calibrated calorimeter cells are used starting from topological energy clusters [82]. In addition, corrections are applied for particles which are not fully reconstructed in the calorimeter, for example muons in the muon spectrometer. This is described in more detail in Section 2.6.5.

For the SM WW cross section measurement, the variable $\not\!\!E_T^{\mathrm{Rel}}$ is used. This is defined as:

$$\not\!\!E_T^{\mathrm{Rel}} = \begin{cases} \not\!\!E_T \times \sin(\Delta\phi) & \text{if } \Delta\phi < \pi/2 \\ \not\!\!E_T & \text{if } \Delta\phi \geq \pi/2 \end{cases}$$

where $\Delta\phi$ is the phi difference between the missing E_T and the closest lepton or jet passing the selection requirements. This variable allows better rejection of events with missing E_T arising from mismeasured jet or lepton p_T, helping to reduce the background due to Z+jets events. The value of this cut value was optimised for the ee and $\mu\mu$ channels, and separately for the $e\mu$ channel, to give the best signal significance [83].

4.7 WW selection

To select WW events, the data are required to satisfy the criteria described in Section 4.2. Events are collected using the electron or muon triggers listed in Section 4.3 for the ee or $\mu\mu$ channels respectively. $e\mu$ events may be recorded by either trigger. After passing the trigger requirement, events are required to have exactly two opposite sign leptons which both have $p_T > 20$ GeV. This requirement selects events consistent with WW production and reduces contamination from many background processes including QCD, W+jets and WZ production. Distributions of variables used to extract the WW signal are shown in Figure 4.1. In this figure and all subsequent figures showing a comparison of distributions in data and MC, the MC predictions are normalised to correspond to the integrated luminosity of the data sample. The discrepancy at low M_{ll} between data and MC arises because the background due to low mass B-hadrons in this region has not been included. This is due to the very large MC samples which require a lot of CPU time to process; the contribution from this background is also expected to be small at this stage and negligible at all later stages in the WW selection.

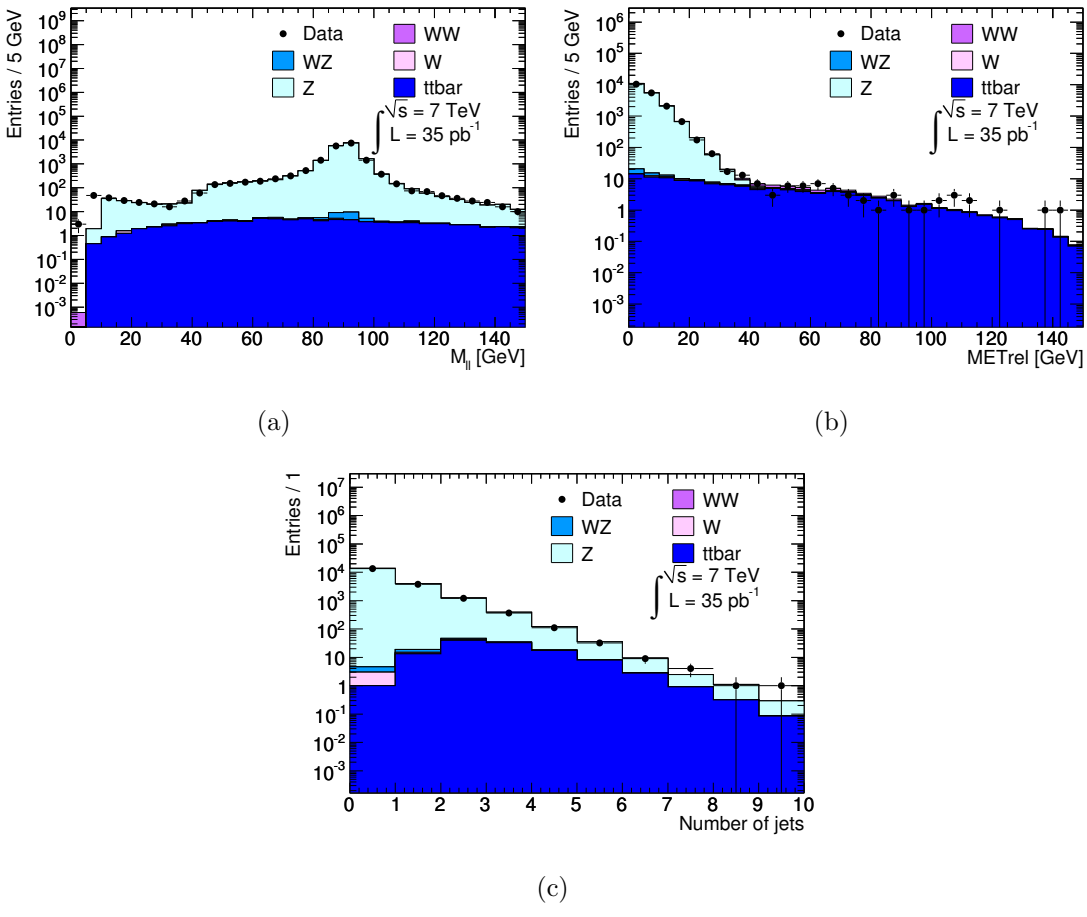

(a) (b)

(c)

Figure 4.1: Dilepton invariant mass (a), $\not\!\!E_T^{\mathrm{Rel}}$ (b) and jet multiplicity (c) distributions for events with two opposite sign dileptons passing WW object selection criteria.

Additional selection requirements are then imposed to select a clean sample of WW events, with contributions from other processes reduced to a small fraction of the sample.

The invariant mass of same-flavour (ee or $\mu\mu$) dilepton pairs, M_{ll}, is required to be larger than 15 GeV to remove any remaining QCD background such as Υ production, which has a mass just below 10 GeV. The background due to Z events, which is sizeable at the stage of requiring two opposite sign leptons, is reduced by vetoing same-flavour dilepton events in which M_{ll} is within ± 10 GeV of the Z boson mass. Remaining Z background is reduced by requiring $\not{E}_T^{\mathrm{Rel}} > 40$ GeV for ee and $\mu\mu$ events and $\not{E}_T^{\mathrm{Rel}} > 20$ GeV for $e\mu$ events. Finally the number of jets must be zero. This acts to significantly reduce contamination from the $t\bar{t}$ and single top backgrounds, in which two high p_T b-jets are generally produced.

A full discussion of the results of the WW cross section measurement is provided in Chapter 8, with the number of WW signal and background events at all stages of the event selection in data and MC shown in Table 8.2. Final event yields are given in Table 8.3. Event distributions throughout the cutflow and after all selections have been applied are shown in Figures 8.1 and 8.2 respectively.

4.8 Higgs boson selection using a cut-based approach

Common preselection for the three jet channels is applied to select Higgs boson candidate events, which is rather similar to the selection applied in the WW analysis. The same trigger selection is used as in the WW case and events with two opposite sign leptons are also selected. However, for the Higgs boson selection, the p_T requirement on the subleading lepton is lowered from 20 GeV to 15 GeV to try to gain the maximum possible acceptance while still keeping the backgrounds at an acceptable level. This is one area which may be optimised further in future versions of the analysis; for Higgs bosons with low mass, the leptons produced will have lower average p_T so any lowering of lepton p_T leads to a noticeable improvement in signal acceptance. The backgrounds due to W+jets and QCD processes may become problematic for lower p_T leptons, so more study is needed to understand and reduce these backgrounds. Also, the unprescaled single lepton trigger thresholds are higher than desired to achieve maximal acceptance, so lower threshold dilepton triggers are likely to be used in the future.

Reduction of the Υ background is performed in the same way as in the WW case, by requiring the invariant mass of the dileptons to be larger than 15 GeV. The lepton pair must also have an invariant mass outside the Z peak region with $|m_Z - M_{ll}| > 10$ GeV. The final stage of preselection requires that the missing E_T is larger than 30 GeV to reduce backgrounds arising from QCD or Z+jets.

Events passing the preselection are then divided into jet channels (zero, one or at least two jets), where specialised cuts are applied to remove backgrounds most prevalent in that specific jet channel. After passing these jet-specific cuts, events must finally pass topological cuts, which are designed to remove the WW background as much as possible. These cuts are discussed in Section 4.8.4.

Variables used to select Higgs boson events are shown in Figure 4.2 at the stage where two opposite sign dilepton events have been selected. A full description of the variables is provided in Section 4.8.4. These plots show that, in general, MC describes the data well. However, it is desirable to have data-driven estimates of background processes to reduce

the effect of any mis-modelling in MC; this is described in Chapter 6.

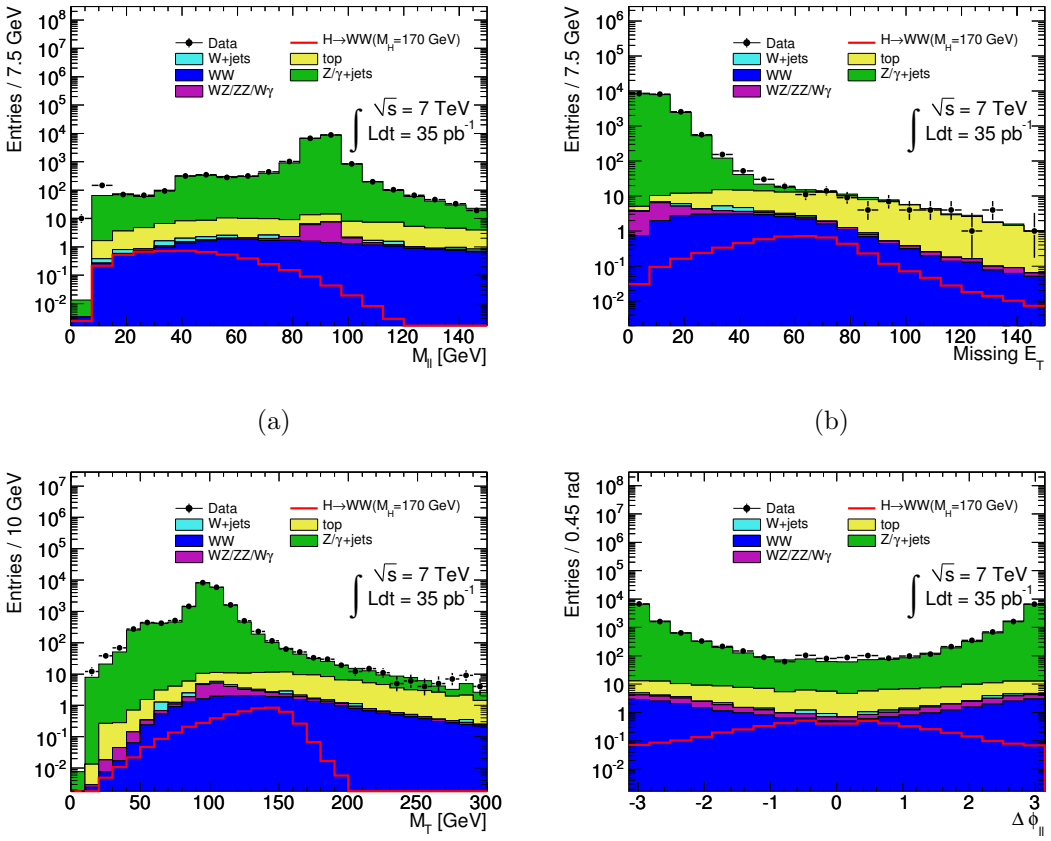

Figure 4.2: Dilepton invariant mass (a), missing E_T (b), transverse mass as defined in Equation 4.4(c) and $\Delta\phi$ between leptons (d) for events containing two opposite sign dileptons passing Higgs boson object selection criteria.

These cuts were optimised using a simple algorithm. Cuts on the variables described in this section, such as M_{ll}, missing E_T, $\Delta\phi_{ll}$ and m_T, were varied from no cut to a maximum and the signal significance was calculated for each possible combination of cuts. The cuts used for this analysis were chosen to be those which maximised the significance.

Figure 4.3 shows the jet and b-jet multiplicity distribution after requiring exactly two opposite sign leptons. This figure shows that the relative contribution of different backgrounds varies with jet multiplicity, with the top background becoming increasingly prominent as the number of jets in the event increases. The Higgs boson signal, with ggF and VBF contributions combined, is also shown on this plot and tends to have few jets per event. This is due to the large cross section of the ggF production mechanism, which tends to produce mainly zero or one jets, with respect to VBF, which tends to produce two or more jets per event.

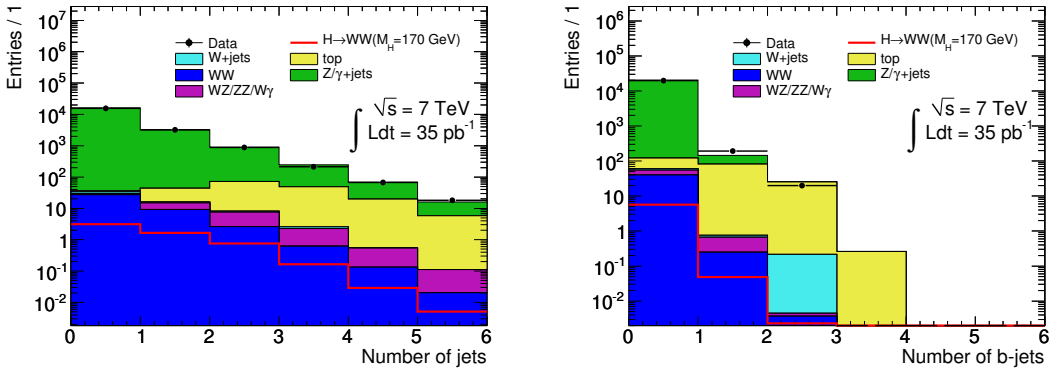

(a) (b)

Figure 4.3: Jet (a) and b-jet (b) multiplicity distributions for events containing two opposite sign dileptons passing Higgs boson object selection criteria.

4.8.1 Zero jet channel

To be considered for the zero jet channel, events must pass the preselection described in Section 4.8 and have no jets with $p_T > 25$ GeV within $|\eta| < 4.5$. Further cuts are additionally applied to separate the Higgs boson signal from backgrounds. The transverse momentum of the lepton pair, p_T^{ll}, is required to be larger than 30 GeV to reduce contamination from the Z background, which tends to have low values of p_T^{ll}. This distribution is shown in Figure 4.4 with the requirements of two opposite sign leptons and zero jets applied. After the p_T^{ll} cut, the topological cuts described in Section 4.8.4 are applied.

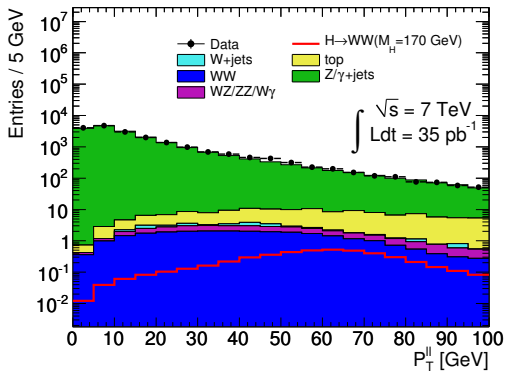

Figure 4.4: p_T^{ll} for dilepton pairs in events with two opposite sign dileptons passing Higgs boson selection criteria in the zero jet channel.

More details are provided in Chapter 9, with the event yields throughout the event selection shown in Table 9.3 and the transverse mass distribution in the zero jet channel given in Figure 9.1.

4.8.2 One jet channel

Events passing the preselection with one high-p_T jet fall into the one jet channel. In addition to satisfying the common preselection requirements, events containing b-jets are vetoed to reduce the top background. The total p_T of the event, defined as $p_T^{Tot} = |\mathbf{P}_T^{l1} + \mathbf{P}_T^{l2} + \mathbf{P}_T^{j} + \mathbf{P}_T^{miss}|$, must be less than 30 GeV to remove events with significant soft gluon radiation recoiling against the dilepton+jet system which does not produce any jets with p_T high enough to pass the cut at 25 GeV. This distribution is shown in Figure 4.5. If the event was measured perfectly, p_T^{Tot} would be expected to exactly zero. However, there may be some underlying hadronic energy which may give non-zero p_T^{Tot}, for example due to soft jets which have $p_T < 25$ GeV in addition to the one hard jet with $p_T > 25$ GeV. These soft jets would be included in the calculation of $\mathbf{P}_T^{miss}$, which is determined as described in Section 2.6.5 using a sum over all the energy deposited in the calorimeters, but would not be included in the vector sum over the p_T of the hard objects in the event (the leptons and the high-p_T jet), giving non-zero p_T^{Tot}. This cut is designed primarily to remove events of this sort, which arise from background events which have jets which fail the p_T cut of 25 GeV.

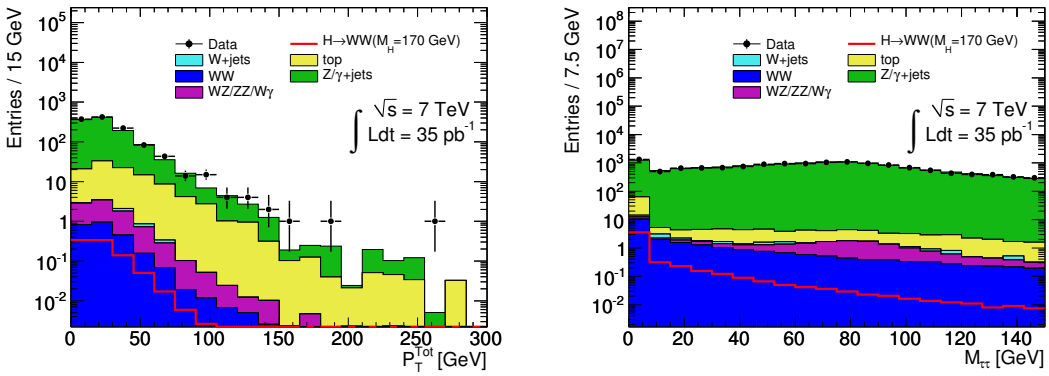

(a) (b)

Figure 4.5: p_T^{Tot} (a) and $M_{\tau\tau}$ (b) for events with two opposite sign dileptons passing Higgs boson selection criteria in the one and two jet channels.

This figure also shows the distribution of $M_{\tau\tau}$, the calculated invariant mass of the lepton pair assuming that the leptons have arisen from the decay of two τ leptons, as may happen in $Z \to \tau\tau$ events.

The $Z \to \tau\tau$ background may be significant in the $e\mu$ channel, therefore it must be reduced. To do this, it is necessary to calculate the invariant mass of the τ pair; di-τ masses which are consistent with the Z boson should be vetoed to remove this background. However, since neutrinos are produced during τ decays, the exact $M_{\tau\tau}$ cannot be calculated. Instead, the collinear approximation can be used, which assumes that the decay products of the τ are collinear with the τ itself, since the τ mass is small relative to its p_T. Using this approximation, the invariant mass of the $Z \to \tau\tau$ candidate, $M_{\tau\tau}$, may be calculated as:

$$M_{\tau\tau} = \frac{M_{ll}}{\sqrt{x_1 x_2}} \tag{4.1}$$

The momentum fractions x_1 and x_2 represent the fraction of τ momentum carried by each lepton and are calculated using:

$$x_1 = \frac{P_x^{l_1} P_y^{l_2} - P_y^{l_1} P_x^{l_2}}{P_y^{l_2} E_{\mathrm{x}}^{\mathrm{miss}} - P_x^{l_2} E_{\mathrm{y}}^{\mathrm{miss}} + P_x^{l_1} P_y^{l_2} - P_y^{l_1} P_x^{l_2}} \tag{4.2}$$

$$x_2 = \frac{P_x^{l_1} P_y^{l_2} - P_y^{l_1} P_x^{l_2}}{P_x^{l_1} E_{\mathrm{y}}^{\mathrm{miss}} - P_y^{l_1} E_{\mathrm{x}}^{\mathrm{miss}} + P_x^{l_1} P_y^{l_2} - P_y^{l_1} P_x^{l_2}} \tag{4.3}$$

If $x_1 \times x_2 < 0$, $M_{\tau\tau}$ is taken to be zero. The actual selection requirement which is enforced is $|M_{\tau\tau} - M_Z| < 25$ GeV.

Finally, the same topological cuts as are applied in the zero jet channel and described in Section 4.8.4 are applied to reduce the WW background.

Chapter 9 provides more information about the results. Within this chapter, Table 9.4 provides the number of expected events at all stages in the event selection for the one jet channel and the transverse mass after all cuts is shown in Figure 9.2.

4.8.3 Two jet channel

Higgs bosons produced by VBF have a distinctive topology of two high p_T jets which are well separated in η, in addition to the Higgs boson decay products, namely the leptons from the W decays. One of the main backgrounds to this process arises from top (mainly $t\bar{t}$) decays which also have a signature of two leptons, missing E_T and two jets. This background may be significantly reduced by applying topological cuts to the two highest p_T jets in the event, known as the 'tag' jets, and applying a veto on events containing b-tagged jets or additional high p_T jets in the central region. These topological cuts also strongly suppress other backgrounds such as QCD and W+jets.

Events must pass the initial preselection common to all three jet multiplicity channels as described in Section 4.8. $H + 2j$ events containing two or more jets with $p_T > 25$ GeV are required to satisfy some further cuts to reduce the top and other backgrounds.

The two tag jets are required to lie in opposite rapidity hemispheres, $\eta_{j1} * \eta_{j2} < 0$, where η_{j1} and η_{j2} are the pseudo-rapidity of the two tag jets and they must be separated in pseudorapidity by a distance $\Delta\eta_{jj}$ of at least 3.8 units. These two requirements select events which are consistent with the VBF topology and reduce the background processes, which tend to be symmetric in $\Delta\eta_{jj}$ and $\eta_{j_1}\eta_{j_2}$. The invariant mass of the tag jets, M_{jj}, must be at least 500 GeV since VBF events tend to have high M_{jj}.

There must also be no additional jets with $p_T > 25$ GeV lying in the central region of $|\eta| < 3.2$, since there is no colour exchange in the VBF process. Additionally, any events containing one or more b-jets are removed, since these are likely to come from $t\bar{t}$ events.

As in the one jet case, cuts are also applied on the p_T^{Tot} of the system and the $M_{\tau\tau}$ where in this case the p_T^{Tot} is defined as $p_T^{Tot} = |\mathbf{P}_T^{l1} + \mathbf{P}_T^{l2} + \mathbf{P}_T^{j1} + \mathbf{P}_T^{j2} + \mathbf{P}_T^{miss}|$. p_T^{Tot} is required to be less than 30 GeV and $|M_{\tau\tau} - M_Z|$ must be greater than 25 GeV, as in the one jet channel.

The final cuts are topological and are described in Section 4.8.4.

Distributions of the forward jet tagging variables $\eta_{j1} * \eta_{j2}$, $\Delta\eta_{jj}$ and M_{jj} are shown in Figure 4.6 for events containing at least two high-p_T jets in addition to two well identified

leptons. These distributions show that the jets in data are well-modelled by the MC. This figure also shows the SV0 b-tagging weight, which is used to define b-jets.

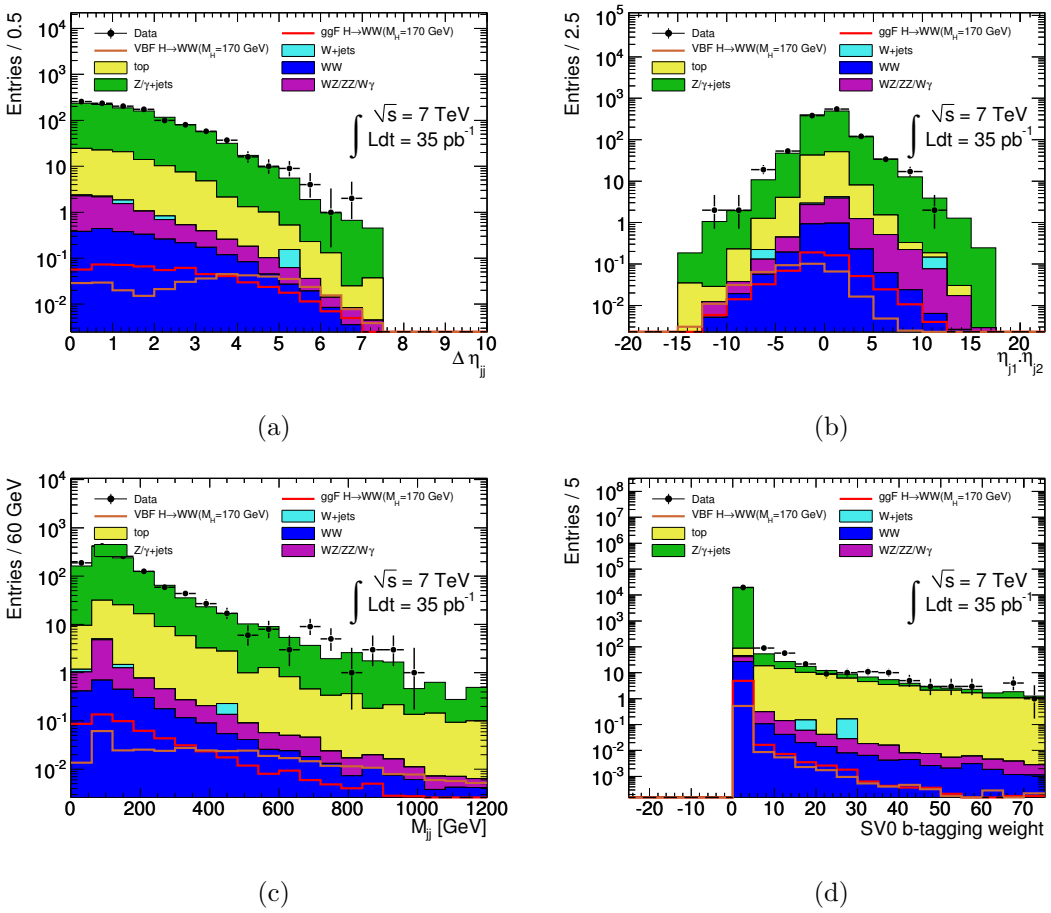

Figure 4.6: Distributions relevant to the Higgs boson search in the two jet channel for events with two opposite sign leptons and two jets: $\Delta\eta$ between the two tag jets (a), $\eta_{j_1} * \eta_{j_2}$ (b), invariant mass of the tag jets (c) and SV0 b-tagging weight (d).

More discussion is given in Chapter 9, with expected and observed event numbers throughout the cutflow shown in Table 9.5. Figure 9.3 shows the transverse mass distribution after all selections have been applied.

4.8.4 Topological cuts

Due to the spin-0 nature of the Higgs boson, the two leptons produced from the WW decays from the $H \rightarrow WW$ process tend to travel roughly in the same direction. This phenomenon is described in more detail in Section 3.2.3. Because of this, there are expected to be differences in some kinematic variables which may be exploited to separate the Higgs boson signal from the continuum WW background.

The invariant mass of the dilepton pair is required to be less than 50 (65) GeV for low (high) Higgs boson masses in the zero and one jet channels. The low mass region is defined as $m_H < 170$ GeV, with the high mass region occupying $m_H \geq 170$ GeV, where these regions were optimised for the best significance. For the two jet channel, M_{ll} is

required to be less than 80 GeV. A further requirement is applied on the difference in ϕ between the two leptons, $\Delta\phi_{ll}$, which is required to be less than 1.3 (1.8) radians for low (high) mass Higgs bosons. A final topological requirement is made on the transverse mass, m_T, of the system which is defined as [84]:

$$m_T = \sqrt{(E_T^{\ell\ell} + E_T^{miss})^2 - (\mathbf{P}_T^{\ell\ell} + \mathbf{P}_T^{miss})^2}, \tag{4.4}$$

where $E_T^{\ell\ell} = \sqrt{(\mathbf{P}_T^{\ell\ell})^2 + M_{\ell\ell}^2}$, $|\mathbf{P}_T^{miss}|$ = missing E_T and $\mathbf{P}_T^{\ell\ell}$ is the transverse momentum of the dilepton system.

These topological cuts are the final cuts applied in the cut-based $H \to WW$ search in all jet channels.

4.9 Higgs boson selection using a matrix-element-based approach

Loose preselection is applied to select events consistent with the $H \to WW$ topology before calculating the matrix element discriminant associated with each event. The discriminant separates Higgs boson events from SM WW events, as described in Chapter 7. It is not designed explicitly to separate Higgs boson events from other background processes, therefore it is necessary to apply some loose preselection to reduce other sources of background without unnecessarily reducing the signal acceptance.

The preselection consists of selecting events with two opposite sign dileptons passing the same trigger and lepton selection criteria as is used in the cut-based $H \to WW$ search. The requirement $|m_Z - M_{ll}| > 15$ GeV is imposed. This is slightly tighter than that used for the cut-based $H \to WW$ search, which uses $|m_Z - M_{ll}| > 10$ GeV. This is to ensure that there is no overlap between the $H \to WW$ and $H \to ZZ$ signal regions, since the $H \to ZZ$ search uses a Z peak region of $|m_Z - M_{ll}| < 15$ GeV to define the signal region. It is not desirable to have an overlap in signal regions between two Higgs boson search channels since this complicates the combination procedure when trying to obtain a combined limit. Hence, it is likely that future versions of the cut-based $H \to WW$ search will use $|m_Z - M_{ll}| > 15$ GeV.

The final preselection requirement is $\not{E}_T^{\mathrm{Rel}} > 25$ GeV for all three lepton channels to further reduce the Z+jets background. The selected sample is then further split up into three jet channels: zero, one and two or more jets. This allows the matrix element method to be optimised separately for each channel, with additional cuts to reduce other backgrounds which the matrix element discriminant does not necessarily remove. This is described in Chapter 10. This chapter also provides a thorough discussion of the results of the matrix-element-based Higgs boson search. The number of events in the ee, $\mu\mu$ and $e\mu$ channels throughout the event selection as well as the expected signal and background yields after preselection are given in Tables 10.1—10.4.

Chapter 5

Efficiency and acceptance corrections

There are certain effects measured in data and corrected in MC to match the data. These include the number of interactions in addition to the hard process, lepton trigger and identification efficiencies and the efficiency with which jets are reconstructed. This chapter discusses how these effects are modelled for the WW analysis. For the $H \to WW$ search, a similar approach is used, as outlined in Section 5.5.

5.1 Primary vertex correction

The number of interactions in addition to the primary hard scatter changes with instantaneous luminosity: higher luminosity results in more additional pileup interactions. The number of pileup interactions in an event can be reasonably characterised by the number of primary vertices in the event. There is a difference in the distribution of number of primary vertices in MC and data. The pileup conditions in data were constantly changing throughout the running period as the instantaneous luminosity continuously increased, leading to increasing numbers of primary vertices per event. The MC was generated with a constant mean number of primary vertices equal to two in addition to that of the hard scatter. Therefore, the MC must be corrected so that the primary vertex distribution matches that in data. This is performed by calculating the ratio of data and MC as a function of number of primary vertices and then reweighting the MC primary vertex distribution with this factor, a process known as pileup reweighting. The resulting weight is carried through the entire analysis procedure.

This process assumes that the primary vertex reconstruction efficiency is the same in data and MC. This efficiency has been measured in data and shown to be $\sim$100% [85], in good agreement with MC.

The primary vertex distributions in data and MC with no correction and after pileup reweighting are shown in Figure 5.1. This figure shows that after reweighting, the MC is in good agreement with the data.

5.2 Trigger scale factor calculation

The trigger efficiencies for WW events, ϵ, are measured using the tag and probe method described in Section 5.2.1. It is assumed that the ratio of efficiencies measured using the

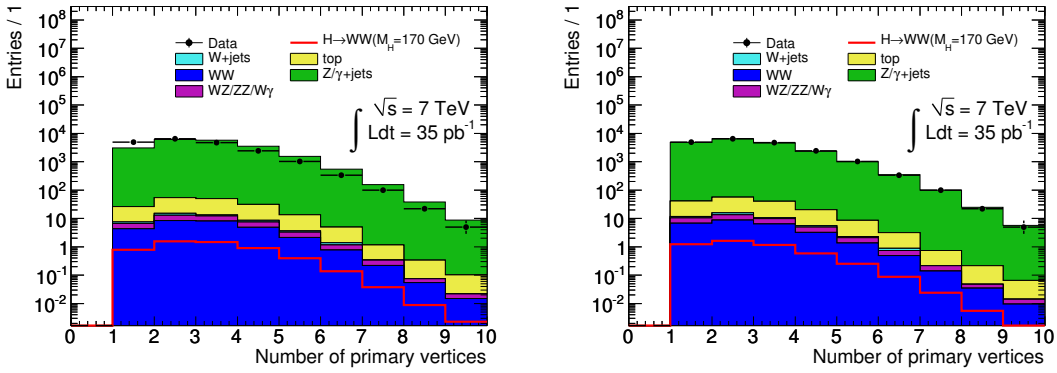

(a) (b)

Figure 5.1: Primary vertex distributions in data and MC before (a) and after (b) pileup reweighting.

tag and probe method is equivalent to the true ratio of efficiencies in the data and MC samples.

From these efficiencies, a per-lepton scale factor, SF, quantifying the difference between the trigger efficiency measured in data and MC can be defined as:

$$SF = \frac{\epsilon(Z, Data)}{\epsilon(Z, MC)}. \tag{5.1}$$

5.2.1 Tag and probe method for trigger efficiencies

To calculate the trigger efficiencies in data, the tag and probe method is used. This method selects a pure sample of events with well-identified leptons and uses these leptons to determine the trigger efficiency. For this analysis, a sample of Z events is selected from the full dataset using the following cuts:

- Two opposite sign leptons passing selection criteria as described in Section 4.4. For the muon channel, the p_T cut on the probe muon is lowered to $p_T^{MS,extrapol.} > 10$ GeV, where $p_T^{MS,extrapol.}$ is as defined in Section 4.4.

- $|m_Z - M_{ll}| < 12, 20$ GeV for electrons and muons respectively

A comparison of the number of Z events seen in data using these cuts and the number expected from MC is shown in Figure 5.2 for the ee channel and shows reasonable agreement. There is a slight discrepancy in the shapes between data and MC since no electron smearing or energy scale factor is applied to the MC. However, this is expected to have only a small effect on the determination of the trigger efficiencies.

Matching is performed between each lepton and the trigger region of interest (RoI) to determine if it was that particular lepton which fired the trigger. Leptons are considered matched if the ΔR between the trigger RoI and the offline lepton object, defined as $\Delta R = \sqrt{(\Delta\eta)^2 + (\Delta\phi)^2}$, satisfies the criteria shown in Table 5.1.

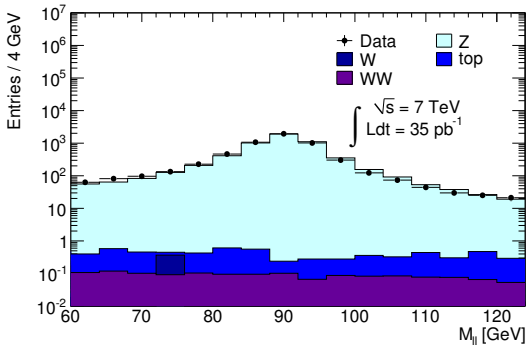

Figure 5.2: Di-electron invariant mass around the Z boson peak for data and MC with no electron smearing or energy scale factor applied.

	ΔR cut	
Trigger level	Electrons	Muons
L1	0.15	0.40
L2	0.05	0.20
EF	0.05	0.20

Table 5.1: Table showing the cut values used for ΔR matching between leptons and trigger RoIs. Leptons are considered matched to an RoI if the ΔR between the offline object and the trigger RoI is less than the cut value indicated above. The use of different ΔR cuts is historical; the same cut values could be used for both electrons and muons with no effect on the final calculated efficiency.

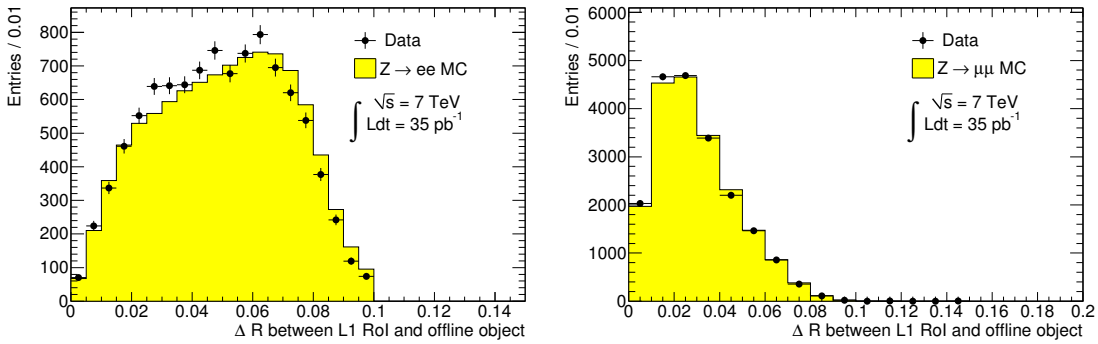

(a) (b)

Figure 5.3: Distributions of ΔR between trigger RoI and offline electrons (a) and muons (b) for RoIs calculated at L1.

The values for the ΔR matching were chosen to ensure that all of the leptons which arise from Z decays and fire the trigger are correctly counted as matched. The ΔR distributions for Z data and MC for electrons and muons, as shown in Figure 5.3 for the L1 trigger, show that the distributions have fallen off well before the ΔR cut values. A similar result is seen at all the trigger levels.

If a lepton matches the trigger RoI and the event satisfies the above criteria, it is considered a 'tag' lepton. The other lepton is then identified as the 'probe' and the trigger efficiency is defined as:

$$\epsilon = \frac{N_{probes}^{matched}}{N_{probes}} \tag{5.2}$$

For each event there are two possible tag leptons. This method is applied to both data and MC and a comparison is performed in the next section.

5.2.2 Electron trigger efficiency

The triggers used in data and MC for events containing electrons in the final state are:

- Periods A-E3: L1_EM14
- Periods E4-I2: EF_e15_medium

As described earlier, an OR is made between the electron and muon triggers for the $e\mu$ channel.

Comparison of data and MC trigger efficiencies

In order to evaluate the scale factor it is necessary to calculate the trigger efficiency using the tag and probe method on both data and MC. This is calculated for each trigger separately and then a luminosity weighted average is taken. The same method is used for the calculation of the scale factor.

To determine if the scale factor shows any dependence on the electron kinematics, it is useful to compare the distributions of some kinematic variables for the probe electrons in data and MC. Figure 5.4 shows good agreement between data and $Z \rightarrow ee$ MC for probe p_T, η and ϕ. The difference between MC and data remains approximately constant as a function of these kinematic variables, indicating that the scale factor is roughly independent of p_T, η and ϕ. This allows a constant scale factor to be defined, which differs from the muon case in which a different scale factor is required for the barrel and endcap regions.

The trigger efficiencies in data and MC are compared as a function of p_T, η and ϕ for the full dataset. All these distributions, shown in Figure 5.5, demonstrate the good agreement between the data and MC, as well as the consistently high efficiency of these triggers.

Scale factor calculation

A comparison between the triggers used in data and MC and the corresponding single electron scale factor is made in Table 5.2. The luminosity-weighted efficiency of the triggers in MC is 0.991 ± 0.00008(stat). For data, the efficiency is 0.990 ± 0.001(stat), giving a scale factor of 0.999 ± 0.001(stat). This suggests that the MC models the data very well. These efficiencies are quoted with statistical errors only; a discussion of systematic errors is given in the following section.

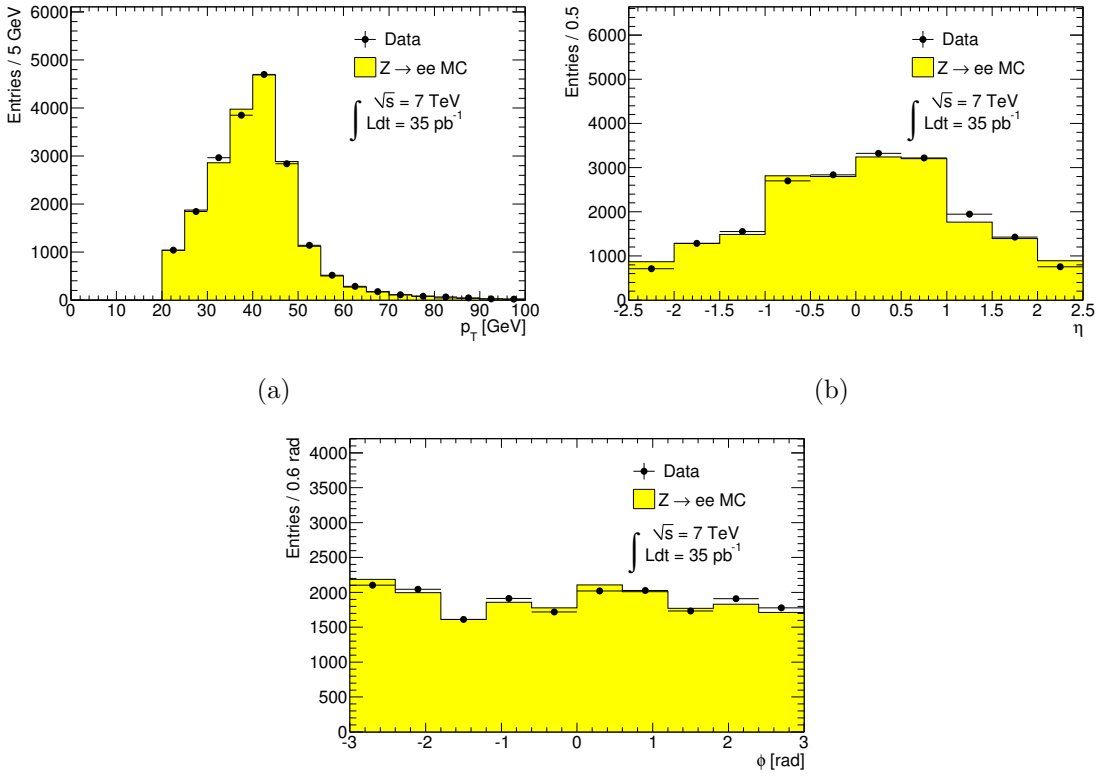

Figure 5.4: Distributions of p_T (a), η (b) and ϕ (c) for probe electrons in data and $Z \to ee$ MC.

Trigger	Data efficiency	Scale factor
L1_EM14	$0.990^{+0.006}_{-0.009}$	$0.999^{+0.006}_{-0.009}$
EF_e15_medium	0.990 ± 0.001	0.999 ± 0.001
Combined	0.990 ± 0.001	0.999 ± 0.001

Table 5.2: Trigger efficiencies and single electron scale factors with statistical uncertainties only for electron triggers used in data.

Systematic uncertainties on trigger scale factor

There are several sources of systematic uncertainty which should be considered when evaluating the scale factor. These sources include the effect of varying the cut on $|M_{ll} - M_Z|$ which may result in a sample of Z events with different levels of background and may affect the trigger efficiencies and hence the scale factor. Similarly, the electrons used are required to be isolated to reduce the contamination from hadrons misreconstructed as electrons. The effect of this isolation requirement is included as a source of systematic uncertainty. The scale factor has been calculated using the ratio of data to $Z \to ee$ MC, however there is expected to be some small contamination from background events in data. Figure 5.2 shows that this contamination is small but it should still be included as a source of systematic uncertainty and is done so by calculating the change in the

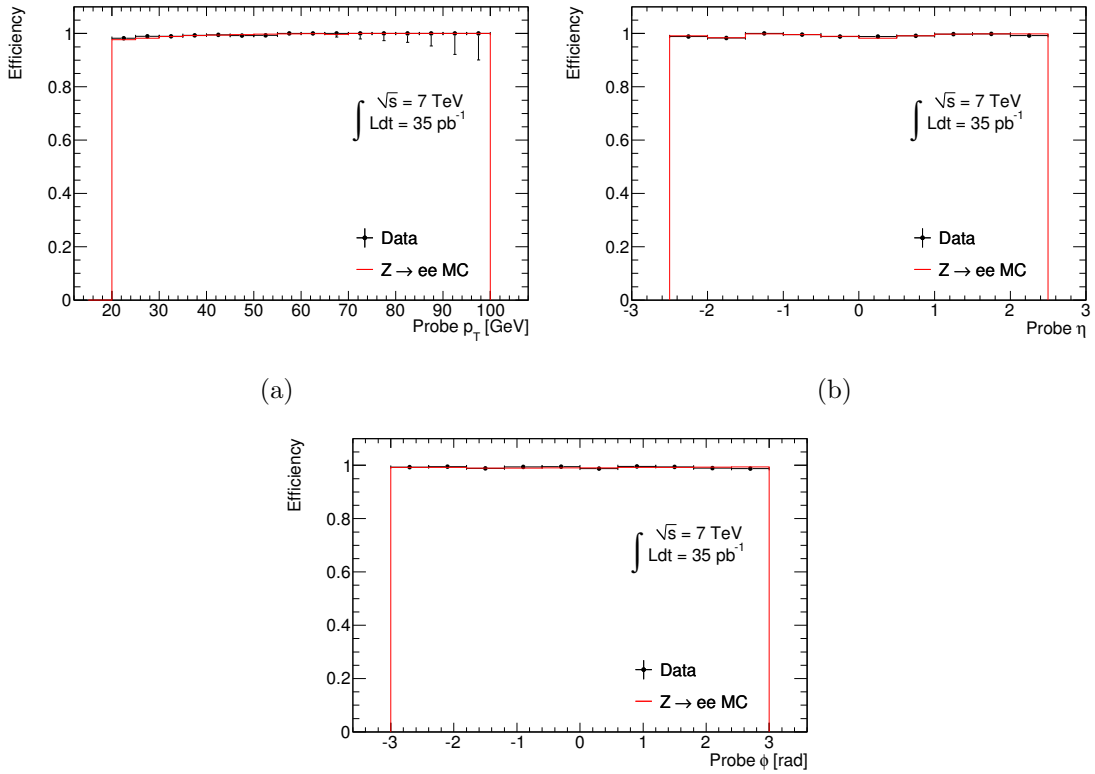

(a) (b)

(c)

Figure 5.5: Trigger efficiency as a function of p_T (a), η (b) and ϕ (c) for probe electrons in data and $Z \to ee$ MC.

scale factor when all the background samples, correctly weighted, are used instead of just the $Z \to ee$ sample. A further source of systematic uncertainty comes from the assumption that the scale factor is constant as a function of η. To model this, the maximum deviation of the measured efficiency as a function of η from the central value is taken as the systematic uncertainty arising from any η-dependence of the scale factor.

Uncertainty	SF	ΔSF ($\times 10^{-4}$)
Original	0.9985	-
$\lvert M_{ll} - M_Z \rvert < 10$ GeV	0.9989	-3.7
$\lvert M_{ll} - M_Z \rvert < 15$ GeV	0.9985	+0.10
Unisolated electrons	0.9985	+0.27
Background contamination	0.9985	-0.53
η-dependence (upper)	0.9987	+2.0
η-dependence (lower)	0.9983	-2.0

Table 5.3: Systematic uncertainties on the electron trigger scale factor.

These uncertainties are summarised in Table 5.3. When added in quadrature with the statistical uncertainty for the full dataset, the resulting scale factor is calculated to be SF $= 0.999 \pm 0.001$(stat) ± 0.0004 (syst) $= 0.999 \pm 0.001$(stat+syst).

Period	Barrel efficiency	Endcap efficiency
A-E3	$(78.30 \pm 2.69)\%$	$(84.76 \pm 2.48)\%$
E4-G1	$(74.51 \pm 1.39)\%$	$(94.85 \pm 0.80)\%$
G2-167576	$(78.09 \pm 0.55)\%$	$(94.84 \pm 0.32)\%$
167607-I2	$(76.96 \pm 0.56)\%$	$(92.47 \pm 0.38)\%$
Luminosity-weighted average	$(77.30 \pm 0.37)\%$	$(93.56 \pm 0.24)\%$
MC	$(78.20 \pm 0.10)\%$	$(91.98 \pm 0.06)\%$
Ratio	0.9862 ± 0.0048	1.0157 ± 0.0025

Table 5.4: Trigger efficiencies for muons with $p_T > 20$ GeV for four trigger periods, together with the average trigger efficiencies and data/MC scale factors. Only statistical uncertainties are included.

5.2.3 Muon trigger efficiency

For events with muons in the final state, the following triggers are used in data and MC:

- Periods A-E3: L1_MU10
- Periods E4-G1: EF_mu10_MG
- Periods G2-I1 (up to run 167576): EF_mu13_MG
- Periods I1 (from run 167607)-I2: EF_mu13_MG_tight

The average muon trigger efficiency is calculated using the same method as is used for electrons. The integrated luminosity in different trigger periods is taken into account to correctly weight any differences in efficiency over the course of running.

The efficiency for muon triggers is calculated separately in the barrel and endcap regions. This is due to the L1 muon coverage, which is lower in the barrel region than the endcap region. These efficiencies are shown in Table 5.4.

Possible sources of systematic uncertainty on the scale factor include the cone size used for the matching between the offline muons and the online trigger objects, the contamination due to the QCD background, the size of the mass window used to select Z events and finally the possible η-dependence of the scale factor. These sources are varied to give an estimate of the systematic error associated with the measurement to give a final data/MC scale factor for the muon trigger of 0.986 ± 0.007 (1.016 ± 0.006) for the barrel (endcap).

5.2.4 Event-based scale factor calculation

There are two charged leptons in this analysis, so there are two chances to pass a single-lepton trigger. Therefore it is necessary to define an event-based scale factor which is dependent on the lepton-based scale factor given by Equation 5.1. Assuming a constant scale factor, the event-based scale factor for events with l_1 and l_2, where $l = e, \mu$, is defined as:

$$SF_{l_1,l_2} = \frac{1 - [1 - \epsilon_{l_1}(Z, data)][1 - \epsilon_{l_2}(Z, data)]}{1 - [1 - \epsilon_{l_1}(Z, MC)][1 - \epsilon_{l_2}(Z, MC)]} \tag{5.3}$$

This may be rearranged to give:

$$SF_{l_1,l_2} = \frac{1 - [1 - \epsilon_{l_1}(Z, MC) \times SF_{l_1}][1 - \epsilon_{l_2}(Z, MC) \times SF_{l_2}]}{1 - [1 - \epsilon_{l_1}(Z, MC)][1 - \epsilon_{l_2}(Z, MC)]} \tag{5.4}$$

There are 6 possible WW final states: ee, $\mu\mu$ (barrel-barrel), $\mu\mu$ (endcap-endcap), $\mu\mu$ (barrel-endcap), $e\mu$ (barrel) and $e\mu$ (endcap), where barrel and endcap denote where the muon lies in the detector. Using Equation 5.4, the event-based scale factors can be calculated for each scenario separately. These results are shown in Table 5.5.

Channel	SF	Error on SF
ee	0.99998	0.00008
$\mu\mu$ (barrel-barrel)	0.995	0.001
$\mu\mu$ (endcap-endcap)	1.0021	0.0002
$\mu\mu$ (barrel-endcap)	1.0025	0.0006
$e\mu$ (barrel)	0.9997	0.0002
$e\mu$ (endcap)	1.00007	0.00007

Table 5.5: Event-based trigger scale factors with statistical and systematic uncertainties combined. Scale factors are shown separately for muons lying in the barrel and endcap regions.

Using the expected proportion of $\mu\mu$ events in WW MC with both muons in the barrel, both in the endcap and one in each region, a weighted $\mu\mu$ event-based scale factor can be calculated for WW events. This method is also used to determine the average $e\mu$ event-based scale factor, and Table 5.6 summarises the overall scale factors and their associated uncertainties for each channel: ee, $\mu\mu$ and $e\mu$.

Channel	SF	Error on SF
ee	0.99998	0.00008
$\mu\mu$	1.0002	0.0004
$e\mu$	0.9998	0.0001

Table 5.6: Event-based trigger scale factors averaged over all regions with statistical and systematic uncertainties combined.

5.3 Lepton identification efficiency

Lepton identification efficiencies are determined in data and MC using the same tag and probe method as is used to determine the trigger efficiencies. The electron and muon efficiencies are determined separately and are discussed in the following sections.

5.3.1 Electron identification efficiency

There are multiple factors which affect the overall efficiency with which electrons are reconstructed and pass the identification criteria described in Section 4.4. These factors are threefold:

- The efficiency with which electrons are initially reconstructed.
- The efficiency of reconstructed electrons to pass the identification criteria, which, in this analysis, are the standard ATLAS tight requirements described in Table 4.2.
- The efficiency of reconstructed electrons which pass the identification criteria to additionally pass the isolation requirements.

The first factor is common to all ATLAS analyses using electrons. The second factor is also common to many analyses involving electrons, although some may choose more relaxed identification criteria (medium criteria instead of tight). Because of this overlap, these efficiencies are determined centrally by the ATLAS electron and photon working group and are documented in [79]. The final factor is specific to the WW analysis and was determined using the tag and probe method [83].

Each of these factors can be combined to give an overall electron identification efficiency in data, as well as a data/MC scale factor which is used to correct the MC, both calculated in 8 η bins. These are shown in Tables 5.7 and 5.8.

η bin	[-2.47,-2.01]	[-2.01,-1.52]	[-1.37,-0.8]	[-0.8,0]
Efficiency	0.638 ± 0.035	0.665 ± 0.032	0.715 ± 0.033	0.771 ± 0.031
Scale factor	0.910 ± 0.039	0.988 ± 0.032	0.986 ± 0.029	0.975 ± 0.027

Table 5.7: Electron identification efficiencies in data, and data/MC scale factors for $-2.47 < \eta < 0$ used in the SM WW cross section measurement.

η bin	[0,0.8]	[0.8,1.37]	[1.52,2.01]	[2.01,2.47]
Efficiency	0.784 ± 0.031	0.75 ± 0.037	0.685 ± 0.053	0.643 ± 0.043
Scale factor	0.982 ± 0.027	1.024 ± 0.033	1.020 ± 0.050	0.916 ± 0.039

Table 5.8: Electron identification efficiencies in data and data/MC scale factors for $0 < \eta < 2.47$ used in the SM WW cross section measurement.

Investigations using $W \to e\nu$ events revealed that there is a possible E_T dependence to the data/MC scale factor. This is included as an additional uncertainty as a function of E_T as shown in Table 5.9. Overall, this corresponds to a total additional uncertainty on the WW acceptance of 6% in the ee channel and 3.4% in the $e\mu$ channel. The additional E_T-dependent uncertainty is added in quadrature with the η-dependent uncertainty to give a total uncertainty which depends on the electron's E_T and η.

5.3.2 Muon identification efficiency

The reconstruction and identification efficiency for muons is determined in the same way as electrons, using the tag and probe method on $Z \to \mu\mu$ events. The overall efficiency is formed from the product of the following three factors:

E_T bin	[20,25]	[25,30]	[30,35]	[35,40]	[40,45]	Above 45
Additional relative uncertainty	0.16	0.05	0.01	0.01	0.01	0.03

Table 5.9: Additional relative uncertainty on the electron efficiency scale factor as a function of E_T used in the SM WW cross section measurement.

- The probability for an isolated muon track to be reconstructed by the muon spectrometer.
- The probability for a muon reconstructed by the muon spectrometer to match an inner detector track, ϵ_{ID}. The inner detector track must satisfy the requirements on hits and $|p_T^{ID} - p_T^{MS}|/p_T^{ID} < 0.5$ as described in Section 5.3.
- The probability for a combined muon to be isolated, ϵ_{Iso}.

These efficiencies are shown in Table 5.10. Overall, reasonable agreement is seen between data and MC, with a data/MC scale factor of 0.980 ± 0.008. Further details are given in [83].

Efficiency type	Data eff.	MC eff.	Data/MC scale factor
ϵ_{CB}	0.932 ± 0.0017	0.948 ± 0.0003	0.983 ± 0.002(stat) ± 0.007(syst)
ϵ_{ID}	0.990 ± 0.0007	0.992 ± 0.0001	0.998 ± 0.001(stat) ± 0.003(syst)
ϵ_{Iso}	0.993 ± 0.0006	0.994 ± 0.0001	0.999 ± 0.0006(stat ± 0.004(syst)
ϵ_{Total}	0.916 ± 0.0019	0.935 ± 0.0003	0.980 ± 0.008

Table 5.10: Muon reconstruction and identification efficiencies in data and MC and data/MC scale factors used in the SM WW cross section measurement.

5.4 Jet veto efficiency

For the WW analysis, a jet veto is applied: all events containing one or more jets are rejected. This is designed to remove the contamination from the top and QCD backgrounds, which become more significant with increasing jet multiplicity. The ratio of the number of events passing all the event selection and the jet veto to the total number of events passing event selection (excluding the jet veto) is defined as the jet veto efficiency:

$$\epsilon = \frac{N_{njets=0}}{N_{njets\geq 0}} \tag{5.5}$$

This quantity may be calculated using MC but suffers from significant theoretical and experimental uncertainties. Therefore, it is preferable to calculate this using a data-driven method and correct the MC with the derived scale factor.

The jet veto efficiency in WW data may be calculated using:

$$\epsilon_{WW}^{data} = \epsilon_{Z}^{data} \frac{\epsilon_{WW}^{MC}}{\epsilon_{Z}^{MC}} \tag{5.6}$$

where ϵ is as defined in Equation 5.5.

Z events are selected in data and MC using the same criteria as in Section 5.2.1. WW events are required to pass the full event selection described in Section 4.7 with the exception of the jet veto. The same event generator, MC@NLO, [74], is used for both Z and WW MC to ensure the same theoretical treatment of jets.

The jet multiplicity distributions are shown in Figures 5.6 and 5.7 for the ee and $\mu\mu$ channels respectively. The figures show how the distributions vary with increasing jet p_T threshold, with more events passing the jet veto as the p_T threshold is raised.

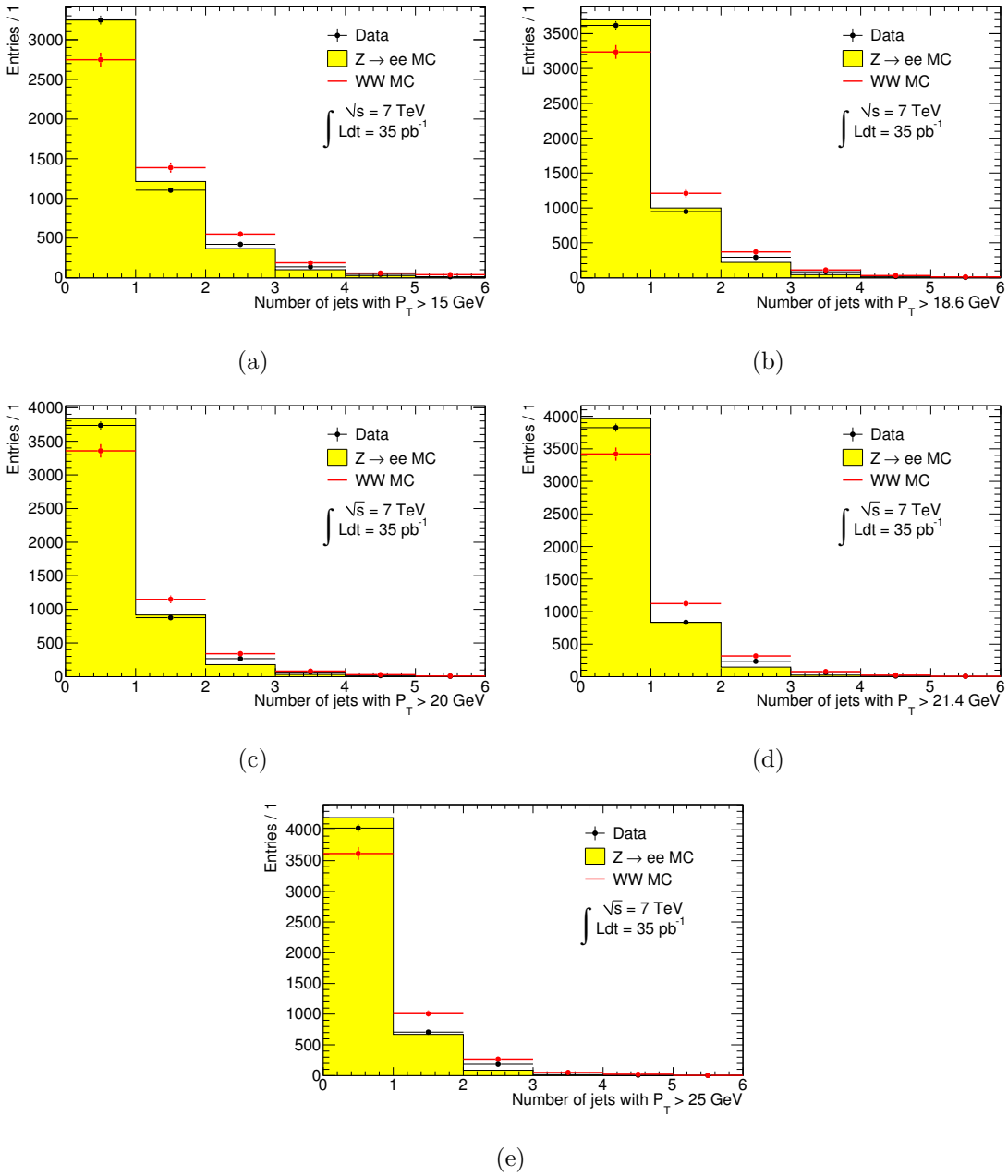

Figure 5.6: Jet multiplicity distributions for Z and WW MC and data for the ee channel in the SM WW cross section measurement. Jet p_T thresholds are at 15 (a), 18.6 (b), 20 (c), 21.4 (d) and 25 (e) GeV.

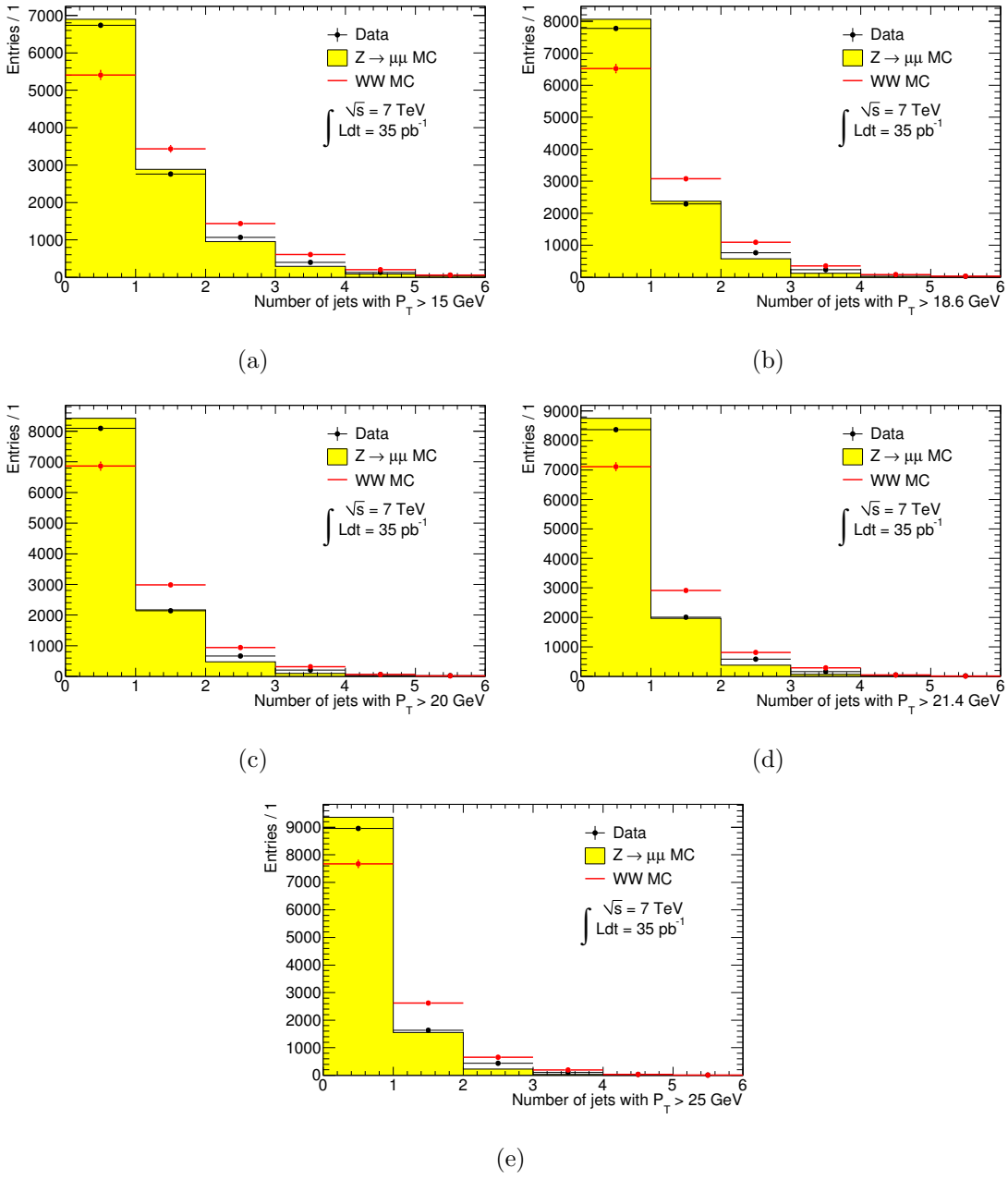

Figure 5.7: Jet multiplicity distributions for Z and WW MC and data for the $\mu\mu$ channel in the SM WW cross section measurement. Jet p_T thresholds are at 15 (a), 18.6 (b), 20 (c), 21.4 (d) and 25 (e) GeV.

There are various sources of systematic uncertainty which must be considered when undertaking this calculation. There are small statistical uncertainties associated with the measurements of the efficiencies, with the dominant statistical uncertainty arising from the measurement of ϵ_Z^{data}. Clearly, this will be significantly reduced once the dataset increases. ϵ_Z^{data} also suffers from an uncertainty due to contamination from other background processes. This is studied in Section 5.2 and is found to be negligible.

There are additional uncertainties arising from the choice of factorisation and renormalisation scales which affect the MC prediction of $\frac{\epsilon_{WW}^{MC}}{\epsilon_Z^{MC}}$. This ratio is also sensitive to

uncertainties on the PDFs. Studies at the parton level [86] suggest that these factors give rise to a theoretical uncertainty on this ratio of ≈ 0.05.

Another source of uncertainty arises in the choice of Z peak region definition, which is used to select events for the Z data and MC samples. Any mismodelling of the M_{ll} distribution may cause differences in the Z mass distribution between data and MC, which may result in differences in the jet veto efficiency. This was investigated by changing the definition of the Z peak region from $|m_Z - M_{ll}| < 12$ GeV to $|m_Z - M_{ll}| < 10$ and 15 GeV and was found to be a small effect at less than 0.1%.

The final source of uncertainty considered here is that arising from the jet energy scale (JES). This is investigated by altering the jet p_T thresholds up and down by the 1 σ uncertainty on the JES. A $\pm 1\sigma$ uncertainty on JES corresponds to a change in the jet p_T threshold of ± 1.4 GeV. These shifted jet p_T thresholds were applied to all the MC samples and the jet veto efficiency was recalculated to determine how much changes in JES affect the calculated jet veto efficiency. This is a very simple method of calculating the effect of the JES, which turns out to slightly overestimate the uncertainty. For a proper treatment, the transverse momenta of the jets themselves should be recalculated with the JES shifted by $\pm 1\sigma$. However, this uncertainty is small when compared to the theoretical uncertainty, therefore any overestimation in uncertainty is not significant.

Table 5.11 shows the results of these measurements, along with the statistical uncertainty on ϵ_Z^{data} and the theoretical and experimental uncertainties on $\frac{\epsilon_{WW}^{MC}}{\epsilon_Z^{MC}}$. The calculated ratio of the jet veto efficiency in WW data and MC is applied as a correction to the WW acceptance prediction. This ratio is determined to be $\frac{\epsilon_{WW}^{data}}{\epsilon_{WW}^{MC}} = 0.966 \pm 0.013$(stat) ± 0.011(syst) ± 0.058 (theory) $= 0.966 \pm 0.060$(stat+syst+theory).

	Value	Stat. error	Syst. error	Theory error	Combined error
ϵ_Z^{data}	0.732	0.007	-	-	0.007
ϵ_Z^{MC}	0.759	0.0006	-	-	0.0006
ϵ_{WW}^{MC}	0.633	0.002	-	-	0.002
$\epsilon_{WW}^{MC}/\epsilon_Z^{MC}$	0.834	0.002	0.007	0.050	0.051
ϵ_{WW}^{data}	0.612	0.008	0.007	0.037	0.038

Table 5.11: The jet veto efficiency for Z data and Z and WW MC with errors. These quantities are used to calculate the expected jet veto efficiency in WW data used in the SM WW cross section measurement, which is also shown in the table.

The jet veto efficiency correction factor is only applicable to events produced with MC@NLO, namely the WW and WZ samples, therefore it is only applied to these samples whereas the lepton efficiency scale factors are applied to all MC events.

5.5 Corrections for the $H \to WW$ search

The same methods as those used for the WW cross section measurement are used to determine correction factors for the $H \to WW$ search to account for any differences between data and MC.

Identical triggers are used for both the WW measurement and the $H \to WW$ search, although the subleading lepton p_T cut is lowered from 20 GeV to 15 GeV for the Higgs boson search. The effect of this on the trigger efficiency was studied and found to have a negligible effect. Therefore, the trigger scale factors calculated for the WW analysis and shown in Table 5.6 are also used for the $H \to WW$ search,

The lepton scale factors are determined separately for the Higgs boson search since the isolation requirements are slightly different from those used in the WW analysis. These scale factors are calculated for the additional selection requirements, namely the isolation, impact parameter and track origin on the z-axis, which are applied on top of the standard tight electron identification requirements. Tag and probe methods are used to calculate the scale factors and are discussed in the context of the $H \to WW$ search in [87] and described briefly in Section 5.5.1.

The jet veto efficiency scale factor is not calculated for the $H \to WW$ search at this stage. However, in the future, it would be desirable to calculate a scale factor as in the WW case to account for differences in the jet multiplicity distributions in data and MC.

5.5.1 Lepton efficiency scale factor calculation

For electrons, an η and E_T dependent scale factor is used. This is particularly important for the Higgs boson search since the subleading lepton E_T cut is at 15 GeV and the scale factor is significantly smaller in the low-E_T region than it is in the high-E_T region. The method used to calculate the efficiency in data and MC, as well as the scale factor, is described in [88] and the results are shown in Tables 5.12 and 5.13 as a function of η and E_T respectively for the electron efficiencies and scale factors corresponding to the isolation, impact parameter and track origin on the z-axis selections applied to electrons which have already passed tight identification criteria. This differs from Tables 5.7 and 5.8, which show the efficiencies and scale factors for isolation, impact parameter, track origin and tight identification selection criteria applied to electrons which have been reconstructed but have passed no other identification requirements.

η bin	$[-2.47, -2.01]$	$[-2.01, -1.52]$	$[-1.37, -0.8]$	$[-0.8, 0.]$
Data (%)	94.1 ± 1.1	91.6 ± 1.0	93.7 ± 0.7	95.6 ± 0.4
MC (%)	95.1 ± 0.6	93.5 ± 0.6	95.5 ± 0.4	96.6 ± 0.2
$\frac{Data}{MC}$(%)	98.9 ± 1.3	98.0 ± 1.3	98.2 ± 0.8	99.0 ± 0.5
η bin	$[0., 0.8]$	$[0.8, 1.37]$	$[1.52, 2.01]$	$[2.01, 2.47]$
Data (%)	95.3 ± 0.4	94.3 ± 0.6	92.9 ± 0.9	94.9 ± 1.0
MC (%)	96.6 ± 0.2	95.1 ± 0.4	92.9 ± 0.6	94.7 ± 0.7
$\frac{Data}{MC}$(%)	98.7 ± 0.5	99.1 ± 0.8	100.0 ± 1.2	100.2 ± 1.3

Table 5.12: Electron identification efficiencies and $\frac{Data}{MC}$ scale factors as a function of η corresponding to the isolation, impact parameter and track origin on the z-axis selections applied to electrons which have already passed tight identification criteria. Errors shown are statistical only.

Muon efficiencies are measured using the tag and probe method on $Z \to \mu\mu$ events as described in [89]. The scale factor used to correct MC events to data is measured to be 0.9813 ± 0.0037.

$E_T(GeV)$ bin	$[15, 20]$	$[20, 25]$	$[25, 30]$	$[30, 35]$	$[35, 40]$	> 40
$\frac{Data}{MC}(\%)$	80.8 ± 12.8	86.5 ± 9.2	92.9 ± 5.8	96.9 ± 5.5	97.8 ± 5.5	98.4 ± 5.5

Table 5.13: Electron identification efficiencies and $\frac{Data}{MC}$ scale factors as a function of E_T corresponding to the isolation, impact parameter and track origin on the z-axis selections applied to electrons which have already passed tight identification criteria. Errors shown are statistical only.

5.6 Summary

The correction factors described in this chapter are applied to MC as follows. Each event is multiplied by a weight, w, given by:

$$w = SF_{PV} \times SF_{trig} \times SF_{\ell_1} \times SF_{\ell_2} \times SF_{JV} \tag{5.7}$$

where SF_{PV} is the primary vertex weight, SF_{trig} is the event-based trigger scale factor, SF_{ℓ_i} is the scale factor for lepton i and SF_{JV} is the jet veto scale factor, which is only applied in the SM WW cross section measurement.

The primary vertex correction is calculated and applied exactly the same way for the SM WW and $H \rightarrow WW$ analyses, as described in Section 5.1, as is the trigger scale factor, which is calculated in Section 5.2.

The lepton scale factors are determined separately for electrons and muons. η-dependent electron scale factors, as given in Tables 5.7 and 5.8, are applied in the SM WW case. These scale factors have an additional E_T-dependent uncertainty, given in Table 5.9. For the Higgs boson search, η and E_T-dependent scale factors are applied, as given by Tables 5.12 and 5.13. For muons, a constant scale factor is applied for both the SM WW and $H \rightarrow WW$ cases. This is determined in Section 5.3.2 for the SM WW measurement and Section 5.5.1 for the Higgs boson analysis.

The jet veto scale factor is only used during the measurement of the SM WW cross section. This is calculated in Section 5.4.

Chapter 6

Backgrounds to WW and $H \rightarrow WW$ production

There are many physics processes which may mimic WW and $H \rightarrow WW$ production. Backgrounds may be taken from MC however the MC may not accurately describe the production of these processes. This could be due to a number of reasons. For example, events containing jets may suffer from theoretical uncertainties due to the hadronisation model, choice of PDFs and many other theoretical effects. This could lead to a difference in the rate at which jets are falsely identified by the detector as leptons in MC and data.

There may be also be mismodelling of the detector response which could affect the modelling of any background process. For example, mismodelling of missing E_T could lead to more events arising from Z+jets processes, with no real source of missing E_T, falling into the signal region in data than in MC if the missing E_T resolution is worse in data than in MC. If this occurs, the modelling of other backgrounds with no real missing E_T, such as QCD, is also affected.

In addition, processes which have a large cross section but a small probability of passing WW or Higgs boson selection critieria may suffer from a significant amount of statistical fluctuation in the MC samples. This follows from the relationship between the number of events, cross section and integrated luminosity:

$$\mathcal{L} = \frac{N}{\sigma} \tag{6.1}$$

For a given luminosity, $\mathcal{L}$, it is necessary to produce an increasingly large number of MC events, N, with increasing cross section σ. If the MC sample is smaller than the number of data events for the integrated luminosity of the data sample, each event gains a scale factor of more than one when it is scaled to the luminosity of the data. This means that even if there is just one MC event left after full event selection, this event will receive a large scale factor and may contribute significantly to the expected background. Of course, this one event may well be just a statistical fluctuation which, in data, occurs much less often than the MC prediction. There is also the chance that rare background events may be completely missed in the MC sample, leading to an underestimate of that background. To avoid this, backgrounds with large cross sections, such as QCD or W+jets, should be measured using data instead of MC.

The methods used to measure backgrounds using data are described in the following sections. Unless otherwise stated, the results presented are for the backgrounds to the

VBF $H \to WW$ search which has at least two jets in the final state. The methods described are applicable to all of the search channels described in this thesis and the methods used to estimate the backgrounds to the WW cross section measurement are explicitly detailed in Section 6.6.

6.1 Z background

The contribution of the Z background to WW and $H \to WW$ production arises when the missing E_T in Z events is mismeasured, giving a signature of two oppositely charged leptons plus significant missing E_T consistent with that of the decay of W-pairs. This background is estimated for the ee and $\mu\mu$ channels by calculating a factor to account for this missing E_T mismeasurement. Z events in data and MC are selected by requiring two opposite sign leptons lying within the Z peak region of $|m_Z - M_{ll}| < 10$ GeV. These samples are then divided into four control regions in the plane of missing E_T versus M_{ll} as shown in Figure 6.1.

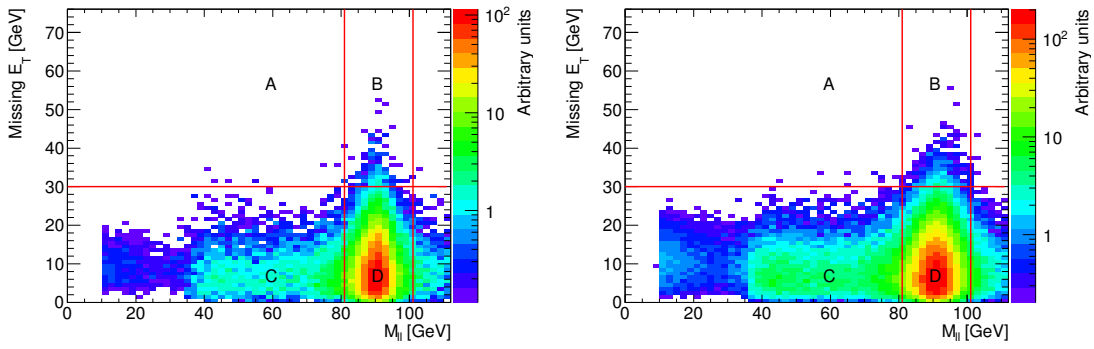

Figure 6.1: Missing E_T distribution versus M_{ll} for $Z \to ee$ (a) and $Z \to \mu\mu$ (b) events in MC with regions A, B, C and D, used in the estimation of the Z background, illustrated.

Region A is the signal region, with M_{ll} below the Z peak and missing $E_T > 30$ GeV. This method aims to calculate a correction factor to account for missing E_T mismodelling which can be applied to the expected number of events from MC in region A to reach a more accurate estimate of the number of Z background events lying in the signal region.

Control regions B and D occupying the Z peak region with $|m_Z - M_{ll}| < 10$ GeV, are compared in data and Z MC to estimate the correction factor. In data, this region is completely Z-dominated, with contributions from other backgrounds being negligible. Regions B and D correspond to events with high and low missing E_T respectively. The ratio between the number of events lying in regions B and D depends on the modelling of the missing E_T tails, which arise from mismeasurements since there is no real source of missing E_T in Z events. If there is any difference in the modelling of these tails in data and MC, this ratio will be different. For example, if this ratio is higher in data than MC, this implies that there are more events lying in this high missing E_T region in data than the MC expectation. The ratio is expected to be independent of M_{ll} and a higher ratio

in data would suggest that there are more Z events in the high missing E_T signal region in data than in MC.

This method can be summarised by the following equation:

$$\begin{aligned} A_{MC}^{Corrected} &= A_{MC} \times \frac{B_{Data}}{D_{Data}} \frac{D_{MC}}{B_{MC}} \\ &= A_{MC} \times F \end{aligned} \tag{6.2}$$

where F is the correction factor.

It would also be possible to directly estimate the number of Z events in the signal region using:

$$A_{Data}^{Estimated} = C_{Data} \times \frac{B_{Data}}{D_{Data}} \tag{6.3}$$

however this would require the contribution from other background processes in control region C to be explicitly subtracted from the number of data events to estimate the number of Z events in region C. To avoid this complication, the simpler data/MC correction factor is calculated instead.

Since the number of events lying in the high missing E_T region is expected to be small due to the lack of any real source of true missing E_T in Z events, the ratio between events lying in regions B and D for data and MC is plotted as a function of missing E_T cut. These ratios are defined as:

$$R_{MC}(x) = \frac{B_{MC}}{D_{MC}}(x) \tag{6.4}$$

$$R_{Data}(x) = \frac{B_{Data}}{D_{Data}}(x) \tag{6.5}$$

where x is the value of the missing E_T cut. A fit is performed to the plot of these ratios evaluated at varying values of missing E_T cut and the value of the fit with the missing E_T cut equal to 30 GeV is taken to be the ratio. These ratios, along with the fitted exponentials, are shown in Figure 6.2. This figure shows that the statistical error increases with increasing missing E_T cut as expected.

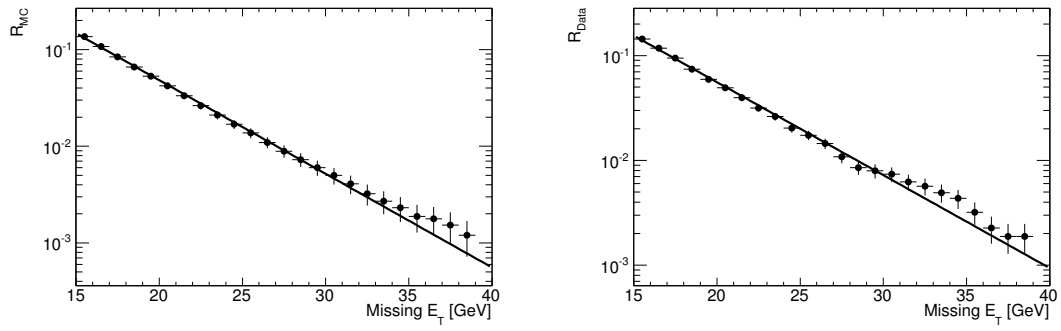

(a) (b)

Figure 6.2: The ratio of events lying in high and low missing E_T regions, described by equations 6.4 (a) and 6.5 (b), for $Z \to ee$ MC and data respectively.

At a missing E_T cut of 30 GeV, the correction factors for the ee and $\mu\mu$ channels are calculated to be 1.36 and 1.24 respectively. This indicates that the missing E_T resolution

is worse in data than in MC and the MC is likely to underestimate the Z background in the signal region. The Z background estimates using these correction factors are shown in Tables 6.1 and 6.2 for the ee and $\mu\mu$ channels respectively.

Selection	A (MC)	A (Estimated)
Opposite charge	6.26	8.48
$M_{\ell\ell} > 15$ GeV	6.03	8.17
Z veto	6.03	8.17
Missing E_T	6.03	8.17
≥ 2 jets	2.58	3.50
$\eta_{j_1} * \eta_{j_2} < 0$	1.15	1.56
$\Delta\eta_{jj} > 3.8$ rad	0.02	0.02
$M_{jj} > 500$ GeV	0.01	0.01
Extra jet veto	0	0
b-jet veto	0	0
$p_T^{Tot} < 30$ GeV	0	0
$Z \to \tau\tau$ veto	0	0
$M_{\ell\ell} < 65$ GeV	0	0
$\Delta\phi_{ll} < 1.8$ rad	0	0
$0.75 \times m_H < M_T < m_H$	0	0

Table 6.1: Number of Z+jets events expected in the ee+2 jets channel estimated directly from MC and estimated with the data-driven method.

Selection	A (MC)	A (Estimated)
Opposite sign	22.43	27.92
$M_{\ell\ell} > 15$ GeV	21.31	26.52
Z veto	21.31	26.52
Missing E_T	21.31	26.52
≥ 2 jets	8.54	10.63
$\eta_{j_1} * \eta_{j_2} < 0$	3.66	4.56
$\Delta\eta_{jj} > 3.8$ rad	0.42	0.53
$M_{jj} > 500$ GeV	0.13	0.17
Extra jet veto	0.12	0.15
b-jet veto	0.12	0.15
$p_T^{Tot} < 30$ GeV	0.11	0.14
$Z \to \tau\tau$ veto	0.11	0.14
$M_{\ell\ell} < 65$ GeV	0	0
$\Delta\phi_{ll} < 1.8$ rad	0	0
$0.75 \times m_H < M_T < m_H$	0	0

Table 6.2: Number of Z+jets events expected in the $\mu\mu$+2 jets channel estimated directly from MC and estimated with the data-driven method.

These tables show that after the full $H+2j$ event selection is applied, no events remain in the signal region in Z MC. This means that at this stage, this method of estimating the

Z background estimation breaks down. However, with larger MC samples, it is possible that some Z events may remain at the end of the cutflow, in which case it would be possible to use this method. It would also be possible to use the method described by Equation 6.3 in the future.

Regardless of these issues with estimating the final contribution of Z after all cuts, this method still indicates that while the data and MC agreement is not perfect for the missing E_T resolution, there is not a dramatic discrepancy. For the final results, MC is used to estimate the Z background and the data-driven results just provide a cross-check.

6.2 Top background

In the $H+2j$ analysis, the top background can be estimated by defining a control sample which is enriched in top events. The control region is constructed by reversing the b-jet veto and removing all other cuts after the requirement of at least 2 jets. The distribution of the number of b-jets is shown in Figure 6.3. This figure indicates that requiring at least one b-jet selects a sample which is completely dominated by top events, with contributions from other backgrounds totalling much less than one event.

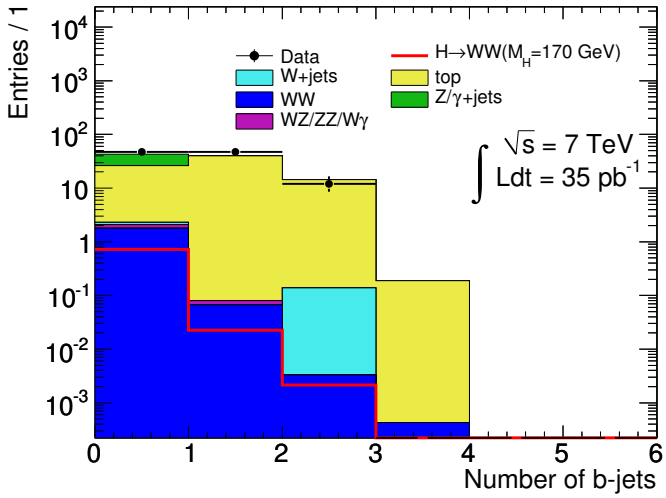

Figure 6.3: The number of b-jets for ee, $\mu\mu$ and $e\mu$ channels combined after requiring at least 2 jets.

Using this control region, the number of top events in the signal region may be estimated in the two jet channel using:

$$\begin{aligned} N_{SR}^{Data} &= \frac{N_{SR}^{MC}}{N_{CR}^{MC}} \times N_{CR}^{Data} \\ N_{SR}^{Data} &= \alpha_{top}^{2j} \times N_{CR}^{Data} \end{aligned} \tag{6.6}$$

where N_{SR} gives the number of top events in the signal region, defined as events with no b-jets, and N_{CR} is the number of top events in the control region, defined as events with one or more b-jets. This equation also provides the definition of α_{top}^{2j}, which describes the ratio of events in the signal and control regions in MC,

Lepton Flavors	Signal	Top	WW	$WZ/ZZ/W\gamma$	Z+jets	W+jets	Total Bkg.	Observed
Two jets, opposite hemispheres								
$e\mu$	0.01 ± 0.01	27.7	0.04	0.00	0.00	0.14	27.9 ± 0.89	30
ee	0.00	8.49	0.01	0.00	0.11	0.00	8.62 ± 0.49	14
$\mu\mu$	0.01 ± 0.01	18.0	0.03	0.01	0.41	0.00	18.5 ± 0.75	15
$\Delta\eta_{\rm jj} > 3.8$								
$e\mu$	0.01 ± 0.01	12.8	0.02	0.00	0.00	0.00	12.8 ± 0.59	12
ee	0.00	4.00	0.01	0.00	0.01	0.00	4.01 ± 0.33	8
$\mu\mu$	0.01 ± 0.01	8.00	0.01	0.00	0.28	0.00	8.30 ± 0.51	6
$m_{\rm jj} > 500$ GeV								
$e\mu$	0.00	0.56	0.00	0.00	0.00	0.00	0.56 ± 0.12	1
ee	0.00	0.30	0.00	0.00	0.00	0.00	0.31 ± 0.09	0
$\mu\mu$	0.00	0.62	0.00	0.00	0.00	0.00	0.62 ± 0.12	0
Central jet veto								
$e\mu$	0.00	0.09	0.00	0.00	0.00	0.00	0.09 ± 0.04	0
ee	0.00	0.00	0.00	0.00	0.00	0.00	0.00	0
$\mu\mu$	0.00	0.10	0.00	0.00	0.00	0.00	0.10 ± 0.05	0

Table 6.3: The expected number of events in the top control region for the $H + 2j$ analysis after various cuts for 35 pb^{-1} of integrated luminosity. The rightmost two columns show the total number of expected background and observed events. The signal numbers correspond to the case of $m_H = 170$ GeV. Errors are statistical only.

Since the jet veto and the cuts on $\Delta\eta_{\rm jj}$ and $m_{\rm jj}$ also significantly reject the top background, it is informative to study the effect of successive application of these cuts. Table 6.3 shows the expected number of events in 35 pb^{-1} of integrated luminosity for signal and background in this control region after the application of the cuts on $\Delta\eta_{\rm jj}$, $m_{\rm jj}$, and the central jet veto. A comparison with the observed number of events in data in the control region is also provided. This table demonstrates that the control region definition used produces a very pure top control sample. In the currently available dataset, statistical errors are quite large, and so the loosest set of cuts should be used to normalise the top background meaning that α_{top}^{2j} (which is taken entirely from MC) should be calculated after the requirement of two jets lying in opposite hemispheres.

The ratio of top cross sections in the signal region and the control region is denoted as α_{top}^{2j}, and its central value is taken from MC. Systematic errors on this quantity arise from three main sources:

- The Q^2 scale choice in the top MC may be varied to estimate the theoretical uncertainty. For the loosest control sample selection (no central jet veto and no forward jet tagging cuts), the theoretical uncertainty on α_{top}^{2j} is 38% [90]. α_{top}^{2j} is determined after the selection of events containing two jets lying in opposite hemispheres to reduce the statistical uncertainty. However, this increases the systematic uncertainty due to the Q^2 scale. This uncertainty may be reduced in the future, when more data is available and statistical errors are not so large, by calculating α_{top}^{2j} after the $m_{\rm jj}$ cut instead.

- There is an uncertainty on the JES which contributes 8% to the uncertainty on α_{top}^{2j}.

- There is also a 12% uncertainty on the b-tagging efficiency which contributes 20%

to the uncertainty on α_{top}^{2j}.

In order to estimate the number of top events in the signal region, the number of data events lying in the top-dominated control region is multiplied by α_{top}^{2j}. However, with the dataset available at present, there are no events lying in the control region after all cuts have been applied. Therefore currently the top background is estimated using MC only.

Looking at the number of top background events estimated in data and expected from MC, good agreement is seen in the $\mu\mu$ and $e\mu$ channels. There is a reasonably large discrepancy in the ee channel, with the MC appearing to quite significantly underestimate the number of top events observed in data. Since the absolute number of top events expected after all cuts is very small in the two jet channel with the dataset used here, this is not a significant effect at present. However, this should be closely monitored in the future as the dataset increases further.

6.3 W+jets background

The W+jets background to WW and $H \to WW$ occurs when the W boson decays leptonically and one of the jets is falsely identified as a lepton giving a signature of two leptons with missing E_T from the neutrino produced during the W decay. The rate at which jets are misidentified as leptons is expected to be small however this effect may not be well-modelled in MC therefore it is desirable to estimate this background directly from data.

A well-established procedure for estimating the W+jets background to WW and $H \to WW$ processes has been defined and is described in Refs. [90, 91]. This method selects a W+jets control sample by requiring events to contain one lepton passing the identification criteria described in Section 5.3, known as the identified lepton, and one lepton which must pass a very loose set of cuts, known as the fakeable lepton. The number of W+jets events falling in the signal region is calculated to be the number of events with one identified lepton and one fakeable lepton multiplied by the fake factor, f_l, which is defined as the probability for a fakeable lepton to additionally pass the full lepton selection.

f_l may be determined by collecting a control sample which is required to pass a jet trigger with a p_T threshold of 15 GeV. This sample is expected to be enriched in jets and provides a large sample from which to extract f_l. Within this control sample, events containing a fakeable lepton are selected and the fraction of these fakeable leptons which also pass full lepton identification criteria is calculated. This is then applied to the W+jets control sample to estimate the number of W+jets events lying in the signal region. W and Z events are explicitly removed when determining f_l by rejecting any events with $m_T > 30$ GeV as well as any events with two opposite sign leptons with $|m_Z - M_{ll}| < 15$ GeV.

This method is used to estimate the W+jets background for the WW cross section measurement as well as the zero and one jet channels in the $H \to WW$ search. The W+jets background to the $H + 2j$ channel is taken from MC since it is expected to be small. In the future, however, this background should be determined in this way for the $H + 2j$ channel as well.

6.4 WW background to $H \rightarrow WW$

SM WW production is expected to be the dominant background to $H \rightarrow WW$. The two processes may be distinguished by utilising the spin-0 nature of the Higgs boson, which causes differences in the M_{ll} and $\Delta\phi_{ll}$ distributions. The m_T distribution may also be used to separate $H \rightarrow WW$ and SM WW production. Therefore, a WW control region may be constructed by applying the same cuts as are used to select the Higgs boson signal with the following exceptions:

- M_{ll} is required to be larger than 80 GeV. Events with same flavour dileptons must lie outside the Z peak region, with $|m_Z - M_{ll}| > 10$ GeV.
- The cuts on $\Delta\phi_{ll}$ and m_T are removed.

These cuts select a control region which is dominated by WW events however some contamination remains from top and Z+jets events. These are subtracted using MC. From this, α_{WW}, defined as the ratio between the number of events lying in the Higgs boson signal region and the number of events in the WW control region may be calculated from MC. Then, the estimated number of WW events lying in the Higgs boson signal region is given by α_{WW} multiplied by the number of data events in the WW control region.

The WW background is determined using this method in the $H + 0j$ and $H + 1j$ channels. As is the case for the W+jets background, it would also be desirable to use this method in the $H + 2j$ channel in the future.

6.5 Additional sources of background

The dominant sources of background in addition to those already considered arise from WZ, ZZ and $W\gamma$ processes. At present, these are determined using MC since they are expected to be small with respect to the other backgrounds. With the dataset increasing rapidly in 2011, it would be desirable to measure these backgrounds in a data-driven way to act as a cross-check to the MC prediction at least.

6.6 Determination of backgrounds to SM WW production

The same sources of background which may be falsely identified as $H \rightarrow WW$ events also serve as backgrounds to SM WW production. For the WW cross section measurement, the W+jets background was measured in exactly the same way as that used for the $H \rightarrow WW$ search. All other backgrounds were taken from MC, with the systematic error on the Z+jets background calculated using a partially data-driven method, described in detail in [83].

6.7 Summary

To summarise, most of the backgrounds to $H \to WW$ and SM WW production may be measured in a data-driven way, reducing the reliance on MC, as described in this chapter. However, due to the small amount of data collected, resulting in low statistics in the control regions, most backgrounds were taken from MC for the final results, with the data-driven methods used as a cross-check. For the SM WW cross section measurement, the W+jets background was determined in the data-driven way described in Section 6.3 and all other backgrounds were taken from MC. Similarly, this same method of estimating the W+jets background was used in the $H + 0j$ and $H + 1j$ channels in the cut-based analysis, with all the other backgrounds estimated using MC. For the $H + 2j$ (cut-based) and the matrix-element-based Higgs boson search, all backgrounds were taken from MC.

The number of background events after selections for the SM WW cross section measurement is shown in Table 8.3. This is shown for the H+$0j$, H+$1j$ and H+$2j$ (cut-based) channels in Tables 9.3, 9.4 and 9.5 respectively. Similarly, the number of background events for the matrix-element-based Higgs boson search are given in Tables 10.1, 10.2 and 10.3 for the ee, $\mu\mu$ and $e\mu$ channels respectively.

Chapter 7

The matrix element discriminant

7.1 The matrix element discriminant

A matrix element discriminant provides a way to exploit the slight differences in final state event kinematics between signal and backgrounds which may be too subtle to allow much discrimination in a straightforward cut-based analysis. It has been used successfully by the CDF collaboration in their searches for Higgs bosons decaying to W pairs [92, 93] both on its own and as an input to a neural network and has been studied previously at ATLAS using MC [94].

The probability that an event is of a certain type relies directly on the matrix element for that process and can be calculated exactly at generator level provided that the full event kinematics are known. At the reconstructed level, it can also be calculated provided that any unknowns in the system, such as the neutrino kinematics, are correctly integrated over and detector resolution effects are properly accounted for. The details of the event probability calculation are shown in Section 7.2.

A matrix element discriminant may be constructed from the event probability for each event, defined as:

$$LH(M_H) = \frac{P_H(M_H)}{P_H(M_H) + \sum_n \beta_n P_n} \tag{7.1}$$

where P_α = event probability for event type α. The sum term runs over all the possible backgrounds, with β giving the relative contribution of each background channel to the total background. In theory, this should include all the backgrounds listed in Section 6 but in fact it is only necessary to include the major backgrounds since for minor backgrounds β will be small. In this analysis, only the main background of continuum WW production is investigated and the discriminant reduces to:

$$LH(M_H) = \frac{P_H(M_H)}{P_H(M_H) + P_{WW}} \tag{7.2}$$

This discriminant will henceforth be referred to as the matrix element likelihood ratio.

Cutting directly on the matrix element likelihood as part of a simple cut-based analysis should allow other selection criteria to be relaxed so that more signal events remain for the same amount of background. The likelihood distribution may also be used directly as an input to the limit-setting procedure to exploit differences in shape between the signal and background processes.

It is important to note that the Higgs boson event probability, and hence the matrix element likelihood, relies directly on the hypothesized Higgs boson mass meaning that the likelihood must be re-calculated at each mass point.

7.2 Event probability calculation at truth level

The event probability, P_α, is given by:

$$P_\alpha = \frac{1}{\sigma}\sum_{i,j}\int T(z,y)\frac{d\sigma_{ij}}{dy}dy \tag{7.3}$$

where σ is the cross section for the process α, the sum runs over the possible combinations of initial state partons i, j, $\frac{d\sigma_{ij}}{dy}$ is the parton-level differential cross section and $T(z,y)$ is the transfer function relating measured quantities with parton-level quantities. z is the four-vector of the reconstructed final state and y is the four-vector of the true final state at generator level. The transfer function accounts for the intrinsic resolution of the detector, which is not perfect; in an ideal detector, the transfer function would just be a delta function since the measured quantities would be exactly equal to the parton-level quantities. In this thesis, the transfer function $T(z,y)$ represents a smearing of event kinematics according to the detector resolution.

This event probability should be interpreted as the probability that an event with given kinematics is consistent with process α. Higgs boson events will tend to have kinematics which are more consistent with Higgs boson production than continuum WW production so the Higgs event probability will be larger than the WW event probability for these events.

Since the colliding partons only carry a fraction of the colliding protons' momentum, where $x_{1,2}$ give the momentum fractions carried by partons 1 and 2, this must be accounted for in the event probability calculation. This is done by convolving the cross section $d\sigma_{ij}$ with the PDFs for partons 1 and 2 to give:

$$P_\alpha = \frac{1}{\sigma}\sum_{i,j}\int f_i(x_1,Q^2)f_j(x_2,Q^2)T(z,y)dx_1dx_2\frac{d\sigma_{ij}}{dy}dy \tag{7.4}$$

where $f_x(x_n,Q^2)$ are the PDFs for parton n.

The differential cross section for two-body production of an N-body final state from two incoming particles is given by [1]:

$$d\sigma_{ij} = \frac{|\mathcal{M}_{ij}(\alpha)|^2}{4\sqrt{(q_1.q_2)^2 - m_{q_1}^2 m_{q_2}^2}} \times d\Phi_N(q_1+q_2;p_1,...,p_N) \tag{7.5}$$

where α is the process type, $\mathcal{M}_{ij}(\alpha)$ is the matrix element for partons in initial states i and j, $d\Phi_N$ represents the differential over N-body phase space, q_1 and q_2 are the four momenta of the incoming partons, which have masses m_{q_1} and m_{q_2}, and $p_1,...,p_N$ are the four momenta of the outgoing partons.

Representing four momentum as $q = (p_x, p_y, p_z, E)$, q_1 and q_2 may be written as:

$$\begin{aligned} q_1 &= (0,0,x_1E_{beam},x_1E_{beam}) \\ q_2 &= (0,0,-x_2E_{beam},x_2E_{beam}) \end{aligned} \tag{7.6}$$

Under the assumption that the partons are massless, the flux term may be written:

$$F = \frac{1}{4\sqrt{(q_1.q_2)^2 - m_{q_1}^2 m_{q_2}^2}} = \frac{1}{8x_1x_2E_{beam}^2} \tag{7.7}$$

where E_{beam} is the beam energy, which is equal to 3.5 TeV for the dataset used here.

The $d\Phi_N$ term, which represents the Lorentz invariant differential over N-body phase space, is defined as:

$$d\Phi_N(q_1 + q_2; p_1, ..., p_N) = (2\pi)^4\delta^4(q_1 + q_2 - \sum_{i=1}^{N} p_i)\prod_{i=1}^{N}\frac{d^3p_i}{(2\pi)^3 2E_i} \tag{7.8}$$

where q_1 and q_2 are the four momenta of the initial state partons and E_i and p_i are the energy and momentum of the ith final state particle produced in the decay.

Using Equation 7.8, the event probability for process α may be written:

$$\begin{aligned} P_\alpha \;=\; & \tfrac{1}{\sigma}\textstyle\sum_{i,j}\int \frac{f_i(x_1,Q^2)f_j(x_2,Q^2)|\mathcal{M}_{ij}(\alpha)|^2 T(z,y)dx_1dx_2}{8x_1x_2E_{beam}^2} \\ & \times(2\pi)^4\textstyle\prod\frac{d^3p_i}{(2\pi)^3 2E_i} \\ & \times\delta^3(L_{l_1} - p_{l_1})\delta^3(L_{l_2} - p_{l_2})\delta(k_x - \textstyle\sum p_{x_i})\delta(k_y - \textstyle\sum p_{y_i})d^3L_{l_1}d^3L_{l_2}dk_xdk_y \end{aligned} \tag{7.9}$$

where σ is the total cross section for production of particle α, $f_x(x_n, Q^2)$ are the PDFs for parton n with momentum fraction x_n, $\mathcal{M}_{ij}(\alpha)$ is the matrix element for partons in initial states i and j, q_1 and q_2 are the four momenta of the initial state partons and E_i and p_i are the energy and momentum of the ith final state particle produced in the decay. L_{l_i} is the true four vector for lepton i, with p_{l_i} representing the measured four vector. k_x and k_y are the true x and y components of momentum of the whole system.

A routine to calculate the matrix element is taken from the event generator MadGraph [71], with each different process using a different matrix element function. Since the initial state parton flavours are not known, a sum over all possible subprocesses is performed, with each subprocess corresponding to a different initial state parton configuration.

The event probability may be calculated without performing the integration over phase space if the full truth information for each event is known since the integration reduces to a delta function at the true value of the event kinematics. In this case, the event probabilty formula may be simplified to become:

$$P_\alpha = \frac{1}{\sigma}\sum_{i,j}|\mathcal{M}_{ij}(\alpha)|^2 f_i(x_1, Q^2)f_j(x_2, Q^2) \tag{7.10}$$

where constants have been dropped since they do not affect the calculated matrix element likelihood ratio.

The LHAPDF [95] interface is used to access the PDFs used in the event probability calculation. In this case, CTEQ6.1 [96, 97] is used. A likelihood ratio, defined as in Equation 7.1, constructed of the true event probabilities is shown in Figure 7.1 for a Higgs boson sample with $m_H = 160$ GeV and a WW background sample. The samples were generated first using MadGraph, the event generator used for the matrix element

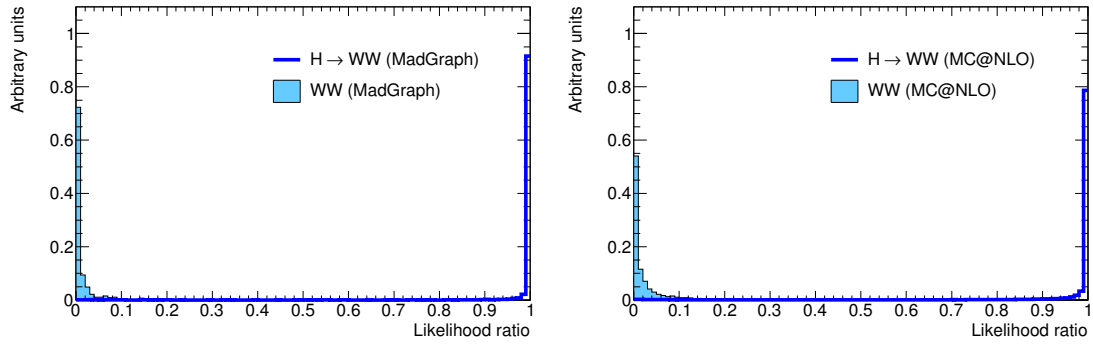

(a) (b)

Figure 7.1: True likelihood ratios for Higgs boson signal and WW background events produced with MadGraph (a) and MC@NLO (b). The Higgs boson signal events are produced with $m_H = 160$ GeV.

calculation, and secondly with MC@NLO, the event generator used to evaluate the backgrounds for the SM WW cross section measurement and the cut-based $H \rightarrow WW$ search described in Chapters 8 and 9.

Clear separation between the signal and background is seen in all cases, with similar performance observed using the MadGraph and MC@NLO samples. This is an important result: MadGraph is a LO generator so does not model any higher order effects which may be present in data. MC@NLO is NLO so models next-to-leading order effects. Since the performance of the likelihood is comparable using MadGraph and MC@NLO, this suggests that these higher order effects do not affect the matrix element calculation significantly. This suggests that the use of a LO matrix element calculation is appropriate in this case.

In addition to looking qualitatively at the likelihood ratios for signal and background, it is also instructive to investigate cases where true Higgs boson events are falsely classified as WW events, with a likelihood ratio close to zero. For a test sample of 10,000 Higgs boson events generated using MadGraph, only 70 events have a likelihood ratio of less than 0.05 so this is clearly a small effect. Investigating the distributions of the topological variables which are used in the cut-based analysis to separate the Higgs boson signal from the SM WW background shows that Higgs boson events with low likelihoods tend to have distributions similar to those observed in WW events, as can be seen in Figure 7.2. This indicates that the matrix element likelihood is classifying events correctly, with Higgs boson events which happen to fall in WW-dominated regions of phase space having a low likelihood ratio. As expected, this is a small number of events since over 99% of Higgs boson events have a high likelihood ratio and are correctly identified as being Higgs-like.

7.3 Event probability calculation at reconstructed level

The approach discussed in the previous section is unfortunately an unrealistic approach since with data the full event kinematics will not be known due to the undetected neutrinos. The method which must be performed with real data involves Monte Carlo integration over the unknown components of neutrino momentum in the integral given by

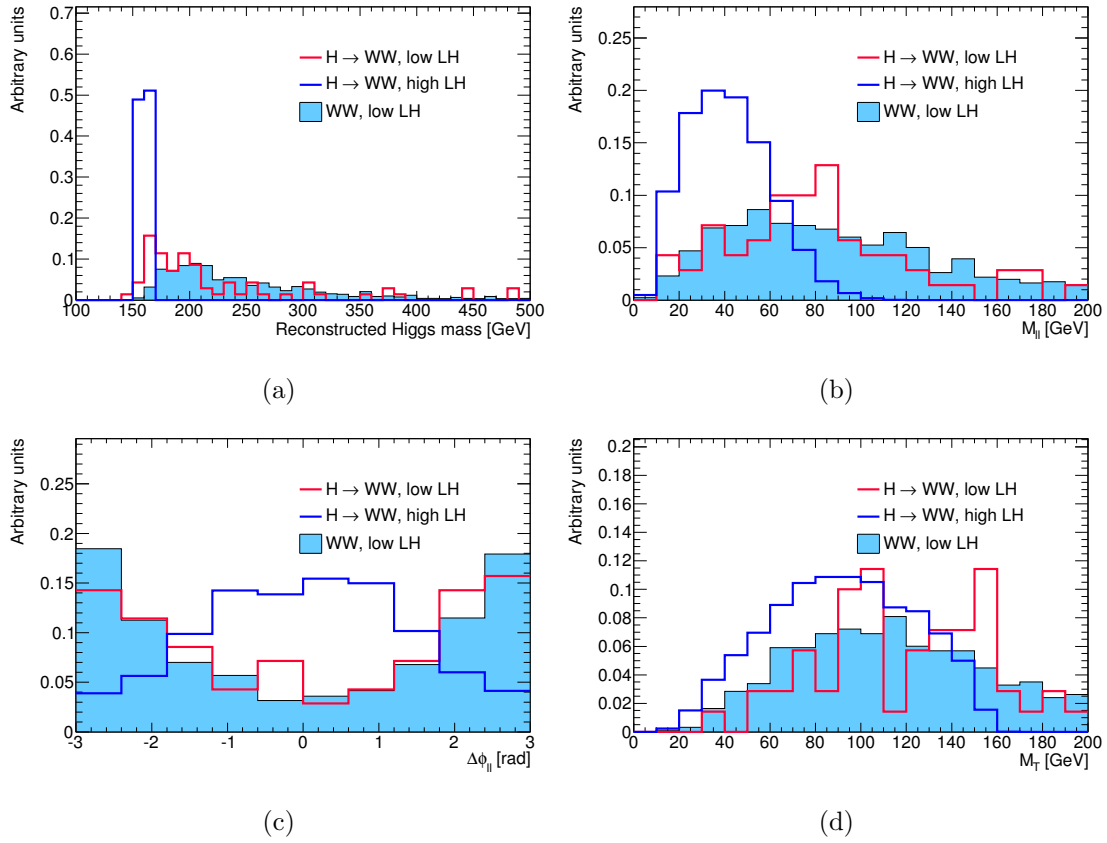

Figure 7.2: Reconstructed m_H (a), M_{ll} (b), $\Delta\phi_{ll}$ (c) and m_T (d) for Higgs boson events with low and high likelihood ratios and SM WW events. All events are generated by MadGraph and the Higgs boson signal events have $m_H = 160$ GeV. The variables are shown at truth level only.

Equation 7.9, This involves the evaluation of the integral at a large number of randomly chosen phase space points. The Higgs boson has a very narrow width so occupies only a very small region of phase space. Conversely, the neutrino momentum distributions cover a very wide region of phase space so very few of the randomly chosen values of neutrino momentum are likely to give solutions which are consistent with a Higgs boson event. If no solutions are found for a given iteration, the iteration does not contribute to the event probability hence, if many of the iterations have no solutions, a much larger number of iterations will be necessary for the integration to converge and give a valid solution with a small uncertainty. Therefore, it is practical to choose integration variables which are more peaked in phase space such as the Higgs boson mass or the W mass to increase the number of iterations which have solutions, allowing the total number of iterations to be reduced, saving CPU time.

7.3.1 Higgs boson event probability

It is important to remember that in order to calculate the Higgs boson event probability, the matrix element function requires the Higgs boson mass to be specified. Therefore instead of obtaining one likelihood for each event, a number of likelihoods are obtained

with each one corresponding to the hypothesized Higgs boson mass. For Higgs boson masses with $m_H > 2m_W$, the W bosons produced during the Higgs boson decay are likely to be on mass shell with masses close to the centre of a Breit-Wigner distribution. However, once the Higgs boson mass falls below $2m_W$, one or both of the W bosons may be off mass shell and will lie towards the tail of the Breit-Wigner distribution. Thus, if the integration was performed using the Breit-Wigner distribution, most W boson masses chosen during the integration process would tend to be close to the W pole mass and hence inconsistent with the W bosons arising from low mass Higgs boson decays, which would tend to have masses far away from the W pole mass, meaning many iterations would be necessary to get the integration to converge. So for low hypothesized Higgs boson masses, with $m_H < 2m_W$, a better choice of integration variable is the m_H distribution itself, since all Higgs bosons produced will lie close to the peak of the Breit-Wigner distribution, meaning that the integration will converge more rapidly. To simplify the calculation, the m_H^2 distribution is used instead of the m_H distribution.

An integration over $p_x^{\nu_1}$, $p_y^{\nu_1}$, $m_{W_1}^2$ and m_H^2 was also tested to evaluate the Higgs boson event probability for high hypothesized Higgs boson mass, $m_H > 2m_W$, as described in Section 7.5. However, this testing indicated that there were more cases where no solutions could be found for a given set of $p_x^{\nu_1}$, $p_y^{\nu_1}$, $m_{W_1}^2$ and m_H^2. Thus, performing the integral over $p_x^{\nu_1}$, $p_y^{\nu_1}$, $p_z^{\nu_1}$ and m_H^2 gave a lower error and improved performance so these variables were used for the integration for the full range of hypothesized Higgs boson masses, from $120 < m_H < 200$ GeV.

This integration may be performed starting from the differential cross section for the Higgs, which with the use of Equations 7.4, 7.5 and 7.3 may be written as:

$$\begin{aligned}\frac{d\sigma(m_H)}{dy} &= \sum_{i,j}\int \frac{|\mathcal{M}_{ij}(\alpha)|^2}{8x_1x_2E_{beam}^2(2\pi)^8 2^4}\frac{d^3p^{l_1}}{E^{l_1}}\frac{d^3p^{l_2}}{E^{l_2}}\frac{d^3p^{\nu_1}}{E^{\nu_1}}\frac{d^3p^{\nu_2}}{E^{\nu_2}} \\ &\quad \times\delta^3(L_{l_1}-p_{l_1})\delta^3(L_{l_2}-p_{l_2})\delta(k_x-\sum p_{x_i})\delta(k_y-\sum p_{y_i}) \\ &= \sum_{i,j}\int \frac{|\mathcal{M}_{ij}(\alpha)|^2}{128x_1x_2E_{beam}^2(2\pi)^8}\frac{dp_x^{\nu_1}dp_y^{\nu_1}dp_z^{\nu_1}dp_z^{\nu_2}}{E^{l_1}E^{l_2}E^{\nu_1}E^{\nu_2}}\end{aligned} \tag{7.11}$$

where E^{l_i} and p_{l_i} are the energy and three momentum of lepton i and E^{ν_i} and p_{ν_i} are the energy and three momentum of neutrino i and the other variables are as defined in Equation 7.5.

In order to integrate over m_H^2, it is necessary to perform a change of variables from $p_x^{\nu_1}$, $p_y^{\nu_1}$, $p_z^{\nu_1}$ and $p_z^{\nu_2}$ to $p_x^{\nu_1}$, $p_y^{\nu_1}$, $p_z^{\nu_1}$ and m_H^2. Assuming the neutrinos are massless, the three momenta of the neutrinos gives 6 unknowns in the final state but this can be reduced to 4 unknowns overall if it is assumed that transverse momentum is conserved. These 4 unknowns are integrated over and all other variables must therefore be expressed in terms of these variables. For this change of variables, $p_z^{\nu_2}$ must be expressed in terms of $p_x^{\nu_1}$, $p_y^{\nu_1}$, $p_z^{\nu_1}$, m_H^2 and the visible lepton momenta. To solve for $p_z^{\nu_2}$, it is necessary to start with the expression for m_H^2:

$$\begin{aligned}m_H^2 &= (E^H)^2-(P^H)^2 \\ &= (E^{l_1}+E^{l_2}+E^{\nu_1}+E^{\nu_2})^2-(\mathbf{p^{l_1}}+\mathbf{p^{l_2}}+\mathbf{p^{\nu_1}}+\mathbf{p^{\nu_2}})^\mathbf{2}\end{aligned} \tag{7.12}$$

Writing $E = E^{l_1}+E^{l_2}+E^{\nu_1}$, $Q_x = p_x^{l_1}+p_x^{l_2}+p_x^{\nu_1}+p_x^{\nu_2}$, $Q_y = p_y^{l_1}+p_y^{l_2}+p_y^{\nu_1}+p_y^{\nu_2}$ and $Z = p_z^{l_1}+p_z^{l_2}+p_z^{\nu_1}$, this may be rewritten:

$$\begin{aligned}m_H^2 &= (E+E^{\nu_2})^2-Q_x^2-Q_y^2-(Z+p_z^{\nu_2})^2 \\ &= E^2+(E^{\nu^2})^2+2EE^{\nu_2}-Q_x^2-Q_y^2-Z^2-(p_z^{\nu_2})^2-2Zp_z^{\nu_2}\end{aligned} \tag{7.13}$$

Defining $T^2 = (p_x^{\nu_2})^2 + (p_y^{\nu_2})^2$ allows the energy of the second neutrino to be written as $E_{\nu_2} = \sqrt{T^2 + (p_z^{\nu_2})^2}$. This allows the original equation to be expressed as:

$$\begin{aligned} m_H^2 &= E^2 + T^2 + 2E\sqrt{T^2 + (p_z^{\nu_2})^2} - Q_x^2 - Q_y^2 - Z^2 - 2Zp_z^{\nu_2} \\ 0 &= m_H^2 - E^2 - T^2 + Q_x^2 + Q_y^2 + Z^2 - 2E\sqrt{T^2 + (p_z^{\nu_2})^2} + 2Zp_z^{\nu_2} \end{aligned} \tag{7.14}$$

All the terms which do not depend on the z-component of momentum may be grouped together as $A = m_H^2 - E^2 - T^2 + Q_x^2 + Q_y^2 + Z^2$, giving:

$$\begin{aligned} 0 &= A - 2E\sqrt{T^2 + (p_z^{\nu_2})^2} + 2Zp_z^{\nu_2} \\ A + 2Zp_z^{\nu_2} &= 2E\sqrt{T^2 + (p_z^{\nu_2})^2} \\ A^2 + 4(p_z^{\nu_2})^2Z^2 + 4Ap_z^{\nu_2}Z &= 4E^2(T^2 + (p_z^{\nu_2})^2) \\ 0 &= 4(Z^2 - E^2)(p_z^{\nu_2})^2 + 4AZp_z^{\nu_2} + A^2 - 4E^2T^2 \end{aligned} \tag{7.15}$$

This quadratic may be solved to express $p_z^{\nu_2}$ in terms of m_H^2, $p_x^{\nu_1}$, $p_y^{\nu_1}$ and $p_z^{\nu_1}$ as well as the measured lepton kinematics. The other remaining unknowns of the system, $p_x^{\nu_2}$ and $p_y^{\nu_2}$, may be solved for using $Q_x = p_x^{l_1} + p_x^{l_2} + p_x^{\nu_1} + p_x^{\nu_2}$ and $Q_y = p_y^{l_1} + p_y^{l_2} + p_y^{\nu_1} + p_y^{\nu_2}$. For a LO process, the Higgs boson has no p_T and $Q_x = Q_y = 0$, therefore this is used as a first approximation.

In order to transform the integral from $dp_z^{\nu_2}$ to m_H^2 it is also necessary to evaluate the Jacobian since the new integral is related to the old by:

$$dp_z^{\nu_2} = \frac{1}{|J|}dm_H^2 = \frac{1}{|\frac{\partial m_H^2}{\partial p_z^{\nu_2}}|}dm_H^2 \tag{7.16}$$

where a general Jacobian is defined as:

$$J = \begin{bmatrix} \frac{\partial y_1}{\partial x_1} & \cdots & \frac{\partial y_1}{\partial x_n} \\ \vdots & \ddots & \vdots \\ \frac{\partial y_m}{\partial x_1} & \cdots & \frac{\partial y_m}{\partial x_n} \end{bmatrix}$$

The Jacobian may be evaluated using Equation 7.15 to give:

$$J = 2E^H \frac{p_z^{\nu_2}}{E^{\nu_2}} - 2P_z^H \tag{7.17}$$

where E^H is the energy of the Higgs boson and P_z^H is the z-component of Higgs boson momentum.

This gives a final formula for the Higgs boson event probability:

$$\frac{d\sigma(m_H)}{dy} = \sum_{i,j} \int \frac{|\mathcal{M}_{ij}(\alpha)|^2}{128x_1x_2E_{beam}^2(2\pi)^8} \frac{dp_x^{\nu_1}dp_y^{\nu_1}dp_z^{\nu_1}dm_H^2}{E^{l_1}E^{l_2}E^{\nu_1}E^{\nu_2}} \frac{1}{|J|} \tag{7.18}$$

where the two possible solutions to the quadratic given in Equation 7.15, along with their corresponding Jacobians, must be summed over.

7.3.2 WW event probability

For SM WW production, it is assumed that the W bosons are on mass shell and will occupy a narrow region of phase space in terms of m_W. Hence it is sensible to perform a transformation of variables from p_{x,ν_1}, p_{y,ν_1} to m_{W_1}, m_{W_2} via:

$$dp_x^{\nu_1} dp_y^{\nu_1} = \frac{1}{|\frac{\partial(m_H^2, m_{W_1}^2)}{\partial(p_x^{\nu_1}, p_y^{\nu_1})}|} dm_{W_1}^2 dm_{W_2}^2 \tag{7.19}$$

The same method to solve for $p_x^{\nu_1}, p_y^{\nu_1}$ in terms of $p_z^{\nu_1}, p_z^{\nu_2}, m_{W_1}$ and m_{W_2} may be used as is described in Section 7.3.1. However, this time, it is necessary to start with m_{W_1} and m_{W_2} and assume that the leptons and neutrinos are massless:

$$\begin{aligned} m_{W_1}^2 &= (p^{l_1} + p^{\nu_1})^2 = 2(p^{l_1}.p^{\nu_1}) = 2(E^{l_1}E^{\nu_1} - p_x^{l_1}p_x^{\nu_1} - p_y^{l_1}p_y^{\nu_1} - p_z^{l_1}p_z^{\nu_1}) \\ m_{W_2}^2 &= (p^{l_2} + p^{\nu_2})^2 = 2(p^{l_2}.p^{\nu_2}) = 2(E^{l_2}E^{\nu_2} - p_x^{l_2}p_x^{\nu_2} - p_y^{l_2}p_y^{\nu_2} - p_z^{l_2}p_z^{\nu_2}) \end{aligned} \tag{7.20}$$

The details of the calculation are rather long and may be seen in Ref. [92] and numerical methods must be used [98] to evaluate the final solutions. The WW event probability is given by:

$$\frac{d\sigma_{WW}}{dy} = \sum_{i,j} \int \frac{|\mathcal{M}_{ij}(\alpha)|^2}{128 x_1 x_2 E_{beam}^2 (2\pi)^8} \frac{dp_x^{\nu_1} dp_y^{\nu_1} dm_{W_1}^2 dm_{W_2}^2}{E^{l_1} E^{l_2} E^{\nu_1} E^{\nu_2}} \frac{1}{|J|} \tag{7.21}$$

with a Jacobian given by:

$$J = 4(E^{l_2}\frac{p_y^{\nu_1}}{E^{\nu_1}} - p_y^{l_2})(E^{l_1}\frac{p_x^{\nu_2}}{E^{\nu_2}} - p_x^{l_1}) - 4(E^{l_2}\frac{p_x^{\nu_1}}{E^{\nu_1}} - p_x^{l_2})(E^{l_1}\frac{p_y^{\nu_2}}{E^{\nu_2}} - p_y^{l_1}) \tag{7.22}$$

Equation 7.21 has 4 solutions. As for the Higgs boson event probability case, these 4 solutions must be summed over.

7.4 Importance sampling integration

Standard Monte Carlo integration draws points at random from the integration volume, not taking into account the fact that in some regions the function to be integrated over, $f(x)$, may be very small. Importance sampling integration aims to draw more points from regions in which $f(x)$ is large and less where it is small.

For example, any W bosons produced in SM WW events are assumed to be on mass shell and hence only fall within the region of space enclosed by the W Breit-Wigner mass peak and are more likely to be close to the peak than further away. Thus the integral over the W boson mass may be performed by using the W Breit-Wigner distribution as a weighting function $w(x)$ and drawing points from this weighted distribution. This gives an integral of the form:

$$\int_a^b f(x)dx = \int_a^b w(x)dx \times \frac{1}{N} \sum_{w(x)}^{N} \frac{f(x)}{w(x)} \tag{7.23}$$

where it is easy to calculate the integral of the Breit-Wigner weighting function $w(x)$. The sum from $w(x)$ to N implies N iterations drawn from $w(x)$. Similarly, integrations

over m_H are performed by drawing from a Higgs boson Breit-Wigner distribution centred around the hypothesized Higgs boson mass. The neutrino p_z is drawn from a parameterised function which has been chosen to correctly describe the data. The m_W, m_H and neutrino p_z distributions at the generator level as well as the template functions which are used in the integration are shown in Figure 7.3. Figure 7.3 shows that the Breit-Wigner distributions used in the integration accurately describe the shapes of the m_W and m_H distributions. Similarly, the parameterisation used for the neutrino p_z also agrees well with the generator level neutrino p_z distribution.

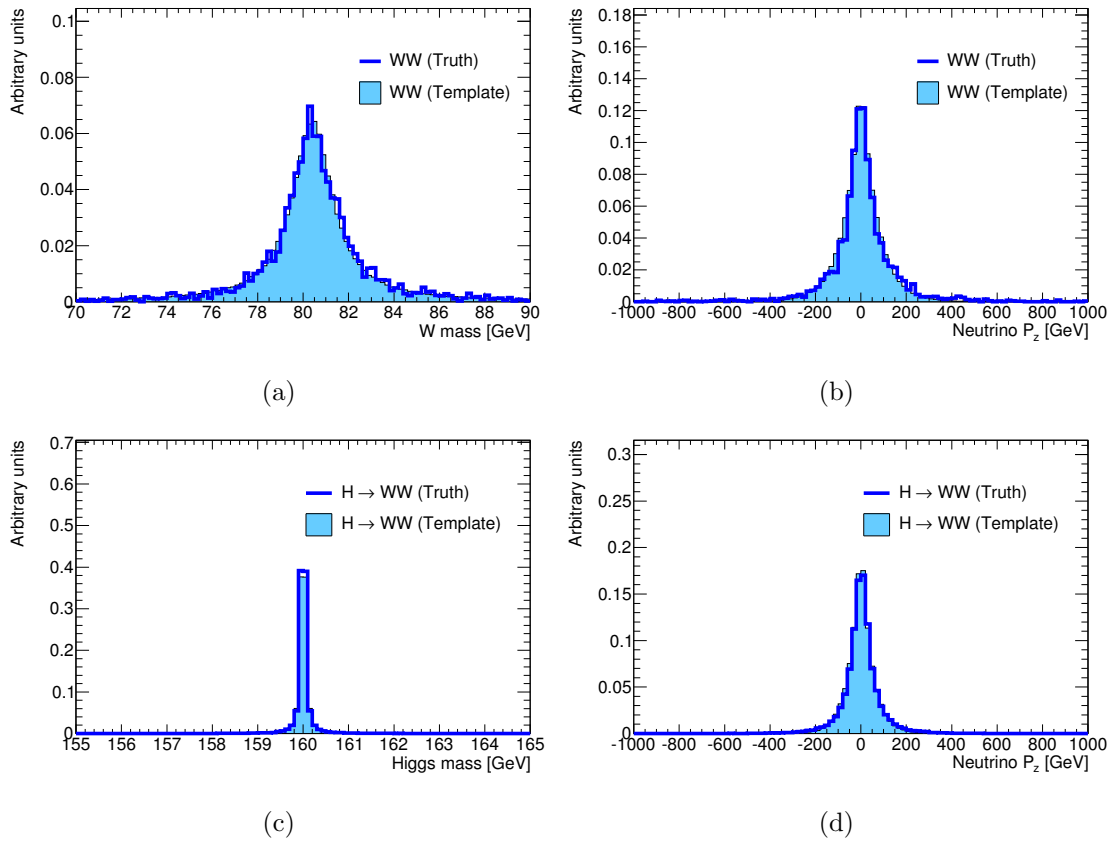

Figure 7.3: A comparison of template distributions from which variables are drawn during the importance sampling integration and the distributions of the variables at generator level. The first row shows the distributions relevant to the WW integration: the mass of the W boson (a) and the p_z distribution of the neutrinos (b). The second row shows the distributions used during the Higgs boson integration: the mass of the Higgs boson for a sample with $m_H = 160$ GeV (c) and the p_z distribution of the neutrinos (d).

Figure 7.4 shows the generator level distributions of neutrino p_x and p_y. These distributions are relatively flat between -50 and 50 GeV and drop off after this. To ensure that the tails of the distribution are covered by the integration, a flat distribution between -60 and 60 GeV is used. Any mismatch between the input distributions for the integration and the true underlying distributions should not affect the performance of the integration as long as the number of iterations is large enough to account for those iterations which fall on the tails of the distribution and do not contribute very much.

A constraint is applied when randomly choosing neutrino $p_x^{\nu_1}$ and $p_y^{\nu_1}$ during the Higgs boson event probability integration. Since no neutrinos have $|p_x|$ or $|p_y| > 60$ GeV, any neutrino $p_x^{\nu_1}$ and $p_y^{\nu_1}$ which gives a solution with $|p_x^{\nu_2}|$ or $|p_y^{\nu_2}| > 60$, using $Q_x = p_x^{l_1} + p_x^{l_2} + p_x^{\nu_1} + p_x^{\nu_2}$ and similarly for Q_y, is discarded before the unknown kinematics and event probability are calculated. $p_x^{\nu_1}$ or $p_y^{\nu_1}$ is re-chosen repeatedly until $|p_x|$ and $|p_y|$ are less than 60 GeV. This dramatically increases the number of iterations for which valid solutions may be found.

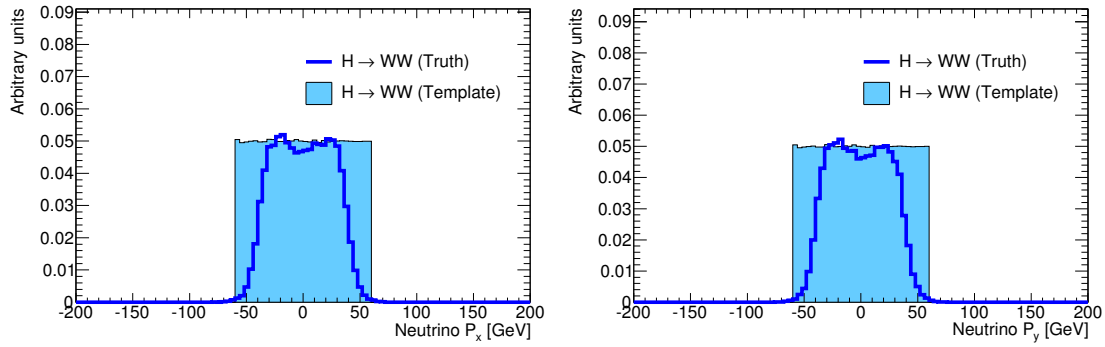

(a) (b)

Figure 7.4: A comparison of template distributions from which variables are drawn during the importance sampling integration and the distributions of the variables at generator level for neutrino p_x (a) and p_y (b) from Higgs boson events.

The integration should evenly sample the integration region when the weights are taken into account. To test this, distributions of the points drawn from the template function multiplied by their associated weights may be checked. This is shown in Figure 7.5 for the neutrino p_z distribution. This distribution is flat, showing that the importance sampling integration correctly samples the full phase space evenly.

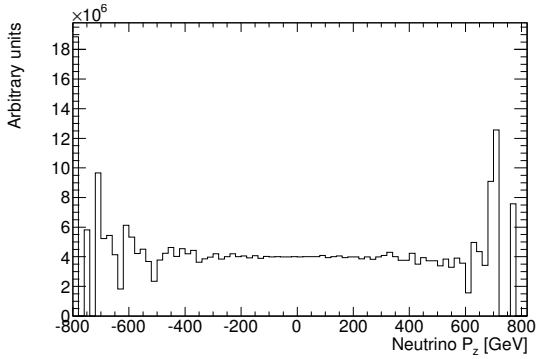

Figure 7.5: Neutrino p_z distribution used for the integration multiplied by its associated weight.

7.5 Integrated matrix element likelihood

There are many different choices of integration variables which may be used to account for the unknowns of the system, some of which have been discussed in Section 7.3. If there were an infinite number of iterations, all sets of integration variables should achieve the same result however this level of precision cannot be achieved in practice. Thus it is necessary to choose the set of integration variables which allows the integration to converge with the smallest number of iterations. Figure 7.6 shows the matrix element likelihood for test MC@NLO Higgs boson and WW samples, consisting of 500 events each, with integrations performed over $p_z^{\nu_1}$, $p_z^{\nu_2}$, $m^2_{W_1}$ and $m^2_{W_2}$ with 10,000 iterations. This shows reasonable separation between Higgs boson events and SM WW events however there is quite a lot of overlap, suggesting that the integration is perhaps not optimal given the number of iterations.

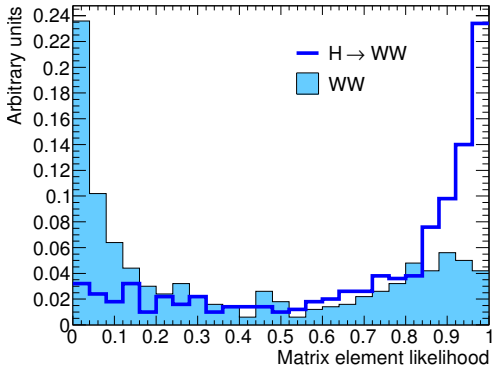

Figure 7.6: Integrated likelihood ratio for test MC@NLO Higgs boson and WW samples. The Higgs boson sample has a mass of 160 GeV. The integration is performed over $p_z^{\nu_1}$, $p_z^{\nu_2}$, $m^2_{W_1}$ and $m^2_{W_2}$. No transfer functions are applied. The matrix element is evaluated at $m_H = 160$ GeV.

An investigation of other possible integration variables is shown in Figure 7.7 for integrations performed over $p_z^{\nu_1}$, $p_z^{\nu_2}$, $m^2_{W_1}$ and $m^2_{W_2}$ for the WW event probability and using a change of variables to $p_z^{\nu_1}$, $p_z^{\nu_2}$, $m^2_{W_1}$ and m^2_H and $p_x^{\nu_1}$, $p_y^{\nu_1}$, $p_z^{\nu_1}$ and m^2_H for the Higgs boson event probability. The same test samples as previously are used, consisting of 500 events with 10,000 iterations. The top two figures show the matrix element likelihood with all events included and the bottom two show the distributions once all events with zero Higgs boson event probability have been excluded. This figure indicates that the integral over $p_z^{\nu_1}$, $p_z^{\nu_2}$, $m^2_{W_1}$ and m^2_H has relatively many more events with zero Higgs boson event probability. This is because, for some events, it is not possible to find any valid solutions, even after 10,000 iterations, due to the very narrow Higgs boson Breit-Wigner peak which provides a very strong constraint. The integration performed over $m^2_{W_1}$, m^2_H is constrained not just by the Higgs boson Breit-Wigner but also by that of the W boson so has a larger peak at zero than that performed over m^2_H. This is because, if the measured event kinematics are rather far from their true values (due to detector resolution for example), then if the integration variable distributions are very narrow many of the values chosen at

random during the integration are inconsistent with the observed kinematics and have no valid kinematic solution. If no solutions are found within the 10,000 iterations, the event is assigned a zero Higgs boson event probability. This suggests that, in order to avoid increasing the number of iterations, the correct choice of integration variables to evaluate the Higgs boson event probability is $p_x^{\nu_1}$, $p_y^{\nu_1}$, $p_z^{\nu_1}$ and m_H^2.

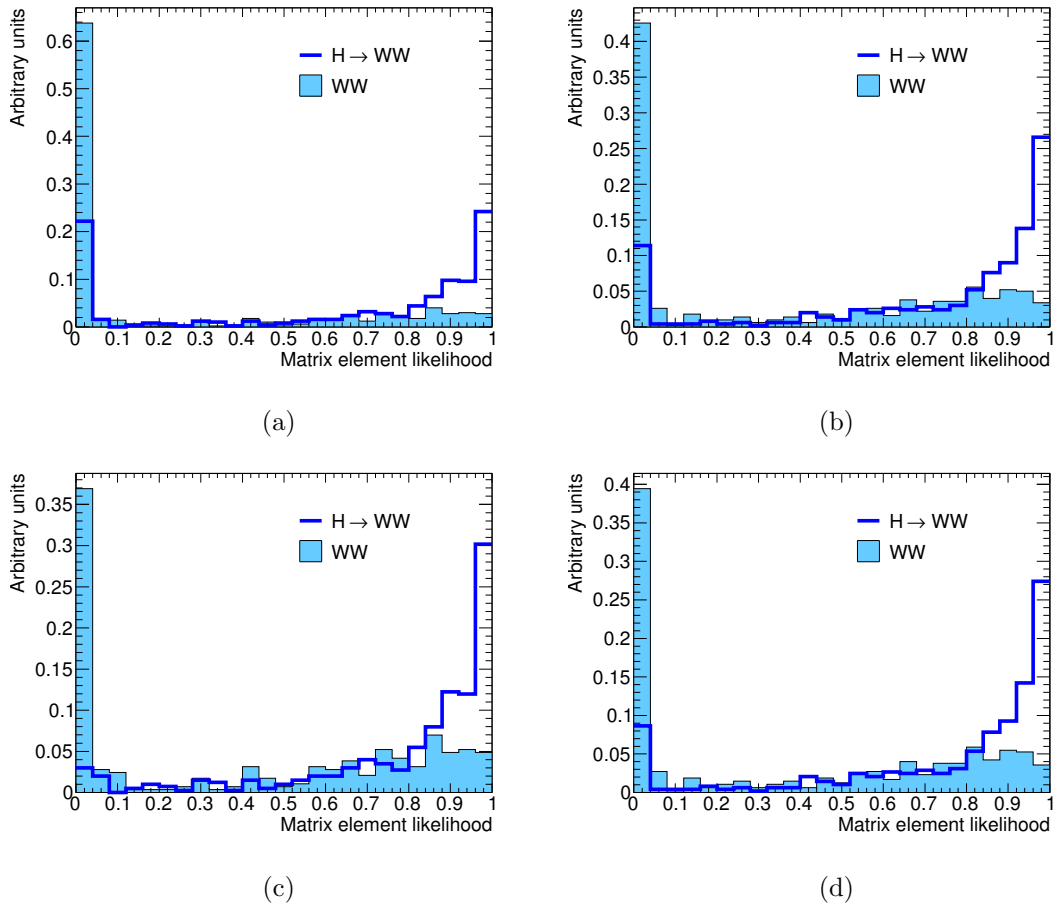

Figure 7.7: Integrated likelihood ratio for test MC@NLO Higgs boson and WW samples. The Higgs boson sample has a mass of 160 GeV. The integration is performed over $p_z^{\nu_1}$, $p_z^{\nu_2}$, $m_{W_1}^2$ and $m_{W_2}^2$ for the WW event probability. No transfer functions are applied. The matrix element is evaluated at $m_H = 160$ GeV. The integration for the Higgs boson event probability is performed over $p_z^{\nu_1}$, $p_z^{\nu_2}$, $m_{W_1}^2$ and m_H^2 in (a) and (c) and $p_x^{\nu_1}$, $p_y^{\nu_1}$, $p_z^{\nu_1}$ and m_H^2 in (b) and (d). Figures (a) and (b) show the matrix element likelihood ratio for all events and Figures (c) and (d) show the same distributions once all events with no valid solutions have been removed.

At this stage, the total x-component of the system is modelled using $Q_x = p_x^{l_1} + p_x^{l_2} + p_x^{\nu_1} + p_x^{\nu_2} = 0$ and similarly for the y-component. This assumes that the Higgs boson has zero p_T, which is not necessarily correct and is further discussed later in this section. One way to model the true Q_x, Q_y of the system is to use the missing E_x, E_y and let $Q_x = p_x^{l_1} + p_x^{l_2} + E_x^{miss}$ and $Q_y = p_y^{l_1} + p_y^{l_2} + E_y^{miss}$ so that Q_x and Q_y are not necessarily zero. Using this, the matrix element likelihood ratio for the test Higgs boson and WW samples with the integration performed over $p_x^{\nu_1}$, $p_y^{\nu_1}$, $p_z^{\nu_1}$ and m_H^2 is shown in Figure 7.8.

This figure indicates that once this more realistic model of the x- and y-components of the system has been incorporated, the performance of the matrix element likelihood improves, with better separation of Higgs boson and SM WW events and far fewer events with no valid solutions for the Higgs boson event probability. The performance of the matrix element likelihood is assessed by calculating the significance, defined as [99]:

$$S = \sqrt{2[(N_S + N_B)\ln(1 + \frac{N_S}{N_B}) - N_S]} \tag{7.24}$$

obtained when requiring the events to have a matrix element likelihood larger than a given value, with the cut value varied from 0 to 1 in steps of 0.04 to obtain the maximum possible significance. The setup which has the largest maximum significance has the best performance in terms of separating signal from background.

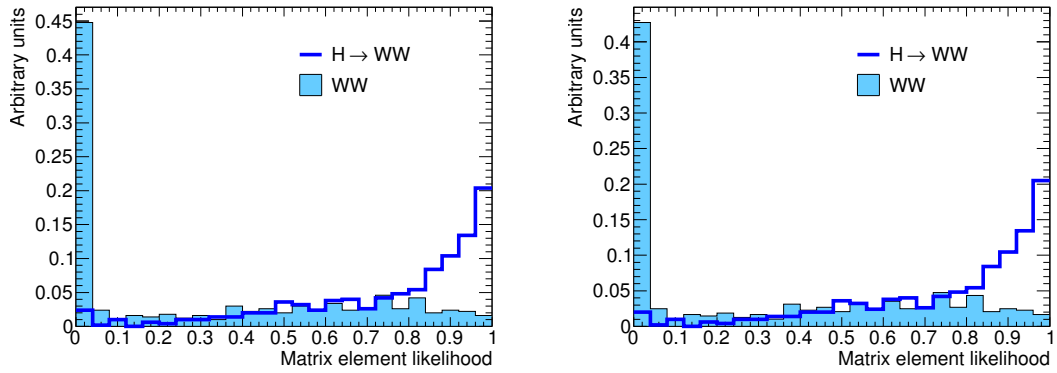

(a) (b)

Figure 7.8: Integrated likelihood ratio for test MC@NLO Higgs boson and WW samples. The Higgs boson sample has a mass of 160 GeV. The integration is performed over m_H, $p_x^{\nu_1}$, $p_y^{\nu_1}$, $p_z^{\nu_1}$. No transfer functions are applied. The matrix element is evaluated at $m_H = 160$ GeV. Events with no solutions for the Higgs boson event probability have been explicitly excluded in (a) and all events are included in (b). Previously, $Q_x = Q_y = 0$. In this case, $Q_x = p_x^{l_1} + p_x^{l_2} + E_x^{miss}$ and similarly for Q_y.

7.6 Matrix element likelihoods with transfer functions

The next step in optimising the matrix element likelihood is the inclusion of transfer functions to account for the detector resolution. A simple method is used to apply these transfer functions as a first test of the method. The transfer functions are applied by varying the reconstructed quantities according to the detector resolution to account for the fact that the measured kinematics may be far from their true values. The resolutions for different objects have been determined by the ATLAS combined performance groups and are described briefly below.

Muon smearing is described in Ref. [100]. The smeared combined muon p_T is given by:

$$p'_T(CB) = p_T(CB)[1 + \frac{\frac{\Delta_{MS}}{\sigma^2_{MS}} + \frac{\Delta_{ID}}{\sigma^2_{ID}}}{\frac{1}{\sigma^2_{MS}} + \frac{1}{\sigma^2_{ID}}}] \tag{7.25}$$

where CB refers to combined muons reconstructed using a statistical combination of MS and ID tracks, $\Delta(MS, ID)$ gives the total correction applied to the MS or ID p_T and $\sigma(MS, ID)$ is the resolution. These values are different in the barrel, transition and endcap regions and are given in Ref. [100].

Electron energy resolution is parameterised at ATLAS using:

$$\frac{\sigma}{E} = \frac{S}{\sqrt{E}} \oplus C \tag{7.26}$$

where σ/E is the fractional energy resolution, S is the sampling term and C is the constant term.

The energy resolution differs between different regions of the detector, thus S and C also differ. Their values in given η regions are shown in Table 7.1.

$\lvert\eta\rvert$-region	S	C
$\lvert\eta\rvert < 0.6$	0.1	0.007
$\lvert\eta\rvert \geq 0.6$	0.15	0.007

Table 7.1: Sampling term, S, and constant term, C, used to parameterise the fractional electron energy resolution, σ/E, described by Equation 7.26.

Figure 7.9 shows the difference between the lepton p_T at the reconstructed level and after smearing for electrons and muons. This shows that, for both cases, the difference between the measured p_T is generally within 1 GeV of the true p_T, with a smaller difference for muons, which has improved resolution with respect to electrons due to the combination of tracks from the inner detector and muon spectrometer. This suggests that including the lepton transfer functions in the calculation is not expected to have a significant impact on the matrix element likelihood ratio.

The matrix element likelihood ratio for the same test samples is shown in Figure 7.10 after smearing the reconstructed lepton p_T. The integration is performed over $p_x^{\nu_1}$, $p_y^{\nu_1}$, $p_z^{\nu_1}$ and m_H^2 and $Q_x = p_x^{l_1} + p_x^{l_2} + E_x^{miss}$ and similarly for Q_y.

A comparison of the likelihood ratio plots before and after lepton smearing, shown in Figures 7.8(b) and 7.10 respectively, show similar separation between the Higgs signal and WW background. Therefore, the effect of the lepton resolution on the matrix element likelihood distribution appears to be small. This is due to the excellent resolution of the ATLAS detector: measured lepton energies are very close to their true values. The missing E_T resolution is not so good due to the complexity of the missing E_T reconstruction. This involves the precise measurement not only of the hard objects in the event but also of the soft radiation in the underlying event as well as contributions from pileup, which must all be very well-measured to achieve good missing E_T resolution.

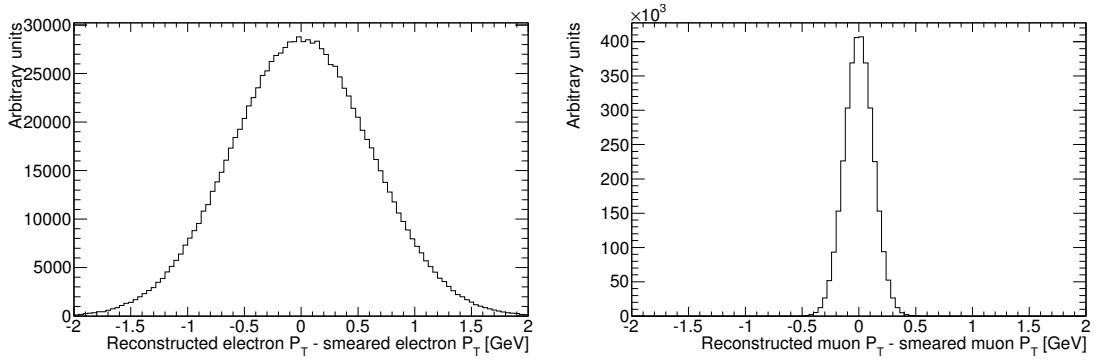

(a) (b)

Figure 7.9: This figure shows the difference between the reconstructed lepton p_T and the lepton p_T after smearing for electrons (a) and muons (b).

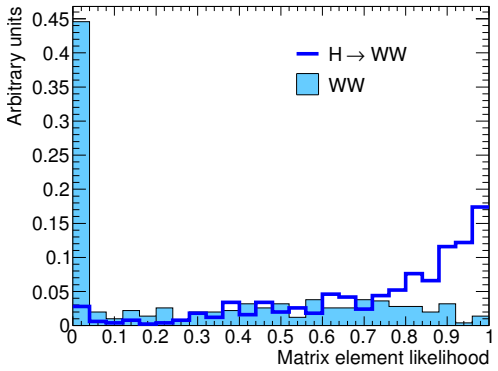

Figure 7.10: Integrated likelihood ratio for test MC@NLO Higgs boson and WW samples. The Higgs boson sample has a mass of 160 GeV. The integration is performed over $p_x^{\nu_1}$, $p_y^{\nu_1}$, $p_z^{\nu_1}$ and m_H^2. Lepton smearing is applied. The matrix element is evaluated at $m_H = 160$ GeV. $Q_x = p_x^{l_1} + p_x^{l_2} + E_x^{miss}$ and similarly for Q_y.

Previous studies using 7 TeV pp collision data at ATLAS [101, 102] have measured the missing E_T resolution to be well described by the function:

$$\sigma(E_x^{miss}, E_y^{miss}) = \alpha\sqrt{\sum E_T} \tag{7.27}$$

where $\alpha = 0.49$. Therefore, the E_x^{miss} and E_y^{miss} of the events is smeared by drawing from Gaussian distributions with widths given by Equation 7.27. This corresponds to the application of the transfer function given in Equation 7.3. The smeared E_x^{miss} and E_y^{miss} are used in the matrix element calculation as a constraint on the total x- and y-components of the system such that $Q_x = p_x^{l_1} + p_x^{l_2} + E_x^{miss,smear}$, $Q_y = p_y^{1_1} + p_y^{1_2} + E_y^{miss,smear}$.

After applying the missing E_T smearing, the matrix element likelihood ratio is shown in Figure 7.11. This shows that the separation between the Higgs boson sample and the WW sample actually decreases when the missing E_T smearing is applied. This could be due to the contribution of WW events which are on the tail of the missing E_T smearing

distribution falling wrongly into the Higgs boson signal region, causing large contributions which would not be there at the truth level. Therefore, the missing E_T smearing is not applied.

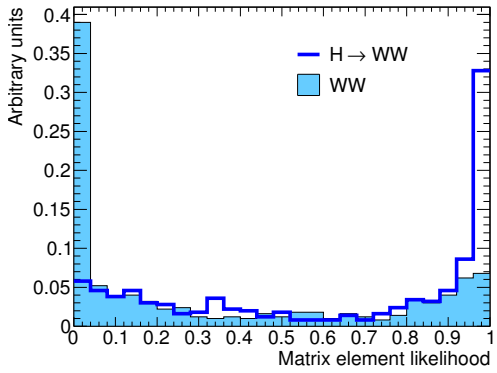

Figure 7.11: Integrated likelihood ratio for test MC@NLO Higgs boson and WW samples. The Higgs boson sample has a mass of 160 GeV. The integration is performed over $p_x^{\nu_1}$, $p_y^{\nu_1}$, $p_z^{\nu_1}$ and m_H^2. Lepton and missing E_T smearing is applied. The matrix element is evaluated at $m_H = 160$ GeV. $Q_x = p_x^{l_1} + p_x^{l_2} + E_x^{miss}$ and similarly for Q_y.

As mentioned previously, the calculation of the matrix element by MadGraph assumes that the Higgs boson has no p_T. An investigation at the truth level using MC@NLO indicates that once higher-order effects have been included, the Higgs boson is expected to have a non-zero p_T distribution which is mass dependent and also dependent on the hadronic activity (i.e. number of jets) in the event, with higher mass and larger number of jets leading to p_T distributions which are less peaked and tend to higher values. This can be seen in Figure 7.12. This figure also shows the p_T distribution of the WW pair in SM WW events and shows that this is slightly different from the Higgs boson p_T distribution, particularly for the zero jet case. This difference may be exploited to further improve the separation between Higgs boson events and WW events by weighting the Higgs boson and WW event probabilities according to where the event lies in the p_T spectrum.

After applying this p_T weighting, the matrix element likelihood ratio is shown in Figure 7.13. This shows a further small improvement in separation between Higgs boson events and SM WW events.

7.7 Simplifications

As previously mentioned in Section 7.1, only the WW event probability is used in the calculation since the WW background is the largest in this channel. While the separation using the matrix element likelihood for WW events is very good, for other types of background events it may not be optimal so future analyses may be improved by including other background processes in the likelihood.

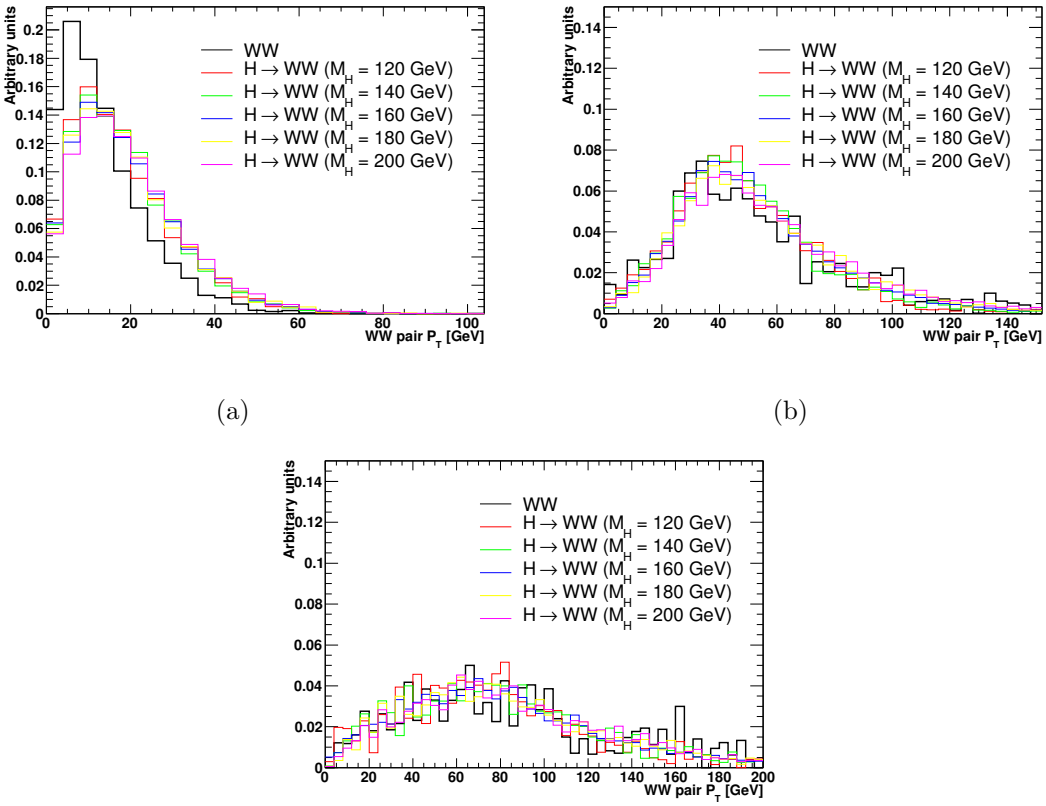

(a) (b)

(c)

Figure 7.12: p_T of WW pairs from SM WW production and $H \to WW$ production with $m_H = 120, 140, 160, 180$ and 200 GeV for the zero (a), one (b) and two (c) jet channels.

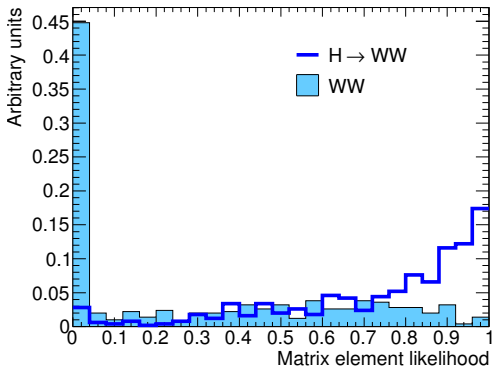

Figure 7.13: Integrated likelihood ratio for test MC@NLO Higgs boson and WW samples. The Higgs boson sample has a mass of 160 GeV. The integration is performed over $p_x^{\nu_1}$, $p_y^{\nu_1}$, $p_z^{\nu_1}$ and m_H^2. Lepton smearing is applied. The matrix element is evaluated at $m_H = 160$ GeV. $Q_x = p_x^{l_1} + p_x^{l_2} + E_x^{miss}$ and similarly for Q_y. Higgs boson p_T weighting is applied.

Chapter 8

WW cross section measurement

The cross section of WW production, σ_{WW} is defined as:

$$\sigma_{WW} = \frac{N_{Obs} - N_{Bkg}}{\epsilon A \times \mathcal{L} \times \text{ BR}} \tag{8.1}$$

where N_{Obs} is the number of observed events, N_{Bkg} is the expected number of background events, ϵA is the efficiency multiplied by the acceptance which is treated as one number, BR is the branching fraction for two W bosons to both decay leptonically, and $\mathcal{L}$ is the integrated luminosity. The acceptance is taken to be the expected number of WW events in the 35 pb^{-1} dataset, N_{WW}. This gives an acceptance times efficiency of $N_{WW}/(\sigma_{SM} \times \mathcal{L} \times \text{ BR})$.

In order to calculate the relevant parts of this formula, the events are selected using the criteria described in Section 4.7. Acceptance and efficiency scale factors are used as detailed in Chapter 5. The backgrounds are taken from MC with the exception of that arising from W+jets, which is determined as described in Section 6.3.

8.1 Systematic uncertainties

There are many sources of systematic uncertainty which contribute to the overall uncertainty on the measured WW production cross section. The luminosity uncertainty is calculated to be 11% using van der Meer scans as described in [24]. Other sources of uncertainty arise from the cross sections used to determine the expected number of signal and background events; these are also sensitive to the PDFs used, which provide another source of uncertainty. As described in Chapter 5, various scale factors are applied to the MC predictions to account for differences between data and MC. These scale factors have their own uncertainties which must be accounted for. There are also additional uncertainties inherent in the calculation of the backgrounds using data-driven methods, in particular the W+jets background which is estimated entirely using data and the Z+jets backgrounds for which the systematic uncertainty on the MC prediction is estimated using data. These sources of uncertainty are summarised in Table 8.1.

The systematic uncertainty on the WW cross section enters the measurement in the calculation of the acceptance which is used in the determination of the corss section according to Equation 8.1.

Source	Mean	Uncertainty	Influence	References
WW cross section	-	5%	MC signal acceptance	Ref [103]
W/Z+jets	-	10%	MC background estimation	Ref [104]
$W/Z+\gamma$	-	5%	MC background estimation	Ref [105]
$t\bar{t}$	-	12%	MC background estimation	Ref [106]
Jet veto eff. SF (WW signal)	96.6%	6.0%	MC diboson efficiency	Section 5.4
ee trig. SF	100%	<0.01%		Table 5.6
Single e ID eff. SF	97.0%	3.3%		Section 5.3.1
ee SF (overall)	94.1%	7.6%		-
$\mu\mu$ trig. SF	100%	<0.01%		Table 5.6
Single μ ID eff. SF	98.0%	1.0%		Section 5.3.2
$\mu\mu$ SF (overall)	96.0%	1.5%		-
$e\mu$ trig. SF	100%	<0.01%		Table 5.6
$e\mu$ SF (overall)	95.1%	4.9%		-
PDF Uncertainty on Acc.	-	1.2%	MC WW signal acc.	Ref [83]
Jet Veto on Top (MC)	-	40%	MC bkg efficiency	Ref [83]
ISR/FSR on Top (MC)	-	32%	MC bkg efficiency	Ref [83]
W+jets bkg (total)	0.54	0.32(stat.), 0.21(syst.)		Ref [83]
Z+jets bkg (total)	0.24	0.15(stat.), 0.17(syst.)		Ref [83]

Table 8.1: Table detailing the sources of systematic uncertainty considered in the WW cross section measurement.

8.2 Results

Figure 8.1 shows the M_{ll}, $\not{E}_T^{\mathrm{Rel}}$ and jet multiplicity distributions for the ee, $\mu\mu$ and $e\mu$ channels separately with all cuts prior to the plotted distribution applied. In this figure, and all other figures showing data-MC comparisons, the SM WW signal and all backgrounds are normalised to the integrated luminosity of the dataset. This shows that the agreement between data and MC is good in the ee and $e\mu$ channels. There is some discrepancy in the $\mu\mu$ channel at earlier stages in the event selection. This could be due to mismodelling of the Drell-Yan background. The use of the data-driven method to estimate the Z+jets background, described in Section 6.1, should help reduce this discrepancy.

Further evidence of this generally good agreement between data and MC is shown in Table 8.2 which shows the number of events for the signal and all of the backgrounds going through the cutflow for each channel separately and combined, with the backgrounds estimated using MC only.

The jet multiplicity distribution for ee, $\mu\mu$ and $e\mu$ channels combined after all cuts except the final jet veto is shown in Figure 8.2 and shows good data-MC agreement. The number of events after all cuts for the WW signal and all backgrounds, as well as the observed number of data events, is shown in Table 8.3. Statistical and systematic errors are shown in this table; a full discussion of sources of systematic uncertainty is given in Section 8.1. These values are used as inputs to the final calculation of the observed WW cross section, which is detailed in the following sections and in Ref. [83].

An event display of an observed candidate event in the $e\mu$ channel is shown in Figure 8.3.

Cut	WW signal	Z	W	Top	WZ	All MC	Data
			ee channel				
Two opp. sign leptons	3.73	6051.33	1.31	17.47	4.24	6078.07	6075
$M_{ll} > 15$ GeV	3.71	6043.45	1.31	17.30	4.24	6070.01	6062
Z veto	3.23	765.87	1.31	14.80	0.71	785.92	872
$\not\!\!E_T^{\mathrm{Rel}} > 40$ GeV	1.28	0.00	0.16	5.73	0.11	7.28	12
Jet veto	0.85	0	0	0.04	0.05	0.94	1
			$\mu\mu$ channel				
Two opp. sign leptons	8.18	13368.06	1.38	42.00	9.13	13428.75	12841.00
$M_{ll} > 15$ GeV	8.09	13340.17	1.38	41.46	9.13	13400.23	12767.00
Z veto	6.99	1999.60	0.89	36.28	1.64	2045.41	1936.00
$\not\!\!E_T^{\mathrm{Rel}} > 40$ GeV	2.87	0.09	0.07	13.32	0.24	16.59	14.00
Jet veto	1.74	0.01	0	0.15	0.10	2.00	2
			$e\mu$ channel				
Two opp. sign leptons	11.12	38.19	2.63	57.35	0.77	110.06	126
$\not\!\!E_T^{\mathrm{Rel}} > 20$ GeV	7.68	0.68	1.18	35.95	0.45	45.95	38
Jet veto	4.81	0.23	0.10	0.36	0.24	5.74	4
			All channels				
Two opp. sign leptons	23.05	19457.57	5.31	116.82	14.14	19616.90	19042
M_{ll}	22.94	19421.82	5.31	116.11	14.13	19580.32	18955
Z veto	21.61	2801.28	4.90	109.09	3.14	2940.02	2935
$\not\!\!E_T^{\mathrm{Rel}}$	11.83	0.77	1.41	55.00	0.80	69.82	65
Jet veto	7.40	0.24	0.10	0.55	0.39	8.68	8

Table 8.2: Table showing the number of WW signal events expected in 35 pb^{-1} of integrated luminosity as well as the expected number of background events and the observed number of data events. All backgrounds are taken from MC.

8.3 WW production cross section measurement

A maximum log-likelihood function is used to fit the WW cross section. This is based on the expected number of events from MC and the observed number of data events and uses Poisson statistics. The constructed log-likelihood for the individual channels is given by:

$$F = \ln \prod_{i=1}^{3} \frac{e^{-(N_s^i+N_b^i)}(N_s^i+N_b^i)^{N_{obs}^i}}{N_{obs}^i!},\ N_s^i = \sigma_{WW} \times \ \mathrm{BR} \times \mathcal{L} \times \epsilon A \times \ \mathrm{SF}, \tag{8.2}$$

where $i = 1, 2, 3$ corresponds to the three dilepton channels and N_S^i, N_B^i and N_{Obs}^i give the expected number of signal and background events and the observed number of data events in channel i. As previously defined, σ_{WW} is the WW production cross section, BR is the branching ratio, $\mathcal{L}$ is the integrated luminosity, ϵA is the acceptance times the efficiency and SF is the scale factor applied to correct the MC so it more closely matches data. $\epsilon A = N_{reco}/N_{prod}$ is calculated to be $7.5/105 = 0.070 \pm 0.005$. F is maximised to calculate the observed WW cross section. These results are summarised in Table 8.4.

These results give an overall cross section, with statistical and systematic uncertainties included, of:

Channel	ee	$\mu\mu$	$e\mu$	Combined
Observed Events	1	2	5	8
MC WW Signal	0.85±0.02±0.13	1.74±0.04±0.24	4.81±0.06±0.68	7.40±0.07±1.05
Backgrounds				
Top (MC)	0.04±0.02±0.03	0.15±0.06±0.08	0.36±0.10±0.19	0.55±0.12±0.30
W+jets (Data)	0.08±0.05±0.03	0±0.29±0.10	0.46±0.12±0.17	0.54±0.32±0.21
Z+jets (MC)	0±0.10±0.07	0.01±0.10±0.07	0.23±0.06±0.15	0.24±0.15±0.17
Other dibosons (MC)	0.05±0.01±0.01	0.10±0.01±0.01	0.24±0.05±0.03	0.39±0.04±0.06
Total Background	0.17±0.11±0.09	0.26±0.31±0.15	1.29±0.17±0.32	1.72±0.37±0.45

Table 8.3: Expected number of events for the WW signal, all backgrounds and data in 35 pb^{-1} of integrated luminosity. The backgrounds are determined as indicated in the table. The central values of the Z+jets backgrounds are taken from MC while the uncertainties are measured using a data-driven method. The errors shown are statistical (first) and systematic (second).

Channel	N_S	N_B	N_{Obs}	σ_{WW} [pb]
ee	0.85	0.17	1	45^{+74}_{-38}
$\mu\mu$	1.74	0.26	2	46^{+47}_{-29}
$e\mu$	4.81	1.29	5	36^{+25}_{-19}
Total	7.49	1.72	8	40^{+20}_{-16}

Table 8.4: Expected and observed number of events used in the calculation of the SM WW cross section measurement and the corresponding calculated cross section. Quoted uncertainties are statistical only.

$$\sigma_{WW} = 40^{+20}_{-16}(\text{stat.}) \pm 7(\text{syst.}) \text{ pb [83].}$$

This is in agreement with the SM NLO prediction of 46 ± 3 pb. The signal significance is calculated to be 3 σ, corresponding to a probability of 1.4×10^{-3} for the background to fluctuate up to the observed number of data events.

The dominant source of uncertainty on this measurement is statistical with the current dataset, amounting to a 44% uncertainty. Systematic uncertainties correspond to a 16.4% uncertainty in total.This uncertainty is calculated using the following formula:

$$\sigma_{syst}/\sigma_{WW} = \sqrt{(\Delta L/L)^2 + (\Delta A/A)^2 + (\Delta N_b/(N_{obs} - N_b))^2} \tag{8.3}$$

where the fractional uncertainty on the luminosity, $\Delta L/L$, is 11%; $\Delta A/A$, the fractional uncertainty on SM WW acceptance, is 7.4% and the uncertainty on the number of background events, $\Delta N_b/(N_{obs} - N_b)$, is 34%.

The systematic uncertainties do not enter the likelihood directly but are instead calculated using Equation 8.3.

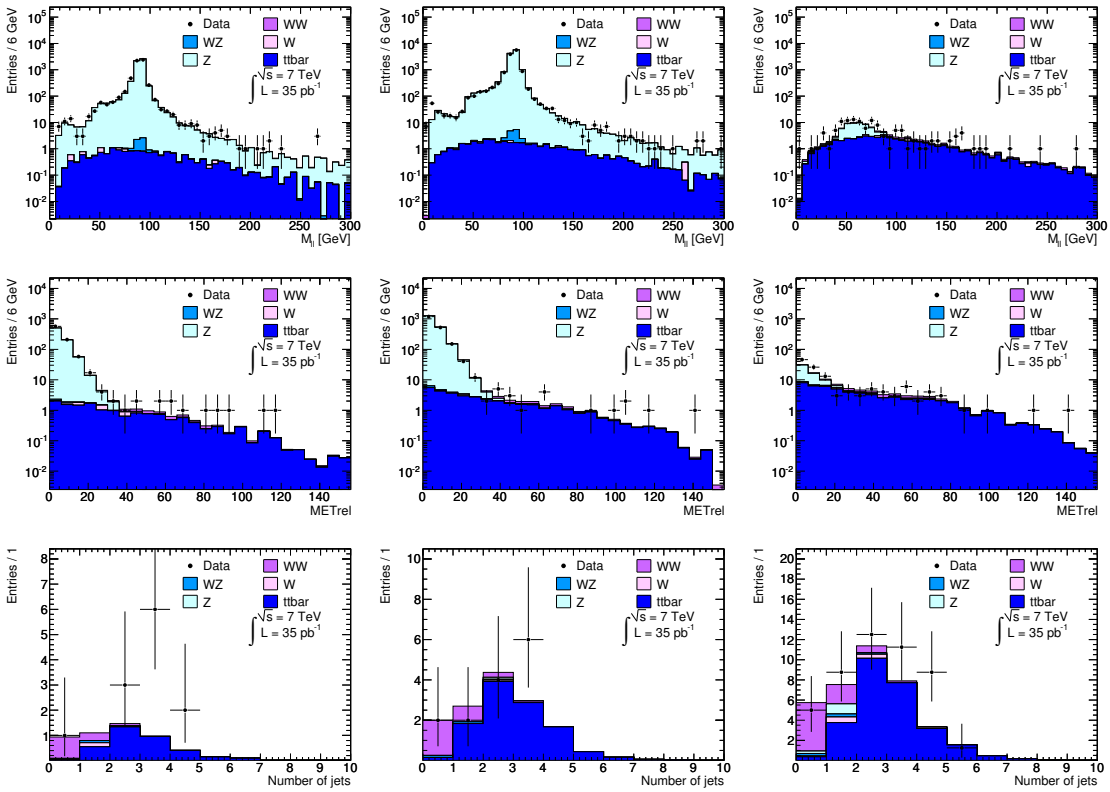

Figure 8.1: Event distributions for the WW cross section in the ee, $\mu\mu$ and $e\mu$ channels (from left-right) with all cuts prior to the one shown applied. The distributions in this figure are (from top-bottom): M_{ll}, $\not{E}_T^{\mathrm{Rel}}$ and the number of jets with $p_T > 25$ GeV.

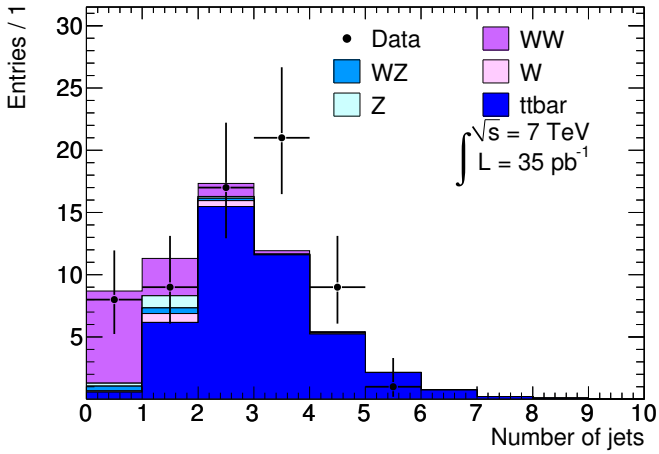

Figure 8.2: Jet multiplicity distribution for the SM WW cross section measurement in all channels combined after all cuts except the jet veto.

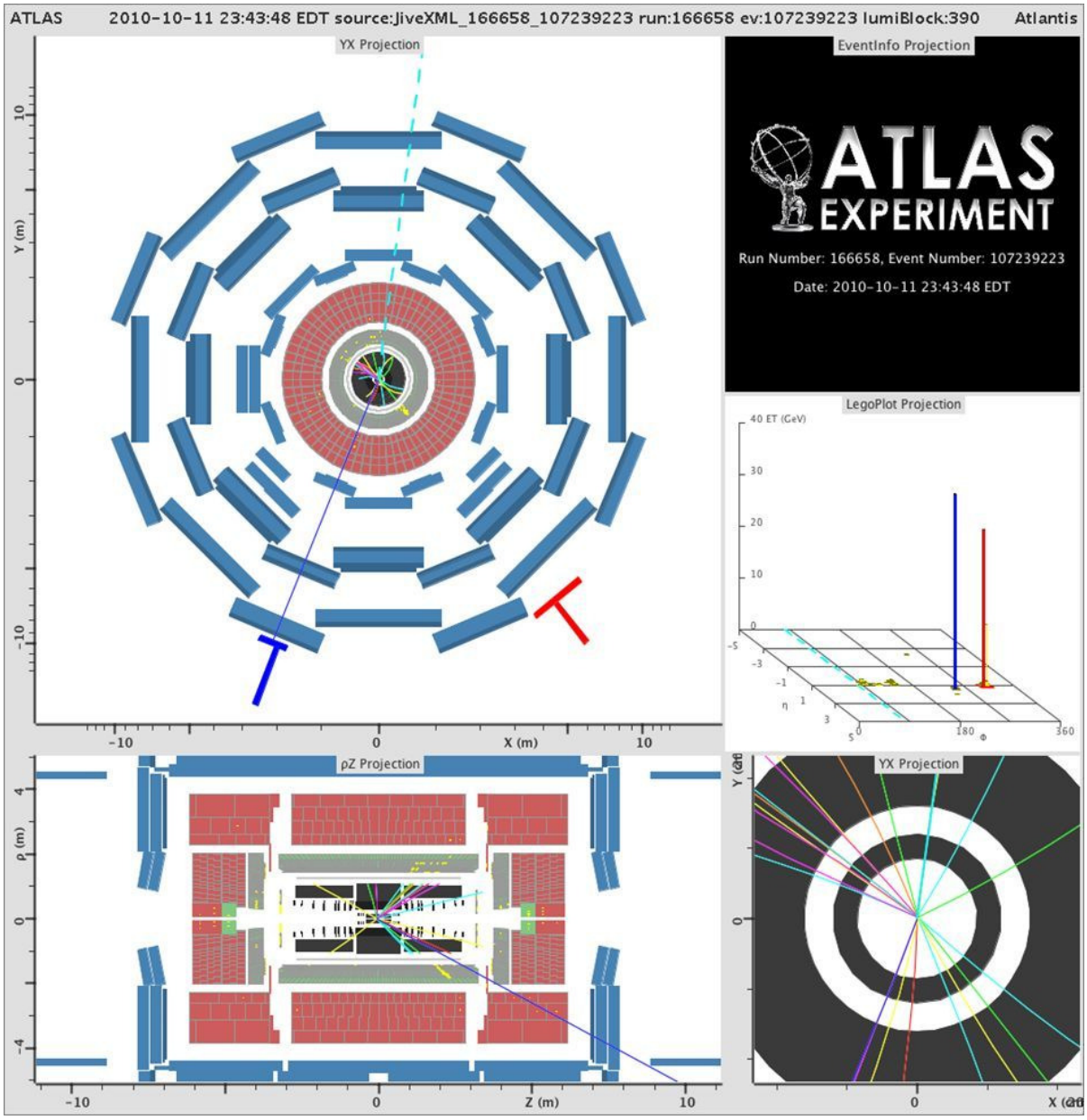

Figure 8.3: An event display for a candidate from $WW \to e\nu\mu\nu_\mu$. The electron is shown in red, the muon in dark blue and the direction of the missing E_T is indicated with a dotted light blue line.

Chapter 9

$H \rightarrow WW$ search results using the cut-based method

This chapter shows the final results obtained in the search for the Higgs boson in the WW decay mode using the simple cut-based selection described in Section 4.8. The systematic uncertainties associated with the measurement are discussed in Section 9.1. Section 9.2 shows the final expected and observed number of events at all stages of event selection, with separate discussions given for the zero, one and two jet channels. Finally, the calculation of the limits on Higgs boson production at ATLAS is described in Section 9.3.

9.1 Systematic uncertainties

Similar sources of systematic uncertainty affect the search for $H \rightarrow WW$ to those which are relevant to the WW production cross section, described in Section 8.1. These uncertainties are summarised in Table 9.1 and are all given as fractional uncertainties.

Source of Uncertainty	Treatment in analysis
Jet energy resolution (JER)	$\sim$ 14%, see Ref. [107]
Jet energy scale (JES)	$<$ 10% for $p_{\mathrm{T}} > 15$ GeV and $\lvert\eta\rvert < 4.5$.
Electron selection efficiency	$6 - 16\%$ as a function of p_{T}
Electron energy scale	1% for $\lvert\eta\rvert < 1.4$, 3% for $1.4 < \lvert\eta\rvert < 2.5$
Electron energy resolution	Sampling term 20%, a small constant term has a large variation with η
Muon selection efficiency	1.2% for $p_{\mathrm{T}} < 20$ GeV and 0.4% for $p_{\mathrm{T}} > 20$ GeV
Muon momentum scale	η dependent scale offset in p_{T}, up to $\sim$ 3.5%
Muon momentum resolution	p_{T} and η dependent resolution smearing functions, $\leq$ 10%
b-tagging efficiency	p_{T} dependent scale factor uncertainties, 10-12%, see Ref. [81]
b-tagging mis-tag rate	up to 26%
Missing E_T	Add/subtract object uncertainties into the $E_{\mathrm{T}}^{\mathrm{miss}}$, up to 20%
Luminosity	11%

Table 9.1: Experimental sources of systematic uncertainties.

In addition to the systematic effects covered by Table 9.1, there are additional uncertainties arising from the data-driven estimation of background processes. The methods used to estimate backgrounds all work in the same way: backgrounds are estimated using a control region in data which is expected to be completely dominated by the background

process of interest. An extrapolation from this control region to the signal region is performed using a scale factor, α. It cannot be guaranteed that the control regions are completely free from contamination from other backgrounds, although the choice of good control regions should minimise this effect. However, assuming that there is some small contribution from other processes in the control region, this contribution may be modelled using a further scale factor, β. These α and β parameters also suffer from systematic uncertainties which must be accounted for in the limit setting procedure.

The sources of systematic uncertainty described in Table 9.1 should also be applied to the calculation of α and β to determine the effect on these parameters. Currently, only the W+jets background estimate in the $H + 0j$ and $H + 1j$ channels, described in Section 6.3, is taken from data. The sources of systematic uncertainty considered are the dependence on the trigger used to collect a jet-enriched sample in which to measure the fake factor, the difference in the fake factor in W+jets and dijet events, the variation of the fake factor in different data periods and the contamination from real leptons. These uncertainties, as well as the estimated number of W+jets events after all cuts have been applied are summarised in Table 9.2 for the $H + 0j$ and $H + 1j$ channels.

Channel	Estimated background	Statistical uncertainty	Systematic uncertainty
$H + 0j$ analysis			
ee channel	0.02	0.01	0.1
$\mu\mu$ channel	0.0	0.1	0.1
$e\mu$ channel	0.01	0.01	0.02
$H + 1j$ analysis			
ee channel	0.03	0.02	0.01
$\mu\mu$ channel	0.0	0.1	0.1
$e\mu$ channel	0.02	0.02	0.01

Table 9.2: Systematic and statistical uncertainties on the W+jets background estimate in the $H + 0j$ and $H + 1j$ channels. Uncertainties are absolute.

9.2 Results

This section shows the final data-MC agreement at all stages of the cutflow for the zero, one and two jet channels in Sections 9.2.1, 9.2.2 and 9.2.3 respectively. All tables and plots are shown with a hypothesized Higgs mass of 170 GeV. A summary of all jet bins and all hypothesized Higgs boson masses from 120 to 200 GeV is given in Section 9.2.4.

9.2.1 Zero jet channel

The expected number of events in 35 pb^{-1} of integrated luminosity from MC are compared with the observed number of events in Table 9.3 for the zero jet channel. The number of events after the common preselection is also shown in the first two lines of the table. This preselection is also applied in the $H + 1j$ and $H + 2j$ channels before requiring one and at least two jets. Observed data appear to be consistent with MC expectation.

Selection	Signal	WW	W+jets	Z+jets	top	$WZ/ZZ/W\gamma$	Total Bkg.	Observed
$m_{\ell\ell} > 15$ GeV	5.39±0.03	27.1	5.09	19500	119	15.53	19700±36.2	19800
$E_{\mathrm{T}}^{\mathrm{miss}} > 30$ GeV	4.72±0.03	17.3	3.17	44.2	100	1.28	166±2.1	173
0 jet	2.49±0.02	11.0	2.03	11.1	1.45	0.59	26.1±1.1	24
$p_T^{ll} > 30$ GeV	2.34±0.02	9.73	1.65	2.32	1.34	0.52	15.6±0.6	19
$m_{\ell\ell} < 65$ GeV	2.04±0.02	3.83	1.22	0.70	0.38	0.29	6.42±0.43	8
$\Delta\phi_{\ell\ell} < 1.8$	1.96±0.02	3.31	0.74	0.42	0.34	0.28	5.09±0.34	6
$0.75 \times m_H < m_T < m_H$	1.26±0.02	1.44	0.03	0.00	0.21	0.03	1.71±0.11	3

Table 9.3: The expected number of signal and background events based on MC in the $H + 0j$ analysis for 35 pb^{-1} of integrated luminosity. The signal numbers correspond to the case of $m_H = 170$ GeV. The 'top' refers to $t\bar{t}$ and single top backgrounds. Errors are statistical only and are calculated using the large MC samples listed in Table 4.1 and scaled to the integrated luminosity of the data sample, with the exception of the W+jets background, which is calculated using the data-driven method described in Section 6.3. The ee, $e\mu$ and $\mu\mu$ final states are summed. The first two lines show the expected and observed number of events for the common preselection which is applied in all jet bins.

Figure 9.1 shows the transverse mass distribution for ee, $\mu\mu$ and $e\mu$ channels combined in the $H + 0j$ channel once all cuts except the final cut on the transverse mass have been applied. This figure shows that once the m_T cut has been applied, a high signal to background ratio is achieved, giving maximum sensitivity to the Higgs boson if it exists.

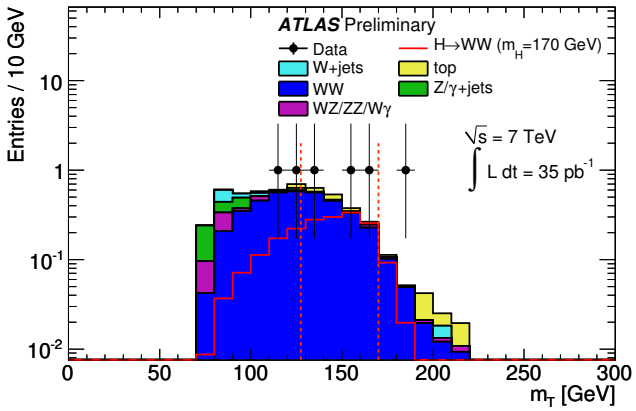

Figure 9.1: m_T distribution for the zero jet channel after all cuts except that on m_T. ee, $\mu\mu$ and $e\mu$ channels have been combined. The signal region lies within the dotted lines. Backgrounds have been estimated using MC scaled to an integrated luminosity of 35 pb^{-1}. Errors shown are statistical only.

9.2.2 One jet channel

Table 9.4 shows the observed and expected number of events in 35 pb^{-1} of integrated luminosity for the one jet channel, with backgrounds taken from MC only. As in the zero jet channel, good agreement between data and the MC background-only expectation is seen.

Selection	Signal	WW	W+jets	Z+jets	top	$WZ/ZZ/W\gamma$	Total Bkg.	Observed
1 jet	1.48±0.02	4.48	0.79	15.9	16.6	0.41	38.2±1.2	43
b-jet veto	1.47±0.02	4.41	0.70	15.7	9.44	0.41	30.7±1.2	35
$p_T^{Tot} < 30$ GeV	1.25±0.02	3.86	0.47	11.9	6.11	0.30	22.6±1.0	27
$Z \to \tau\tau$ veto	1.23±0.02	3.61	0.40	6.53	5.64	0.28	16.5±0.7	21
$m_{\ell\ell} < 65$ GeV	1.05±0.02	1.34	0.00	3.31	1.72	0.12	6.49±0.45	9
$\Delta\phi_{\ell\ell} < 1.8$	0.97±0.02	0.98	0.00	2.26	1.32	0.09	4.65±0.32	5
$0.75 \times m_H < m_T < m_H$	0.60±0.01	0.39	0.05	0.30	0.51	0.02	1.27±0.13	1

Table 9.4: The expected number of signal and background events based on MC in the $H + 1j$ analysis for 35 pb^{-1} of integrated luminosity. The signal numbers correspond to the case of $m_H = 170$ GeV. The 'top' refers to $t\bar{t}$ and single top backgrounds. Errors are statistical only and are calculated using the large MC samples listed in Table 4.1 and scaled to the integrated luminosity of the data sample, with the exception of the W+jets background, which is calculated using the data-driven method described in Section 6.3. The ee, $e\mu$ and $\mu\mu$ final states are summed.

The m_T distribution for the one jet channel after all cuts except that on m_T itself is shown in Figure 9.2. A lower signal to background ratio than the zero jet channel is expected, indicating that the bulk of the sensitivity to the Higgs boson arises from the zero jet analysis.

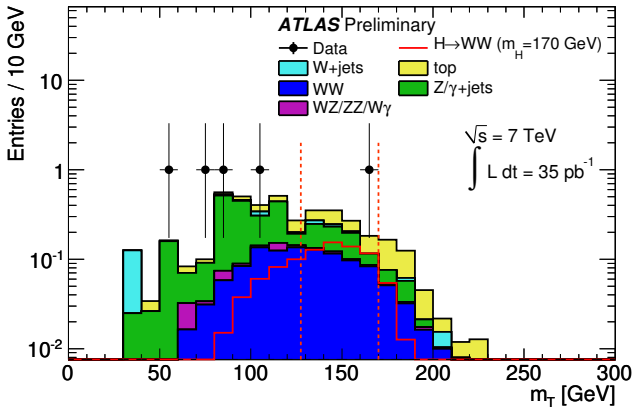

Figure 9.2: m_T distribution for the one jet channel after all cuts except the cut on m_T itself. ee, $\mu\mu$ and $e\mu$ channels have been combined. The signal region lies within the dotted lines. Backgrounds have been estimated using MC scaled to an integrated luminosity of 35 pb^{-1}. Errors shown are statistical only.

9.2.3 Two jet channel

Expected and observed number of events with 35 pb^{-1} of integrated luminosity for the two jet channel is shown in Table 9.5. After the requirement of $\eta_{j1} * \eta_{j2} < 0$, the agreement between data and MC is good however, before this, the MC background expectation appears to slightly underestimate the observed data. This could be due to an underestimation of the top background in the ee channel, as suggested by Table 6.3 in Section 6.2.

Regardless, it is not significant with the current dataset but may warrant further investigation if this deficit of expected events compared to observed events persists with more data.

Selection	Signal	WW	W+jets	Z+jets	top	$WZ/ZZ/W\gamma$	Total Background	Observed
≥ 2 jets	0.81 ± 0.01	1.86	17.1	0.35	78.3	0.33	97.9 ± 1.89	106
$\eta_{j1} * \eta_{j2} < 0$	0.52 ± 0.01	0.89	7.87	0.00	35.7	0.14	44.6 ± 1.27	46
$\Delta\eta_{jj} > 3.8$	0.25 ± 0.01	0.16	0.51	0.00	2.68	0.02	3.37 ± 0.33	5
$m_{jj} > 500$ GeV	0.17 ± 0.01	0.08	0.14	0.00	1.58	0.01	1.81 ± 0.23	3
Extra jet veto	0.15 ± 0.01	0.05	0.12	0.00	0.42	0.00	0.61 ± 0.15	1
b-jet veto	0.14 ± 0.01	0.05	0.12	0.00	0.24	0.00	0.42 ± 0.15	1
$p_T^{Tot} < 30$ GeV	0.13 ± 0.01	0.04	0.11	0.00	0.14	0.00	0.31 ± 0.12	1
$Z \to \tau\tau$ veto	0.12 ± 0.01	0.04	0.11	0.00	0.08	0.00	0.24 ± 0.11	1
$m_{\ell\ell} < 80$ GeV	0.12 ± 0.01	0.02	0.11	0.00	0.01	0.00	0.15 ± 0.10	1
$\Delta\phi_{\ell\ell} < 1.8$	0.10 ± 0.01	0.01	0.11	0.00	0.01	0.00	0.14 ± 0.10	0
$0.75 \times m_H < m_T < m_H$	0.06 ± 0.01	0.01	0.00	0.00	0.01	0.00	0.02 ± 0.01	0

Table 9.5: The expected number of signal and background events based on MC in the $H + 2j$ analysis for 35 pb^{-1} of integrated luminosity. The signal numbers correspond to the case of $m_H = 170$ GeV. The 'top' refers to $t\bar{t}$ and single top backgrounds. Errors are statistical only and are calculated using the large MC samples listed in Table 4.1 and scaled to the integrated luminosity of the data sample. The ee, $e\mu$ and $\mu\mu$ final states are summed.

Once all cuts have been applied except the m_T cut, there are no events observed in data. This is consistent with the MC expectation of 0.02 ± 0.01 events. Nevertheless, Figure 9.3, which shows the m_T distribution after the cut on $\eta_{j_1} * \eta_{j_2}$ to benefit from improved statistics and the m_T distribution after all other cuts, indicates that the signal to background ratio in the two jet channel is in fact better than both the zero and one jet channels. This channel suffers from the small cross section of the VBF Higgs boson production mechanism hence does not contribute significantly to the calculated Higgs boson limits with the current dataset. However, with a larger dataset in the future, this good signal to background ratio may be exploited and the two jet channel should show an increasing contribution to the search potential of the $H \to WW$ channel.

9.2.4 Summary

The number of events expected using MC for the signal and all of the backgrounds except the W+jets background, which is estimated using the data-driven method detailed in Section 6.3 for the $H + 0j$ and $H + 1j$ channels, is shown in Table 9.6. No excess is observed hence limits on Higgs boson production are set as described in the following section.

9.3 Limits on Higgs boson production

The profile likelihood method [99, 108] is used to set limits on Higgs boson production, as described in detail in Ref. [90]. This method uses the likelihood function, defined in Equation 9.2, as a test statistic. The limit setting procedure performs a hypothesis test between the null hypothesis, H_0, which is the background-only model and the alternative

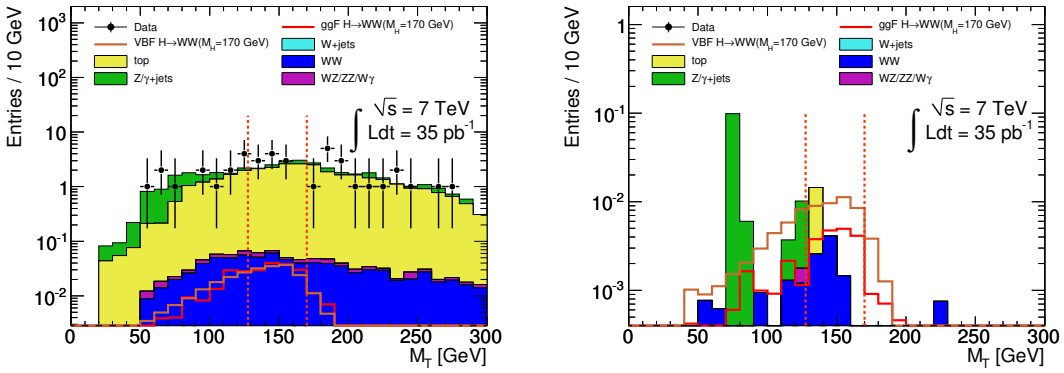

(a) (b)

Figure 9.3: m_T distribution for the two jet channel after the cut on $\eta_{j_1} * \eta_{j_2}$ (a) and after all the cuts except the cut on m_T itself (b). The signal region lies within the dotted lines. ee, $\mu\mu$ and $e\mu$ channels have been combined. Backgrounds have been estimated using MC scaled to an integrated luminosity of 35 pb^{-1}. Errors shown are statistical only.

hypothesis, H_1, which is the signal plus background model. The parameter of interest (the signal cross section) in the model being considered can be determined by maximising this likelihood ratio. To determine the expected limit, this may be performed for a number of pseudo-experiments with the number of signal and background events Poisson fluctuated and for a range of different hypothesized values of the parameter of interest. From this the expected 95% C.L. limit may be extracted.

The $H+0j$, $H+1j$ and $H+2j$ channels are treated as separate analyses and are then combined by multiplying their likelihood functions to give a combined likelihood:

$$L(\mu) = L_{global} \times L_{H+0j}(\mu) \times L_{H+1j}(\mu) \times L_{H+2j}(\mu) \tag{9.1}$$

In this equation, L_{global} constrains the nuisance parameters which model the global systematic uncertainties which affect all channels and are shown in Table 9.1. μ parameterises the signal strength, which is assumed to be the same in each of the jet channels. It is this parameter which the limit setting procedure aims to extract and in this case it is expressed as a ratio of the observed cross section to the expected SM Higgs boson production cross section.

The channel-specific terms in Equation 9.1 constrain the nuisance parameters specific to each jet bin. These terms consist of products of Poissonians for the signal and backgrounds with the extrapolation parameters α and β, as discussed in Section 9.1, constrained by Gaussians.

The likelihood function is maximised twice to calculate the likelihood ratio $\tilde{\lambda}(\mu)$:

$$\tilde{\lambda}(\mu) = \begin{cases} \frac{L(\mu,\hat{\hat{\theta}}(\mu))}{L(\hat{\mu},\hat{\theta})} & \hat{\mu} \geq 0, \\ \frac{L(\mu,\hat{\hat{\theta}}(\mu))}{L(0,\hat{\hat{\theta}}(0))} & \hat{\mu} < 0, \end{cases} \tag{9.2}$$

The first time the likelihood function is maximised, the parameters are allowed to wander freely within their uncertainties and a best fit value of signal strength is extracted,

m_H [GeV]	Jet bin	Signal	Total Bkg.	Observed
120	$H+0j$	0.15	0.87	1
	$H+1j$	0.05	1.05	1
	$H+2j$	0.01	0.00	0
130	$H+0j$	0.34	0.97	2
	$H+1j$	0.13	1.07	1
	$H+2j$	0.03	0.01	0
140	$H+0j$	0.56	1.07	2
	$H+1j$	0.22	1.02	0
	$H+2j$	0.03	0.03	0
150	$H+0j$	0.78	1.12	1
	$H+1j$	0.32	1.03	0
	$H+2j$	0.04	0.03	0
160	$H+0j$	1.11	1.09	1
	$H+1j$	0.50	0.93	0
	$H+2j$	0.06	0.03	0
165	$H+0j$	1.13	1.03	2
	$H+1j$	0.50	0.93	0
	$H+2j$	0.06	0.02	0
170	$H+0j$	1.26	1.70	3
	$H+1j$	0.6	1.26	1
	$H+2j$	0.06	0.02	0
180	$H+0j$	0.85	1.33	3
	$H+1j$	0.42	1.25	1
	$H+2j$	0.05	0.01	0
190	$H+0j$	0.45	0.97	3
	$H+1j$	0.24	1.12	1
	$H+2j$	0.03	0.01	0
200	$H+0j$	0.29	0.72	3
	$H+1j$	0.15	0.85	1
	$H+2j$	0.02	0.01	0

Table 9.6: The expected and observed number of events in 35 pb^{-1} of integrated luminosity for each jet channel for ee, $\mu\mu$ and $e\mu$ channels combined.

$\hat{\mu}$. The second time, the signal strength μ is constrained by $\hat{\mu}$ to give an estimator $\tilde{q}_\mu$:

$$\tilde{q}_\mu = \begin{cases} -2\ln\tilde{\lambda}(\mu) & \hat{\mu} \le \mu \\ 0 & \hat{\mu} > \mu \end{cases} = \begin{cases} -2\ln\frac{L(\mu,\hat{\hat{\theta}}(\mu))}{L(0,\hat{\hat{\theta}}(0))} & \hat{\mu} < 0, \\ -2\ln\frac{L(\mu,\hat{\hat{\theta}}(\mu))}{L(\hat{\mu},\hat{\theta})} & 0 \le \hat{\mu} \le \mu, \\ 0 & \hat{\mu} > \mu. \end{cases} \tag{9.3}$$

In the above equation, $\hat{\theta}$ represents the preferred set of nuisance parameters extracted from the first fit, with $\hat{\hat{\theta}}$ repesenting the same quantity but from the second fit.

Assuming a signal strength of μ, the PDF $f(\tilde{q_\mu}|\mu, \theta(\hat{\hat{\mu}}))$ is constructed using toy MC. The p-value, which expresses the likelihood that a given test statistic is at least as extreme

as the observed test statistic under the assumption that the null hypothesis is true (and the Higgs boson does not exist), is calculated. For example, if the Higgs boson did exist, a small p-value would indicate that it was extremely unlikely that the observed number of events was consistent with the SM. In this case, the p-value for signal strength μ is given by:

$$p_\mu = \int_{\tilde{q}_{\mu,obs}}^{\infty} f(\tilde{q}_\mu|\mu, \hat{\hat{\theta}}(\mu))\, \mathrm{d}\tilde{\mathrm{q}}_\mu \tag{9.4}$$

To obtain a 95% C.L., iterations are performed with an assumed signal strength of μ to obtain $p_{\mu_{up}} \leq 5\%$ to give a value of μ_{up}. The expected median, μ_{med}, is extracted in a similar fashion using background-only toy MC. The $\pm 1\sigma$ and $\pm 2\sigma$ bands can also be obtained this way. There is a chance that the null hypothesis may be wrongly excluded in cases where the expected and observed number of events is very small and statistical fluctuations could have a large effect. To avoid this, if the observed limit fluctuates beneath the $\mu_{med} - 1\sigma$ band, the quoted limit is given as $\mu_{med} - 1\sigma$ instead of the observed smaller value. This is known as a Power Constrained Limit (PCL) [109].

Figure 9.4 shows the expected and observed limits on the Higgs boson production cross section obtained by the ATLAS experiment with 35 pb^{-1} of data using the $H \to WW$ decay mode. A SM-like Higgs boson of mass $m_H = 160$ GeV with a cross section of 1.2 times the SM value is excluded at 95% C.L.

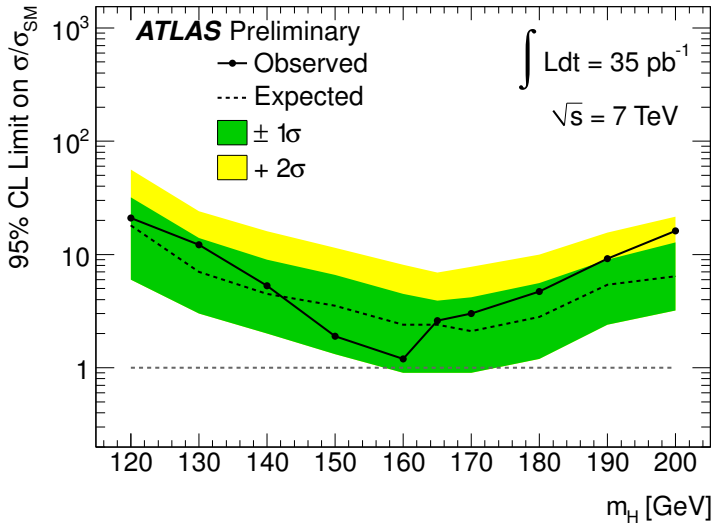

Figure 9.4: The expected signal cross section as a ratio of the SM-only cross section which is excluded at 95% C.L. in the $H \to WW$ channel using 35 pb^{-1} of integrated luminosity and a combination of the $H + 0j$, $H + 1j$ and $H + 2j$ channels.

Results from the Tevatron [110, 111] using the CL$_S$ method [112] are overlaid with the obtained ATLAS results and shown in Figure 9.5. ATLAS limits are also shown in this figure as calculated using the CL$_S$ method with asymptotic approximations [99]. This comparison shows that even with such a small dataset, the ATLAS limit closely approaches the Tevatron limit, which was obtained using 5.9 fb^{-1} and a combination of all Higgs boson search channels. Thus, with more data it is clear that if the Higgs boson

does not exist, the limits obtained with ATLAS will quickly eclipse the Tevatron's results in the mid to high Higgs boson mass range (from $\sim$ 130 GeV upwards). Similarly, this translates in the ability to rapidly discover the Higgs boson if it does exist. To extend the sensitivity to the low mass range will need much more data as well as improvements in the analysis itself, such as lowering lepton p_T thresholds to increase the acceptance for low mass Higgs boson events which will produce soft leptons.

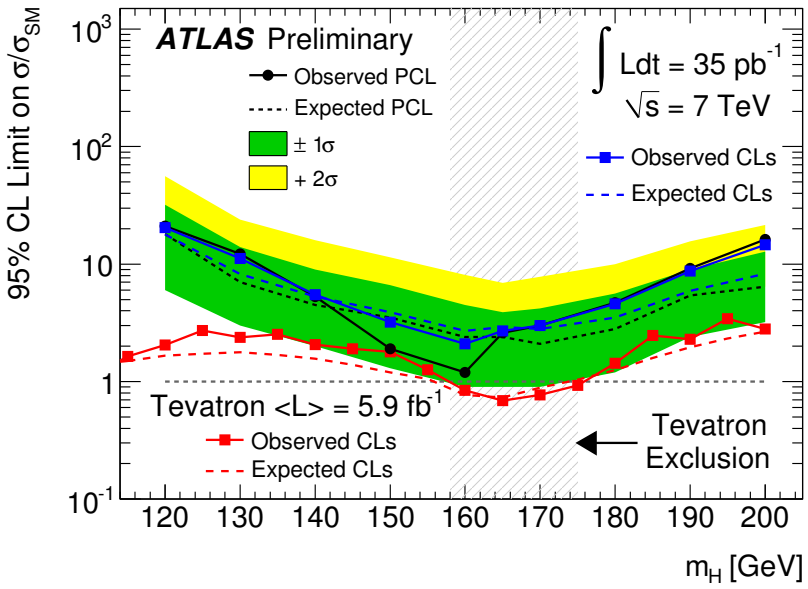

Figure 9.5: The expected signal cross section as a ratio of the SM-only cross section which is excluded at 95% C.L. in the $H \rightarrow WW$ channel using 35 pb^{-1} of integrated luminosity and a combination of the $H+0j$, $H+1j$ and $H+2j$ channels. A comparison is shown with the Tevatron limits, calculated using the CL$_S$ method. The ATLAS limits as calculated using both the PCL method and the CL_S method are shown.

Chapter 10

$H \rightarrow WW$ search results using the matrix element discriminant

Results obtained using the matrix element discriminant, which is discussed in detail in Chapter 7, are presented in this chapter. A discussion of possible sources of systematic uncertainty is provided in Section 10.1, the results obtained with the matrix element method are shown in Section 10.2 and the final limits on Higgs boson production are given in Section 10.3

10.1 Systematics

Various source of systematic uncertainty are considered. These sources are:

- **JES**: The jet energy scale is varied by $\pm 1\sigma$ to estimate the effect of this uncertainty.
- **JER**: To determine the effect of the jet energy resolution, the jet energies are smeared according to a Gaussian.
- **Electron reconstruction and identification efficiency**: This is known to differ in data and MC, and a p_T and η dependent scale factor is applied to MC to correct for this, as described in Section 5.3.1. This scale factor has an associated uncertainty, thus the uncertainty associated with the electron reconstruction and identification efficiency is determined by adding and subtracting the uncertainty to the scale factor.
- **Electron resolution**: The electron resolution uncertainty is determined in the same way the JER is determined.
- **Muon reconstruction and identification efficiency**: This is calculated in the same manner as the electron reconstruction and identification efficiency uncertainty is determined.
- **Muon resolution**: This is determined in the same way as for the jets and electrons.
- **Missing** E_T: The uncertainty on the missing E_T is estimated by propagating the object uncertainties through to the missing E_T calculation, giving an uncertainty of up to 20%.

- **Luminosity**: This uncertainty is calculated to be 11% using van der Meer scans [24].

The magnitude of these uncertainties can be seen in Table 9.1.

The p_T distributions of the leading and subleading electrons using the nominal event selection and after varying the electron reconstruction and identification efficiency scale factor and the electron resolution are shown in Figure 10.1. This figure indicates that the reconstruction and identification efficiency uncertainty is the dominant source of uncertainty affecting electrons.

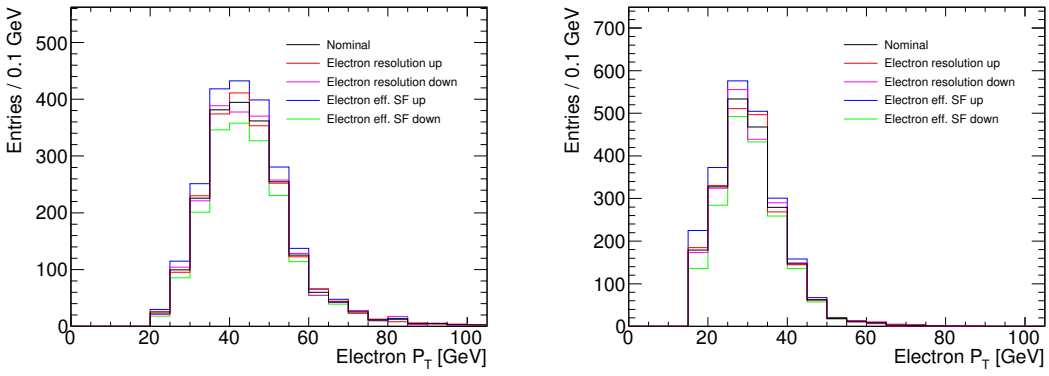

(a) (b)

Figure 10.1: Leading (a) and subleading (b) electron p_T distributions for Higgs boson events in the ee channel in MC for the nominal case, after allowing the electron p_T to vary within its allowed resolution and after varying the electron efficiency scale factor by $\pm 1\sigma$ using a Higgs boson sample with $m_H = 170$ GeV.

Figure 10.2 shows the p_T distributions of leading and subleading muons once the muon reconstruction and identification efficiency and muon resolution are varied as well as the nominal p_T distributions. This figure indicates that the uncertainties are smaller for muons than electrons. This is to be expected since the intrinsic detector resolution for muons is better than that for electrons, as can be seen in Figure 7.9. As in the electron case, the dominant uncertainty for muons is that arising from the reconstruction and identification efficiency.

The p_T distributions for leading and subleading jets are shown in Figure 10.3 with the variations in JES and JER shown as well as the nominal distributions. This figure also shows the jet multiplicity distribution with these uncertainties applied. The JES uncertainty has the largest effect, causing migration between the various jet bins. Since only the lepton kinematics are used as an input to the matrix element calculation, these jet uncertainties propagate through to an overall normalisation systematic and do not affect the shape of the matrix element likelihood distribution.

After applying the electron and muon uncertainties, the matrix element distribution is shown in Figure 10.4. These uncertainties do not significantly alter the shape of the matrix element likelihood distribution, indicating that the method is robust even once uncertainties have been accounted for.

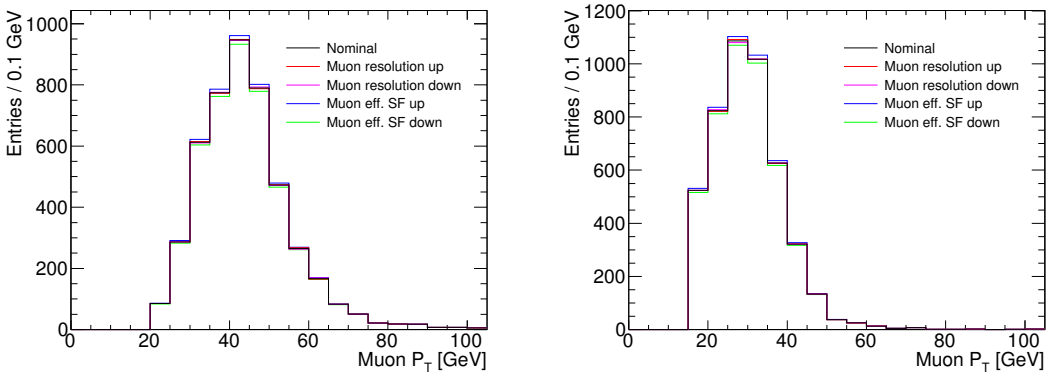

(a) (b)

Figure 10.2: Leading (a) and subleading (b) muon p_T distributions for Higgs boson events in the $\mu\mu$ channel in MC for the nominal case, after allowing the muon p_T to vary within its allowed resolution and after varying the muon efficiency scale factor by $\pm 1\sigma$ using a Higgs boson sample with $m_H = 170$ GeV.

10.2 Results

The expected number of events in the ee, $\mu\mu$ and $e\mu$ channels after the preselection described in Chapter 4 are given in Tables 10.1, 10.2 and 10.3 respectively. These tables indicate that the agreement between data and MC is good in all channels, with no significant discrepancies observed.

Selection	Signal	WW	W+jets	Z+jets	top	Other	Total Bkg.	Observed
Opposite charge dileptons	0.86	4.35	1.22	5879	21.47	4.88	5911	6212
$M_{ll} > 15$ GeV	0.83	4.31	1.22	5866	21.28	4.85	5897	6174
$\lvert M_{ll} - M_Z \rvert > 15$ GeV	0.77	3.40	1.09	592.3	16.93	0.55	614.3	696
$E^{miss}_{T,Rel} > 25$ GeV	0.64	2.09	0.67	2.59	9.68	0.22	15.25	24
0 jet	0.37 ± 0.01	1.48	0.45	1.45	0.20	0.09	3.68 ± 0.33	6
$E^{miss}_{T,Rel} > 40$ GeV	0.32 ± 0.01	0.98	0.00	0.00	0.20	0.03	1.21 ± 0.09	3
1 jet	0.18 ± 0.01	0.42	0.15	0.37	1.92	0.10	3.02 ± 0.36	2
≥ 2 jet	0.09 ± 0.004	0.18	0.07	0.70	7.13	0.03	8.11 ± 0.50	16

Table 10.1: The expected number of signal and background events in the ee channel for 35 pb^{-1} of integrated luminosity for a Higgs boson signal sample with $m_H = 170$ GeV. The signal and all backgrounds are estimated using MC only. Errors are statistical only.

The expected number of signal events for all hypothesized Higgs boson masses, from $120 < m_H < 200$ GeV, and all backgrounds after the preselection in the 0 jet channel, with the requirement of $\not\!\!E_T^{\rm Rel} > 40$ GeV, is given in Table 10.4 for the ee, $\mu\mu$ and $e\mu$ channels as well as all lepton channels combined. This table also gives the observed number of events in each of these channels.

After applying a loose preselection, with $\not\!\!E_T^{\rm Rel} > 25$ GeV, the matrix element likelihood distributions are given in Figure 10.5 for all jet channels combined, the zero jet channel, the one jet channel and the two jet channel (which consists of events with two or more jets). These distributions are shown for MC only, with a Higgs boson signal mass of 170 GeV. Good separation between the Higgs boson signal and the SM WW background

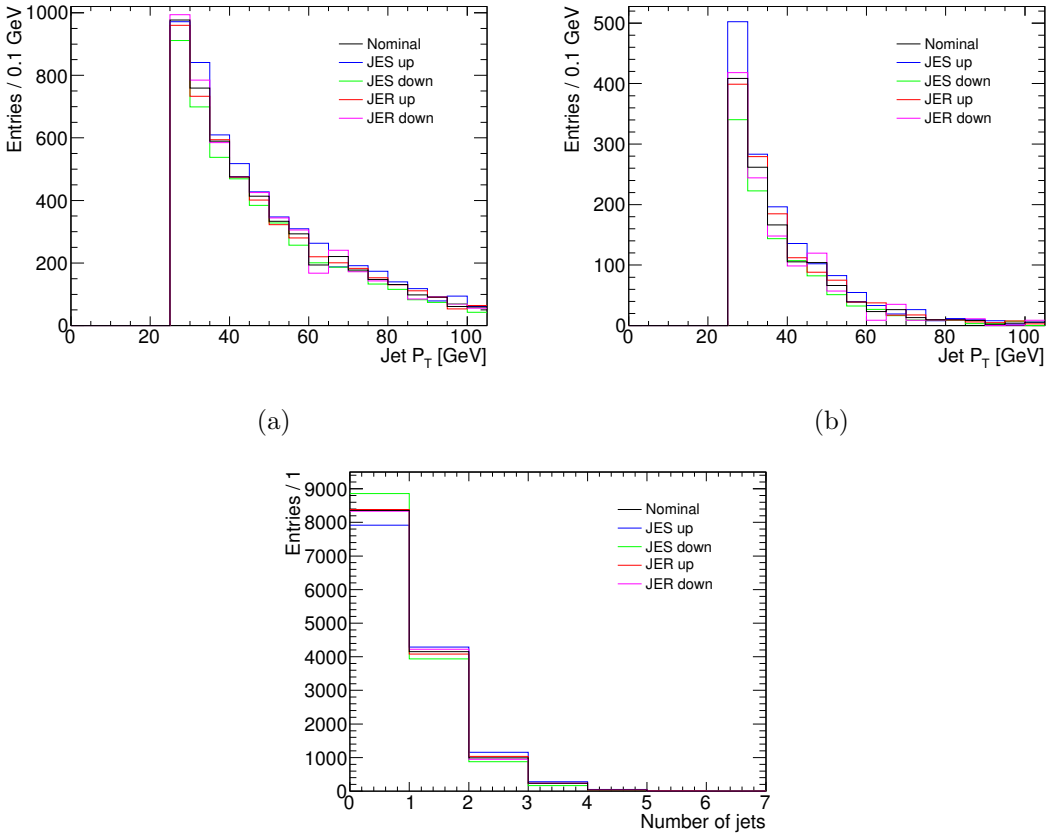

Figure 10.3: Leading (a) and subleading (b) jet p_T distributions and jet multiplicity distribution (c) for Higgs boson events in MC in all channels for the nominal case, after allowing the jet p_T to vary within its allowed resolution and after varying the jet energy scale by $\pm 1\sigma$ using a Higgs boson sample with $m_H = 170$ GeV.

Selection	Signal	WW	W+jets	Z+jets	top	Other	Total Bkg.	Observed
Opposite charge dileptons	2.02	9.96	0.73	1.377e+04	47.00	9.63	1.384e+04	1.362e+04
$M_{ll} > 15$ GeV	1.93	9.86	0.73	1.372e+04	46.44	9.62	1.379e+04	1.351e+04
$\lvert M_{ll} - M_Z \rvert > 15$ GeV	1.77	7.72	0.53	1735	36.51	0.45	1781	1730
$E_{T,Rel}^{miss} > 25$ GeV	1.47	4.93	0.31	8.99	20.86	0.19	35.29	24
0 jet	0.83 ± 0.01	3.40	0.17	6.26	0.45	0.11	10.39 ± 0.67	9
$E_{T,Rel}^{miss} > 40$ GeV	0.73 ± 0.01	2.31	0.00	0.01	0.24	0.12	2.69 ± 0.11	3
1 jet	0.44 ± 0.01	1.14	0.14	1.76	4.33	0.05	7.43 ± 0.53	5
≥ 2 jet	0.19 ± 0.01	0.39	0.00	0.96	14.73	0.04	16.12 ± 0.71	10

Table 10.2: The expected number of signal and background events in the $\mu\mu$ channel for 35 pb^{-1} of integrated luminosity for a Higgs boson signal sample with $m_H = 170$ GeV. The signal and all backgrounds are estimated using MC only. Errors are statistical only.

is observed in all jet bins. The background composition changes noticeably between the jet bins. The dominant background to zero jet events arises from Z and SM WW processes, while, as the number of jets increases, the top background becomes increasingly significant and actually overwhelms all other backgrounds in the two jet bin.

The matrix element likelihood is designed specifically to separate Higgs boson events

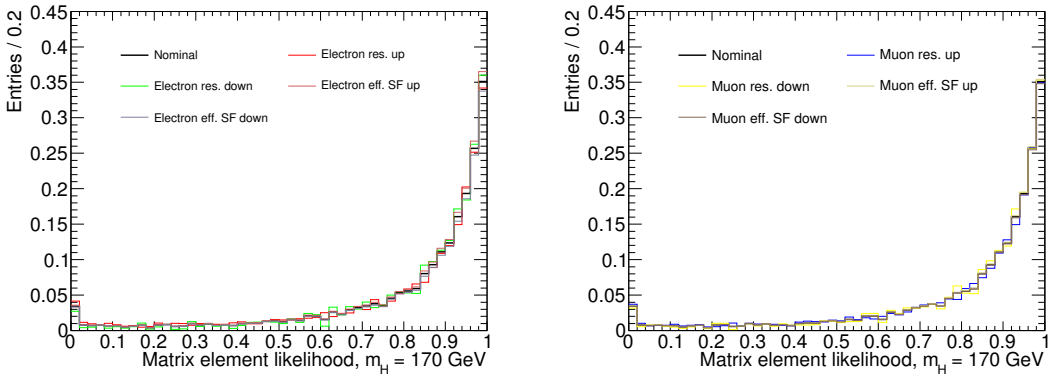

(a) (b)

Figure 10.4: Matrix element likelihood distributions in MC with systematic uncertainties related to electrons (a) and muons (b) after performing the integration for a Higgs boson sample with $m_H = 170$ GeV.

Selection	Signal	WW	W+jets	Z+jets	top	Other	Total Bkg.	Observed
Opposite charge dileptons	2.70	13.18	3.21	59.12	62.18	1.21	138.9	160
$E_{T,Rel}^{miss} > 25$ GeV	2.22	8.35	1.79	0.42	35.62	0.54	46.71	52
0 jet	1.25 ± 2	5.83	1.14	0	0.84	0.32	8.12 ± 0.46	7
$E_{T,Rel}^{miss} > 40$ GeV	1.08 ± 0.02	3.98	0.60	0.00	0.73	0.13	5.43 ± 0.35	5
1 jet	0.66 ± 0.01	1.87	0.36	0.27	6.76	0.15	9.41 ± 0.53	13
$\geq$ 2 jet	0.31 ± 0.01	0.65	0.29	0.15	26.61	0.06	27.75 ± 0.88	32

Table 10.3: The expected number of signal and background events in the $e\mu$ channel for 35 pb^{-1} of integrated luminosity for a Higgs boson signal sample with $m_H = 170$ GeV. The signal and all backgrounds are estimated using MC only. Errors are statistical only.

Channel	$m_H = 120$	$m_H = 130$	$m_H = 140$	$m_H = 150$	$m_H = 160$	$m_H = 165$
ee	0.03 ± 0.002	0.08 ± 0.002	0.16 ± 0.01	0.23 ± 0.01	0.33 ± 0.01	0.34 ± 0.01
$\mu\mu$	0.09 ± 0.003	0.23 ± 0.004	0.42 ± 0.01	0.59 ± 0.01	0.78 ± 0.01	0.82 ± 0.02
$e\mu$	0.11 ± 0.003	0.30 ± 0.004	0.55 ± 0.01	0.84 ± 0.02	1.15 ± 0.01	1.15 ± 0.02
All	0.22 ± 0.005	0.62 ± 0.01	1.13 ± 0.02	1.66 ± 0.02	2.26 ± 0.01	2.32 ± 0.03
Channel	$m_H = 170$	$m_H = 180$	$m_H = 190$	$m_H = 200$	Bkg.	Data
ee	0.32 ± 0.01	0.24 ± 0.01	0.16 ± 0.01	0.13 ± 0.00	1.21 ± 0.09	3
$\mu\mu$	0.73 ± 0.01	0.58 ± 0.01	0.36 ± 0.01	0.28 ± 0.01	2.69 ± 0.11	3
$e\mu$	1.08 ± 0.02	0.90 ± 0.01	0.64 ± 0.01	0.52 ± 0.01	5.43 ± 0.35	5
All	2.13 ± 0.02	1.73 ± 0.02	1.16 ± 0.01	0.92 ± 0.01	9.33 ± 0.38	11

Table 10.4: Signal, background and data yields in the zero jet channel after preselection for 35 pb^{-1} of integrated luminosity. ggF and VBF processes are combined.

from SM WW events; it makes no attempt to discriminate between the Higgs boson signal and other background processes. In the one and two jet cases, the top background is large so additional selection must be applied to reduce it to an acceptable level. One way in which top events may be distinguished from signal events is the presence of b-jets. When the top quark decays, it has an almost 100% branching ratio to b quarks, which hadronise and form b-jets. When events containing b-jets are removed from the one and two jet

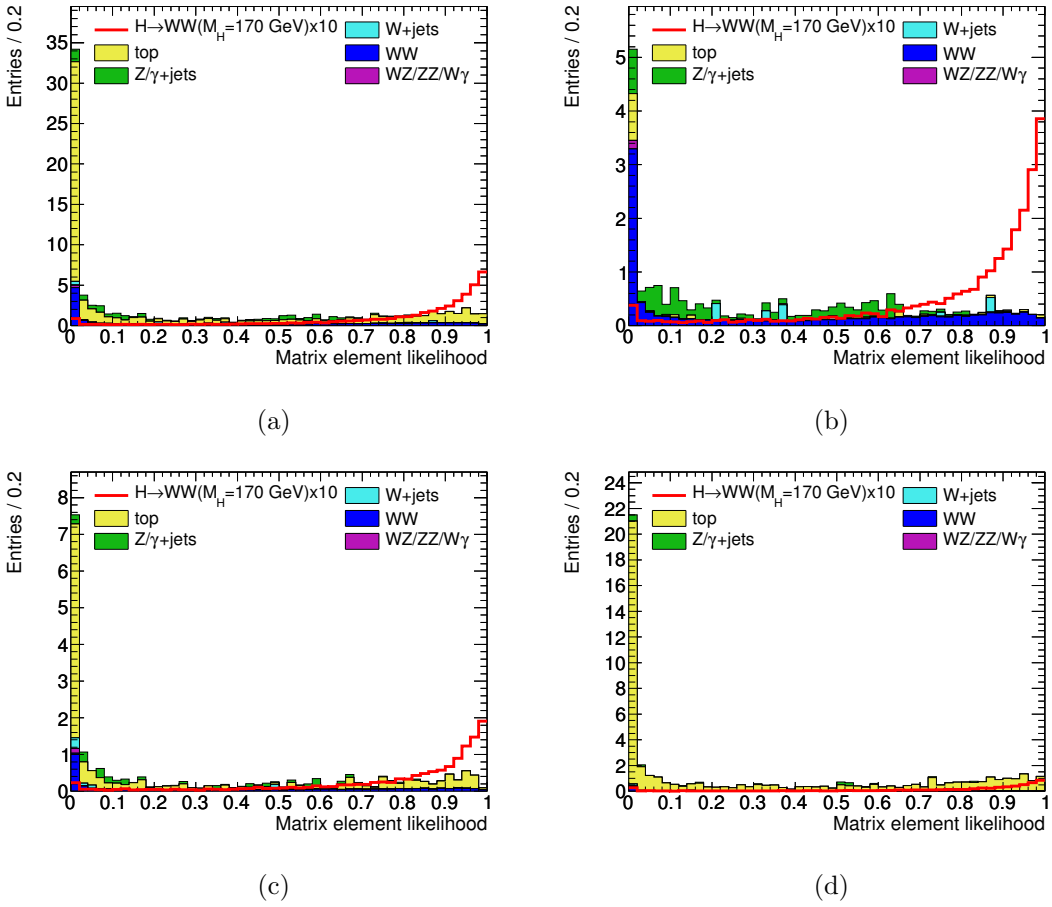

Figure 10.5: Matrix element likelihood distributions with a hypothesized Higgs boson mass of 170 GeV and a $m_H = 170$ GeV Higgs boson sample for all jet channels combined (a), the zero jet channel (b), the one jet channel (c) and the two jet channel (d) after requiring $\not\!\!E_T^{\mathrm{Rel}} > 25$ GeV.

channels, a significant reduction in the top background is achieved. This may be seen in Figure 10.6 for a Higgs boson sample with $m_H = 170$ GeV using MC only.

The zero jet channel suffers from some contamination from the Z background, which has a large cross section and is not entirely removed by the requirement of $\not\!\!E_T^{\mathrm{Rel}} > 25$ GeV. To further reduce the Z background, this selection is tightened to $\not\!\!E_T^{\mathrm{Rel}} > 40$ GeV. Once this is applied, the matrix element likelihood dsitributions show good separation from background, which is now dominated by SM WW production. This separation is seen at all hypothesized Higgs boson masses, as is shown in Figure 10.7, which uses MC only. This figure shows that at low Higgs boson mass, there is a non-neligible contribution from the W+jets background in the signal region. This may be accounted for in future analyses by including a W+jets matrix element in the discriminant, as has been done previously at CDF [92]. This should improve the separation for these low hypothesized Higgs boson mass cases, reducing the contamination from the W+jets background.

The final step is to include data. This is shown in Figure 10.8 for the zero jet channel for all hypothesized Higgs boson masses, with the requirement of $\not\!\!E_T^{\mathrm{Rel}} > 40$ GeV applied. These distributions show good agreement between data and the background MC, within

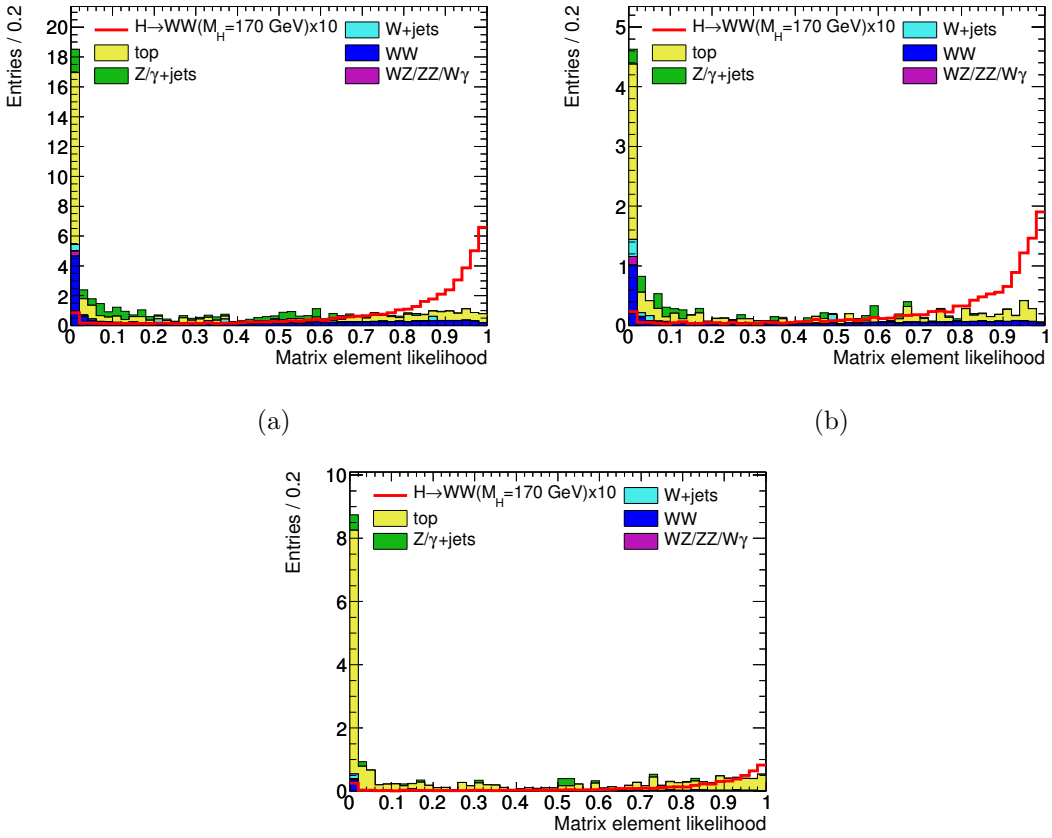

Figure 10.6: Matrix element likelihood distributions with a hypothesized Higgs boson mass of 170 GeV and a $m_H = 170$ GeV Higgs boson sample for all jet channels combined (a), the one jet channel (b) and the two jet channel (c) after requiring $\not\!\!E_T^{\mathrm{Rel}} > 25$ GeV and vetoing events containing b-jets.

the limited statistics, with no obvious excesses, suggesting that it is appropriate to set limits on Higgs boson production. Due to the low statistics, it is quite difficult to determine how compatible the data and MC are. One way to allow sparse distributions, such as these, to be compared is the use of integral distributions. However, once the dataset increases, these difficulties in comparing data and MC will be reduced.

A comparison between the sensitivity obtained using the cut-based analysis described in Chapter 9 and the matrix element discriminant can be obtained using the significance, defined as [99]:

$$S = \sqrt{2[(N_S + N_B)\ln(1 + \frac{N_S}{N_B}) - N_S]} \tag{10.1}$$

For the zero jet channel this is shown in Table 10.5, where the selection applied to the matrix element likelihood distribution has been optimised using MC to obtain the best significance. This indicates that the matrix element discriminant gives a noticeable improvement with respect to the cut-based analysis at all hypothesized Higgs boson masses except $m_H = 120$ GeV and $m_H = 130$ GeV. No improvement is seen at these masses due

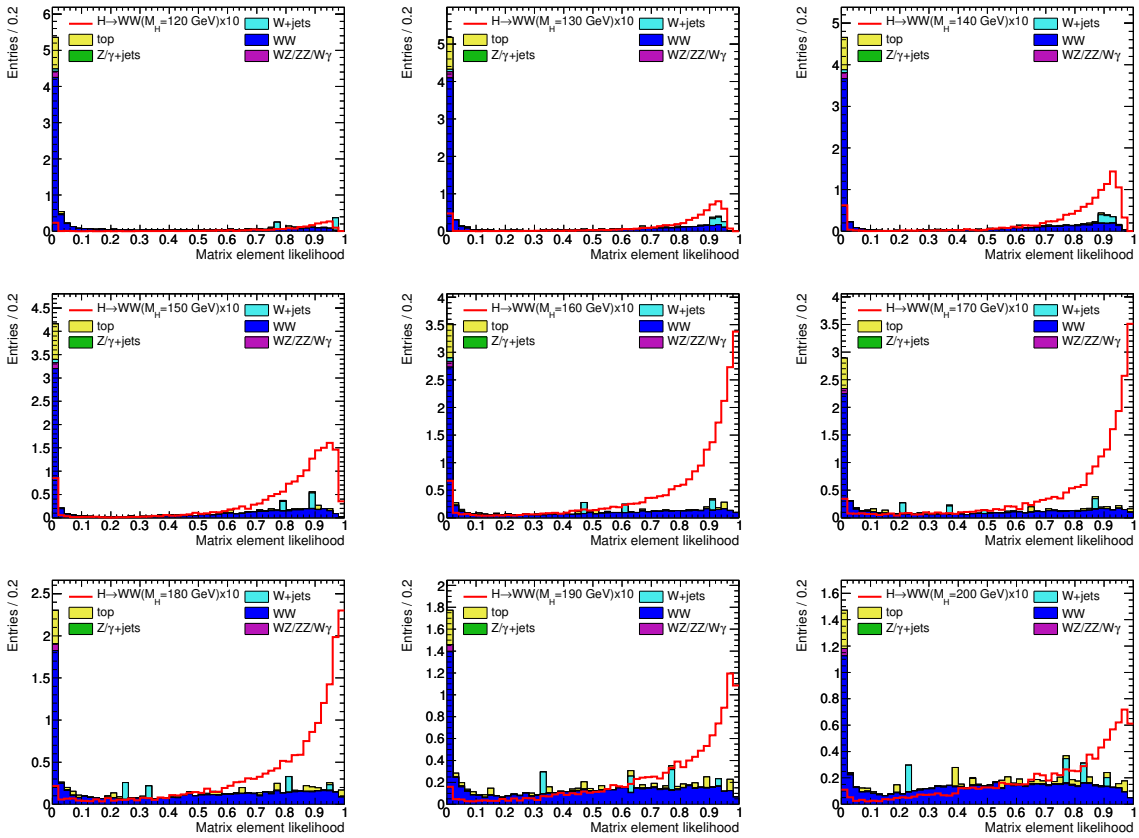

Figure 10.7: Matrix element likelihood distributions with hypothesized Higgs boson mass of 120, 130, 140, 150, 160, 170, 180, 190 and 200 GeV in the zero jet channel after requiring $\not\!\!E_T^{\mathrm{Rel}} > 40$ GeV using MC only.

to the contribution from the W+jets background. This has been discussed previously, and separation between Higgs boson signal and W+jets background is something that may be added to future analyses to gain some additional improvement in significance at these low Higgs boson masses.

A comparison between the significance using the matrix element method and the cut-based search in the one and two jet channels has also been performed. For these channels, the matrix element discriminant does not perform as well hence the one and two jet channels are not used at this stage. This is due to the large top background, which must be dealt with separately. This needs further study but, in the future, the top background may be reduced by the application of additional cuts in these channels, or potentially by the inclusion of a top matrix element in the discriminant.

The expected number of signal and background events taken from MC as well as the number of observed events in data is shown in Table 10.6. This shows that, for many cases, the additional sensitivity achieved by the matrix element method is gained by using a loose preselection in combination with the matrix element likelihood which allows more signal events to be retained, whereas the cut-based method requires tighter cuts to achieve good significance. Note that there may be common events between the two methods, since the selections applied are not mutually exclusive.

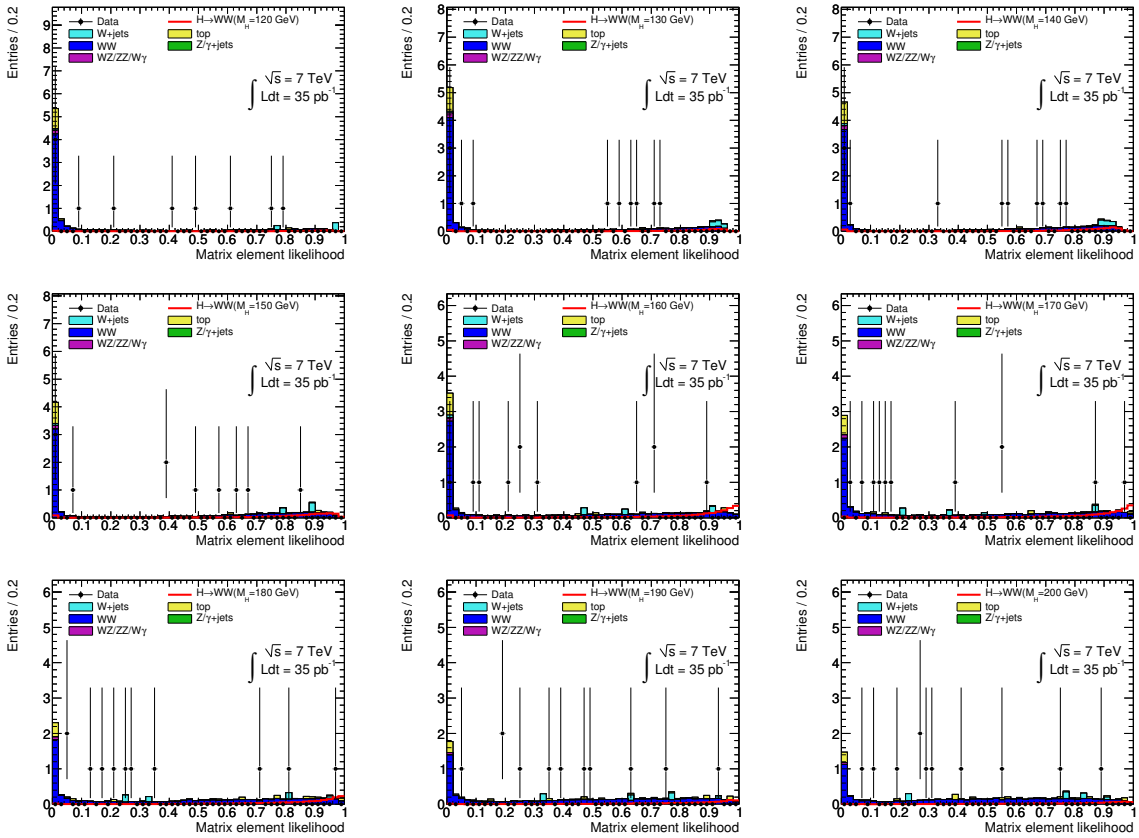

Figure 10.8: Matrix element likelihood distributions with hypothesized Higgs boson mass of 120, 130, 140, 150, 160, 170, 180, 190 and 200 GeV in the zero jet channel after requiring $\not\!\!E_T^{\mathrm{Rel}} > 40$ GeV using MC and data.

These numbers show good agreement between the number of events expected using the background-only hypothesis and the number observed in data. Therefore, the next section discusses the limits which may be set on Higgs boson production at ATLAS.

10.3 Limits on Higgs boson production

The profile likelihood method with a power constraint, described in Section 9.3, is used to set limits on Higgs boson production. Only the zero jet channel is used, with the ee, $\mu\mu$ and $e\mu$ channels combined to give a single channel for simplicity. Instead of performing a number counting experiment, the matrix element likelihood distributions as shown in Figure 10.8 are used as inputs to the limit setting procedure to exploit shape differences between signal and backgrounds. This is performed using the RooStats package [113]. The matrix element likelihood distributions with the lepton efficiency uncertainties and the lepton resolution uncertainties varied are used as systematic uncertainties. The luminosity, JES and JER uncertainties are treated as overall uncertainties in the normalisation. For all the uncertainties, the signal and background are assumed to move in a correlated way during the limit setting procedure.

A comparison between the expected and observed limits on Higgs boson production

Higgs mass [GeV]	Cut-based significance	Matrix element significance	% increase
120	0.156	0.151	-3.72
130	0.328	0.312	-4.63
140	0.502	0.515	2.64
150	0.670	0.714	6.56
160	0.933	1.054	13.0
165	0.969	1.114	14.9
170	0.873	1.013	16.0
180	0.674	0.754	11.8
190	0.427	0.485	13.6
200	0.326	0.356	9.23

Table 10.5: A comparison of the significance achieved using the cut-based method described in Chapter 9 and the matrix element method described in this chapter for the zero jet channel. The percentage increase in significance of the matrix element likelihood method with respect to the cut-based analysis is also shown.

	Cut-based analysis			Matrix element analysis			
m_H [GeV]	N_S	N_{Bg}	Data	Cut value	N_S	N_{Bg}	Data
120	0.15	0.87	1	$0.86 < \text{LH} < 0.96$	0.12	0.55	1
130	0.34	0.97	2	$\text{LH} > 0.72$	0.48	2.24	2
140	0.56	1.07	2	$\text{LH} > 0.64$	0.97	3.22	4
150	0.78	1.12	1	$\text{LH} > 0.64$	1.42	3.51	3
160	1.11	1.09	1	$\text{LH} > 0.78$	1.67	2.02	0
165	1.13	1.03	2	$\text{LH} > 0.92$	1.24	0.89	1
170	1.26	1.70	3	$\text{LH} > 0.90$	1.20	1.05	1
180	0.85	1.33	3	$\text{LH} > 0.84$	1.07	1.67	1
190	0.45	0.97	3	$\text{LH} > 0.80$	0.71	1.93	1
200	0.29	0.70	3	$\text{LH} > 0.86$	0.42	1.23	1

Table 10.6: A comparison of the expected number of signal and background events from MC and the observed number of data events using the cut-based method described in Chapter 9 and the matrix element method described in this chapter. The cuts applied to the matrix element likelihood, LH, are given for each Higgs boson mass point.

using the cut-based method with the zero, one and two jet channels combined and the matrix element discriminant in the zero jet channel only are shown in Table 10.7. This comparison shows that the matrix element method achieves better expected limits at all Higgs boson masses, despite only using the zero jet channel. This is due not only to the additional separation achieved with the likelihood distribution, which is expected from the comparison given in Table 10.5, but also due to the shape difference between the signal and background which is not exploited at all in the cut-based analysis.

The expected and observed limits on Higgs boson production using a dataset of 35 pb^{-1} as a ratio of the SM-only cross section are shown in Figure 10.9. Figure 10.10 shows the same limits, with the limits obtained using the cut-based method overlaid to show the improvement achieved by using the matrix element discriminant. This figure shows that the observed limits using the matrix-element-based discriminant are worse than the observed

	Cut-based					Matrix-element-based				
m_H [GeV]	Observed	Median	$+1\sigma$	-1σ	$+2\sigma$	Observed	Median	$+1\sigma$	-1σ	$+2\sigma$
120	21.0	18.0	32.0	6.0	56.0	30.5	15.8	29.8	4.6	45.2
130	12.2	7.0	14.0	3.0	24.0	8.8	6.1	11.1	1.9	17.6
140	5.3	4.5	9.0	2.0	16.0	4.8	3.7	7.1	1.6	11.2
150	1.9	3.5	6.6	1.3	11.4	3.2	2.8	4.8	0.8	7.1
160	1.2	2.4	4.5	0.90	8.1	2.2	1.5	2.8	0.5	4.5
165	2.6	2.4	3.9	0.90	6.9	2.8	1.5	2.8	0.5	4.5
170	3.0	2.1	4.2	0.90	7.8	2.5	1.8	3.5	0.8	5.8
180	4.7	2.8	5.6	1.2	10.0	2.8	2.5	4.5	0.8	6.5
190	9.2	5.4	9.0	2.4	15.6	4.3	3.1	7.1	1.1	11.6
200	16.2	6.4	12.8	3.2	21.6	6.3	5.1	8.6	1.1	15.1

Table 10.7: The 95% C.L. upper limit on the expected signal rate, as a multiple of the SM rate, in the $H \to WW$ channel with 35 pb^{-1} of integrated luminosity using the cut-based method described in Chapter 9 in the 0, 1 and 2 jet channels and the matrix element method described in this chapter in the 0 jet channel only.

limits using the cut-based method, despite the expected limits being better. The events selected in the cut-based method are a subset of those obtained in the matrix element method, which uses a much looser selection. At the stage at which the matrix element events are selected, the MC appears to underestimate the data so it is not surprising that the observed limit is worse than the expected limit. However, once all the additional cuts have been applied in the cut-based method, there are some Higgs boson mass points at which the MC underestimates data and some at which it overestimates data. The number of expected and observed events after all the cut-based selection has been applied is also very small (≤ 3 events), therefore a fluctuation by even one event causes the observed limit in the cut-based case to move noticeably with respect to the expected limit. This combination of factors leads to the observed and expected limits shown in Figure 10.10.

It is important to bear in mind the fact that the cut-based limits utilise all three jet channels. While the zero jet channel contributes the most, there is a significant contribution to the sensitivity coming from the one jet channel as well as a small contribution from the two jet channel. The expected limit using the matrix element discriminant in the zero jet channel alone is better than the expected limit using all three jet channels with the cut-based method, therefore, once the one and two jet channels are included in the matrix element limit, a further improvement in sensitivity is to be expected.

A further way in which additional sensitivity may be achieved is by using the matrix element likelihood as an input to a boosted decision tree or neural network. Previous studies [93] suggest that the matrix element likelihood is the most sensitive variable when used as an input to a neural network. This study also indicates that the neural network with the matrix element likelihood as an input gives an improvement in sensitivity with respect to the matrix element discriminant alone, indicating that this may be the best way of maximising the sensitivity in the future.

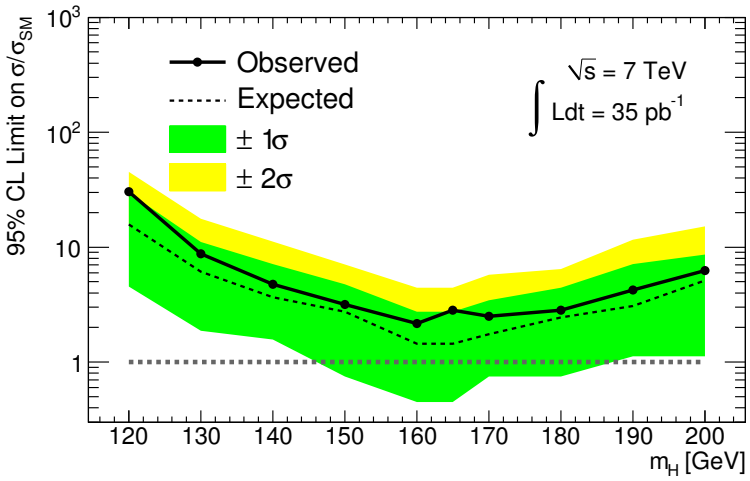

Figure 10.9: The expected signal cross section as a ratio of the SM-only cross section which is excluded at 95% C.L. in the $H \rightarrow WW$ channel using 35 pb^{-1} of integrated luminosity using the matrix element discriminant in the zero jet channel only.

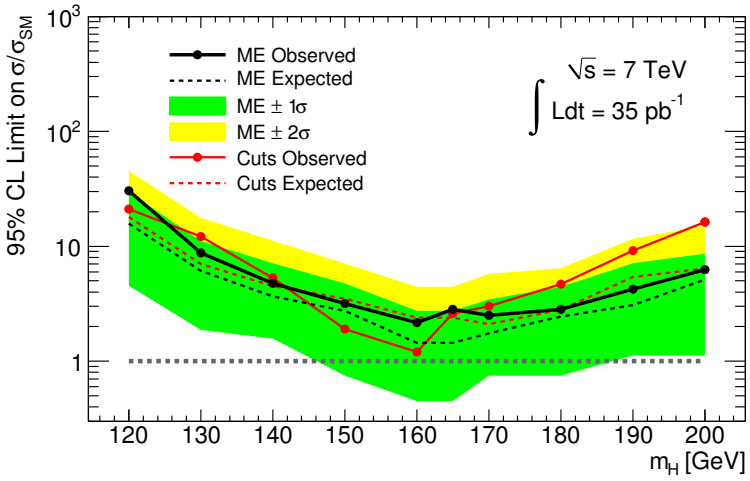

Figure 10.10: The expected signal cross section as a ratio of the SM-only cross section which is excluded at 95% C.L. in the $H \rightarrow WW$ channel using 35 pb^{-1} of integrated luminosity using the matrix element discriminant in the zero jet channel only. The results obtained using the zero, one and two jet channels with the cut-based method are overlaid in red.

Chapter 11

Conclusions and outlook

The current model of particle physics, the SM, requires some mechanism to generate the observed particle masses. The Higgs mechanism is one way in which these masses could be generated. This mechanism would give rise to observable Higgs bosons, which may be discovered at the LHC if they exist.

Precision data suggests that the SM Higgs boson should lie in a mass region accessible to the LHC. Fits to data indicate that the Higgs boson is likely to have a mass of $\mathcal{O}(10^3)$ GeV. In the mass region $m_H > 130$, the branching ratio to pairs of W bosons is expected to dominate, making this a particularly sensitive search channel. In this thesis, a search for the Higgs boson in the $H \to WW \to \ell\nu\ell\nu$ channel has been performed as well as a measurement of the SM WW cross section, which is the dominant background to this process.

The precise measurement of the SM WW cross section measurement is also interesting since some new physics models would give rise to an enhanced WW production cross section, with anomalous triple gauge couplings not observed in the SM. Thus, any deviation of the WW cross section from the SM expectation would give a strong hint of new physics.

This measurement, using 35 pb^{-1} of pp data, collected by the ATLAS detector at the LHC at a centre of mass energy of 7 TeV, gives a WW cross section of $\sigma_{WW} = 40^{+20}_{-16}$(stat.) ± 7(syst.) pb. This is in agreement with the NLO SM prediction of 46 ± 3 pb. This measurement is completely dominant by the statistical uncertainty, which amounts to 44%. Future analyses will benefit from a larger dataset, even if it is not possible to reduce the systematic uncertainties.

In the future, it would be desirable to perform a dedicated search for anomalous triple gauge couplings in addition to a more precise measurement of the WW cross section. This should allow stringent limits to be placed on certain new physics models.

The search for the Higgs boson has been performed using a cut-based method and a matrix element discriminant, with the analysis split into three different jet multiplicity channels: zero, one and at least two jets. The cut-based method uses a combination of all three jet channels, while the matrix element method utilises only the zero jet channel. Despite this, the matrix element discriminant provides an improvement in the expected limit on the Higgs boson production cross section across the full range of Higgs boson masses investigated, from $120 < m_H < 200$ GeV.

Using the cut-based method, a Higgs boson with $m_H = 160$ GeV with a production

rate of 1.2 times the SM value has been excluded at 95% C.L. using a power constrained limit technique with a combination of the zero, one and two jet channels. The matrix element discriminant has a better expected limit than the cut-based method, however, due to fluctuations in the data the observed exclusion limit is not as strong. The matrix element method excludes a Higgs boson with $m_H = 160$ GeV with a production rate of 2.2 times the SM value at 95% C.L. using a fit to the matrix element likelihood distribution with a power constraint applied.

In the future, there are many possible ways these results may be improved upon. The matrix element discriminant may be extended to include other backgrounds, in addition to the WW background. This should give additional separation power, allowing the sensitivity to be further improved. The matrix element likelihood may also be used as an input to a neural network or boosted decision tree to maximise the sensitivity.

The searches presented here represent the first steps at ATLAS to either discover or completely rule out the existence of the Higgs boson. More data are being recorded extremely rapidly as 2011 progresses. Amongst these data may be the first hints of the Higgs boson or something else entirely: the next few months will give a definitive answer, and have the potential to dramatically change our understanding of particle physics.

Bibliography

[1] Nakamura et al. "The review of particle physics". *J. Phys.*, **G37** (2010) 075201.

[2] F. Englert & R. Brout. "Broken Symmetry and the Mass of Gauge Vector Mesons". *Phys. Rev. Lett.*, **13** (1964) 321.

[3] P. W. Higgs. "Broken Symmetries, Massless Particles and Gauge Fields". *Phys. Lett.*, **12** (1964) 132.

[4] P. W. Higgs. "Broken Symmetries and the Masses of Gauge Bosons". *Phys. Rev. Lett.*, **13** (1964) 508.

[5] P. W. Higgs. "Spontaneous Symmetry Breakdown without Massless Bosons". *Phys. Rev.*, **145** (1966) 1156.

[6] G. S. Guralnik, C.R. Hagen & T.W.B. Kibble. "Global Conservation Laws and Massless Particles". *Phys. Rev. Lett.*, **13** (1964) 585.

[7] T.W.B. Kibble. *Phys. Rev.*, **155** (1967) 1554.

[8] S. Martin. "A supersymmetry primer". `arXiv:hep-ph/9709.356`

[9] A. Martin. "Technicolor signals at the LHC". `arXiv:hep-ph/0812.1841`

[10] ATLAS Collaboration. `http://atlas.ch/photos/lhc.html`

[11] L. Evans & P. Bryant. "LHC Machine". *JINST*, **3** (2008) S08001.

[12] CERN. `http://cdsweb.cern.ch/record/42384`

[13] LHC Collaboration. "LHC Conceptual Design Report". *CERN/AC/95-05*.

[14] CERN. "Interim summary report on the analysis of the 19 September 2008 incident at the LHC". `https://edms.cern.ch/file/973073/1/Report_on_080919_incident_at_LHC__2_.pdf`

[15] ATLAS Collaboration. "Observation of a Centrality-Dependent Dijet Asymmetry in Lead-Lead Collisions at $\sqrt{S_{NN}} = 2.76$ TeV with the ATLAS Detector at the LHC". *Phys. Rev. Lett.*, **105** (2010) 252303.

[16] ATLAS Collaboration. `https://twiki.cern.ch/twiki/bin/view/AtlasPublic/LuminosityPublicResults`

[17] ATLAS Collaboration. "The ATLAS Experiment at the CERN Large Hadron Collider". *JINST*, **3** (2008) S08003.

[18] DESY ATLAS group. "A picture of the ATLAS trigger system". `http://www-atlas.desy.de/general.html`

[19] ATLAS Collaboration. "Calorimeter Clustering Algorithms: Description and Performance". ATL-LARG-PUB-2008-002 (2008).

[20] S. Hassini et al. "A muon identification and combined reconstruction procedure for the ATLAS detector at the LHC using the (MUONBOY, STACO, MuTag) reconstruction packages". *NIM A*, **572** (2007) 77–79.

[21] M. Cacciari, G. P. Salam & G. Soyez. "Anti-KT jet clustering Algorithm". *JHEP*, **0804** (2008) 063.

[22] M. Cacciari & G. P. Salam. "Dispelling the N^3 myth for the Kt jet-finder". *Phys. Lett.*, **B641** (2006) 57.

[23] G. P. Salam M. Cacciari & G. Soyez. `http://fastjet.fr/`

[24] ATLAS Collaboration. "Luminosity determination in pp collisions at $\sqrt{s} = 7$ TeV using the ATLAS detector at the LHC". *Eur. Phys. J.*, **C71** (2011) 1630.

[25] ATLAS Collaboration. "ATLAS Forward Detectors for Luminosity Measurement and Monitoring". CERN/LHCC/2004-010 (2004).

[26] G.D. Rochester & C.C. Butler. "Evidence for the existence of new unstable elementary particles". *Nature*, **160**, 4077 (1947) 855.

[27] G.D. Rochester & C.C. Butler. "An example of meson production in lead". *Nature*, **159**, 4033 (1947) 227–228.

[28] C.M.G. Lattes, H. Muirhead, G.P.S. Occialini & C.F. Powell. "Processes involving charged mesons". *Nature*, **159** (1947) 694–697.

[29] C.M.G. Lattes, H. Muirhead, G.P.S. Occialini & C.F. Powell. "Observations on the tracks of slow mesons in photographic emulsions". *Nature*, **160** (1947) 453–456,486–492.

[30] E.D. Bloom et al. "High-energy inelastic $e-p$ scattering at 6° and 10°". *Phys. Rev. Lett.*, **23**, 16 (1969) 930–934.

[31] M. Breidenbach et al. "Observed behaviour of highly inelastic electron-proton scattering". *Phys. Rev. Lett.*, **23**, 16 (1969) 935–939.

[32] H.D. Politzer. "Reliable perturbative results for strong interactions?" *Phys. Rev. Lett.*, **30** (1973) 1346–1349.

[33] D.J. Gross & F. Wilczek. "Ultraviolet behavior of non-Abelian gauge theories". *Phys. Rev. Lett.*, **30** (1973) 1343–1346.

[34] D.J. Gross & F. Wilczek. "Asymptotically free gauge theories". *Phys. Rev.*, **D8** (1973) 3633–3652.

[35] S.L. Glashow. "Partial symmetries of weak interactions". *Nucl. Phys.*, **22** (1961) 579.

[36] S. Weinberg. "A model of leptons". *Phys. Rev. Lett.*, **19** (1967) 1264.

[37] H. Georgi & S.L. Glashow. "Unity of all elementary particle forces". *Phys. Rev. Lett.*, **32** (1974) 438.

[38] CDF Collaboration. "Search for Randall-Sundrum gravitons in the diphoton channel at CDF". *Phys. Rev.*, **D83** (2011) 011102.

[39] CDF Collaboration. "Search for new dielectron resonances and Randall-Sundrum gravitons at the Collider Detector at Fermilab" (2011). `http://www-cdf.fnal.gov/physics/exotic/r2a/20110214.gravitonee/index.html`

[40] D0 Collaboration. "Search for Randall-Sundrum gravitons in the dielectron and diphoton final states with 5.4 fb^{-1} of data from ppbar collisions at $\sqrt{s} = 1.96$ TeV". *Phys. Rev. Lett.*, **104** (2010) 241802.

[41] UA1 Collaboration. "Experimental observation of isolated large transverse energy electrons with associated missing energy at $\sqrt{s} = 540$ GeV". *Phys. Lett.*, **B122** (1983) 103.

[42] UA2 Collaboration. "Observation of single isolated electrons of high transverse momentum in events with missing transverse energy at the CERN pp collider". *Phys. Lett.*, **B122** (1983) 476.

[43] UA1 Collaboration. "Experimental observation of lepton pair of invariant mass around 95 GeV/C^2 at the CERN SPS collider". *Phys. Lett.*, **B126** (1983) 398–410.

[44] N.W. Ashcroft & N.D. Mermin. "Solid state physics". Holt, Rinehart and Winston (1978).

[45] Y. Nambu. "Quasiparticles and gauge invariance in the theory of superconductivity". *Phys. Rev.*, **117** (1960) 648–663.

[46] J. Goldstone. "Field theories with superconductor solutions". *Nuovo Cimento*, **19** (1961) 154–164.

[47] J. Goldstone, A. Salam & S. Weinberg. "Broken symmetries". *Phys. Rev.*, **127** (1962) 965–970.

[48] W.E. Burcham & M. Jobes. "Nuclear and particle physics". Longman Scientific and Technical (1995).

[49] P. Renton. "Electroweak interactions". Cambridge University Press (1990).

[50] Gribov. V.N. & L.N. Lipatov. "Deep inelastic *ep* scattering in perturbation theory". *Sov. J. Nucl. Phys.*, **15** (1972) 438–450.

[51] G. Altarelli & G. Parisi. "Asymptotic freedom in parton language". *Nucl. Phys.*, **B126** (1977) 298.

[52] Yu. L. Dokshitzer. "Calculation of the structure functions for deep inelastic scattering and e^+e^- annihilation by perturbation theory in quantum chromodynamics". *Sov. Phys. JETP*, **46** (1977) 641–653.

[53] J. Ellison & J. Wudka. "Study of trilinear gauge boson couplings at the Tevatron collider". *Ann. Rev. Nucl. Part. Chi.*, **48** (1998) 33.

[54] CDF Collaboration. "Measurement of the W^+W^- production cross section and search for anomalous $WW\gamma$ and WWZ couplings in $p\overline{p}$ collisions at $\sqrt{s} = 1.96$ TeV". *Phys. Rev. Lett.*, **104** (2010) 201801.

[55] S. Dittmaier et al. "Handbook of LHC Higgs cross sections". CERN-2011-002 (2011). `arXiv:hep-ph/1101.0593`

[56] A. Djouadi, J. Kalinowski & M. Spira. "HDECAY: A program for Higgs boson decays in the standard model and its supersymmetric extension". *Comput. Phys. Commun*, **108** (1998) 56–74.

[57] A. Djouadi, J. Kalinowski, M. Muehlleitner & M. Spira. "An update of the program HDECAY in the Les Houches 2009 workshop on TeV colliders: The tools and Monte Carlo working group summary report". `arXiv:hep-ph/1003.1643`

[58] D. Zanzi & S. Xella. "SM Higgs boson search in the $\tau^+\tau^-$ final state at 10 TeV in the ATLAS experiment". ATL-COM-PHYS-2011-036 (2011).

[59] ATLAS Collaboration. "ATLAS sensitivity prospects for Higgs boson production at the LHC running at 7, 8 or 9 TeV". ATL-PHYS-PUB-2010-015 (2010).

[60] R. Barate et al. "Search for the standard model Higgs boson at LEP". *Phys. Lett.*, **B565** (2003) 61–75.

[61] CDF & D0 Collaborations. "Combined CDF and D0 Upper Limits on Standard Model Higgs Boson Production with up to 8.2 fb^{-1} of Data". FERMILAB-CONF-11-044-E.

[62] S. Roth. "W mass at LEP and Standard Model fits". `arXiv:hep-ex/0605014`

[63] CDF & D0 Collaborations. "W mass and width measurements at the Tevatron" (2010). `arXiv:hep-ex/1011.3853`

[64] CDF & D0 Collaborations. "Combination of CDF and D0 results on the mass of the top quark using up to 5.6 fb^{-1} of data" (2010). `arXiv:hep-ex/1007.3178`

[65] H. Flaecher et al. "Revisiting the global electroweak fit of the Standard Model and beyond with Gfitter". *Eur. Phys. J.*, **C60**, 4 (2009) 543–583.

[66] The LEP electroweak working group, the Tevatron electroweak working group, the SLD electroweak & the SLD heavy flavour group. "2010 precision electroweak measurements and constraints on the Standard Model" (2010). `http://lepewwg.web.cern.ch/LEPEWWG`

[67] K. Melnikov & F. Petriello. "The W boson production cross section at the LHC through $O(\alpha_s^2)$". *Phys. Rev. Lett.*, **96** (2006) 231803.

[68] K. Melnikov & F. Petriello. "Electroweak gauge boson production at hadron colliders through $O(\alpha_S^2)$". *Phys. Rev.*, **D74** (2006) 114017.

[69] S. Catani, L. Cieri, G. Ferrera, D. de Florian & M. Grazzini. "Vector boson production at hadron colliders: a fully exclusive QCD calculation at NNLO". *Phys. Rev. Lett.*, **103** (2009) 082001.

[70] M. L. Mangano et al. "ALPGEN, a generator for hard multi-parton processes in hadronic collisions". *JHEP*, **07** (2003) 001.

[71] J. Alwall et al. "MadGraph/MadEvent v4: The New Web Generation". *JHEP*, **09** (2007) 028.

[72] T. Sjöstrand, S. Mrenna & P. Z. Skands. "PYTHIA 6.4 physics and manual". *JHEP*, **05** (2006) 026.

[73] S. Jadach et al. "The tau decay library TAUOLA, version 2.4". Comp. Phys. Comm. **76** (1993) 361.

[74] S. Frixione & B. Webber. `http://www.hep.phy.cam.ac.uk/theory/webber/MCatNLO/`

[75] T. Binoth, M. Ciccolini, N. Kauer & M. Krämer. "Gluon-induced W-boson pair production at the LHC". *JHEP*, **12** (2006) 046.

[76] T. Gleisberg et al. "Event generation with SHERPA 1.1". *JHEP*, **02** (2009) 007.

[77] S. Agostinelli et al. "GEANT 4, A Simulation Toolkit". *NIM A*, **506** (2003) 250–303.

[78] ATLAS Collaboration. "The ATLAS Simulation Infrastructure". *Eur. Phys. J.*, **C70** (2010) 823–874.

[79] ATLAS Collaboration. "Measurement of the $W \to l\nu$ and $Z/\gamma* \to ll$ production cross sections in proton-proton collisions at $\sqrt{s} = 7$ TeV with the ATLAS detector". *JHEP*, **1012** (2010) 060.

[80] ATLAS Collaboration. "Expected electron performance in the ATLAS experiment". ATL-COM-PHYS-2010-990 (2011).

[81] ATLAS Collaboration. "Calibrating the b-Tag and Mistag Efficiencies of the SV0 b-Tagging Algorithm in 3 pb^{-1} of Data with the ATLAS Detector". ATLAS-CONF-2010-099 (2010).

[82] ATLAS Collaboration. "Performance of the Missing Transverse Energy Reconstruction and Calibration in Proton-Proton Collisions at a Center-of-Mass Energy of $\sqrt{s} = 7$ TeV with the ATLAS Detector". ATLAS-CONF-2010-057 (2010).

[83] ATLAS Collaboration. "Measurement of the WW production cross section in proton-proton collisions at $\sqrt{s} = 7$ TeV with the ATLAS detector". ATLAS-CONF-2011-015 (2010).

[84] A. J. Barr, B. Gripaios & C. Lester. "Measuring the Higgs boson mass in dileptonic W-boson decays at hadron colliders". *JHEP*, **07** (2009) 072.

[85] ATLAS Collaboration. "Reconstruction of primary vertices in pp collisions at energies of 900 GeV and 7 TeV with the ATLAS detector". `arXiv:physics.ins-det/1010.1483`

[86] J. M. Campbell, E. Castaneda-Miranda, Y. Fang, N. Kauer, B. Mellado & S. L. Wu. "Normalizing Weak Boson Pair Production at the Large Hadron Collider". *Phys. Rev.*, **D80** (2009) 054023.

[87] ATLAS Collaboration. "Higgs Boson Searches using the $H \to WW \to l\nu l\nu$ Decay Mode with the ATLAS Detector at 7 TeV". ATLAS-CONF-2011-005 (2011).

[88] ATLAS Collaboration. "Expected electron performance in the ATLAS experiment". ATL-PHYS-PUB-2011-006 (2011).

[89] ATLAS Collaboration. "Determination of the muon reconstruction efficiency in ATLAS at the Z resonance in proton-proton collisons at $\sqrt{s} = 7$ TeV". To appear.

[90] ATLAS Collaboration. "Prospects for Higgs Boson Searches using the $H \to WW^{(*)} \to \ell\nu\ell\nu$ Decay Mode with the ATLAS Detector for 10 TeV". ATL-PHYS-PUB-2010-005 (2010).

[91] ATLAS Collaboration. "Observation of the Background from W+jets to the $H \to WW^{(*)} \to \ell\nu\ell\nu$ Search with the ATLAS detector at 7 TeV". ATLAS-CONF-2010-092 (2010).

[92] S.-C. Hsu. "A Study of the Standard Model Higgs, WW and ZZ Production in Dilepton plus Missing Transverse Energy Final State at CDF Run II". FERMILAB-THESIS-2008-61.

[93] CDF Collaboration. "Search for a Higgs Boson Decaying to Two W Bosons at CDF". *Phys. Rev. Lett.*, **102** (2009) 021802.

[94] G. Wooden, C. Hays & D. Whiteson. "A search for $H \to WW(*) \to \ell\nu\ell\nu$ at ATLAS optimised with a matrix-element-based likelihood". ATL-COM-PHYS-2010-1064 (2010).

[95] M. R. Whalley, D. Bourilkov & R. C. Group. "The Les Houches accord PDFs (LHAPDF) and LHAGLUE". `arXiv:hep-ph/0508110`

[96] P.M. Nadolsky, H.L. Lai, J. Huston, J. Pumplin, D.R. Stump & W.K. Tung. "CTEQ6L - LO with NLO α_S". *JHEP*, **0207** (2002) 012.

[97] D. Stump, J. Huston, J. Pumplin, W.K. Tung, H. Lai, S. Kuhlmann & J. Owens. "Inclusive jet production, parton distributions and the search for new physics". *JHEP*, **0310** (2003) 046.

[98] D. Hook & P. McAree. "Real Roots of Polynomial Equations" (1990). `http://tog.acm.org/GraphicsGems/gems/Sturm/`

[99] G. Cowan, K. Cranmer, E. Gross & O. Vitells. "Asymptotic formulae for likelihood-based tests of new physics". *Eur. Phys, J.*, **C71** (2010) 1554.

[100] ATLAS Collaboration. "Muon Momentum Resolution in First Pass Reconstruction of pp Collision Data Recorded by ATLAS in 2010". ATLAS-CONF-2011-046 (2011).

[101] ATLAS Collaboration. "Supporting Document: Measurement of the W cross section and asymmetry in the electron and muon decay channels at $\sqrt{s} = 7$ TeV". ATL-COM-PHYS-2010-477 (2010).

[102] ATLAS Collaboration. "Measurement of the $W \to \ell\nu$ production cross section and observation of $Z \to \ell\ell$ production in proton-proton collisions at $\sqrt{s} = 7$ TeV with the ATLAS detector". ATLAS-CONF-2010-051 (2010).

[103] J. Butterworth, E. Dobson, U. Klein, B. Mellado Garcia, T. Nunnemann, J. Qian, D. Rebuzzi & R. Tanaka. "Single Boson and Diboson Production Cross Sections in pp Collisions at $\sqrt{s}$=7 TeV". ATL-COM-PHYS-2010-695 (2010).

[104] ATLAS Collaboration. "W/Z+Jet Cross Section Measurements at the Large Hadron Collider". ATL-PHYS-PROC-2009-062.

[105] M. Groll. "Associated production of weak bosons at the LHC with the ATLAS detector". *J. Phys. Conf. Ser.*, **171** (2009) 012086.

[106] S. Moch & P. Uwer. "Theoretical status and prospects for top-quark pair production at hadron colliders". *Phys. Rev.*, **D78** (2008) 034003.

[107] ATLAS Collaboration. "Jet energy resolution and reconstruction efficiencies from in-situ techniques with the ATLAS detector using proton-proton collisions at a center of mass energy $\sqrt{s} = 7$ TeV". ATLAS-CONF-2010-054 (2010).

[108] ATLAS Collaboration. "Expected Performance of the ATLAS Experiment - Detector, Trigger and Physics". `arXiv:hep-ex/0901.0512`

[109] G.J. Feldman & R.D. Cousins. "Unified approach to the classical statistical analysis of small signals". *Phys. Rev.*, **D57** (1998) 3873–3889.

[110] CDF & D0 Collaborations. "Combined CDF and D0 upper limits on standard model Higgs boson production with up to 6.7 fb^{-1} of data". `arXiv:hep-ex/1007.4587`

[111] CDF & D0 Collaborations. "Combination of Tevatron searches for the standard model Higgs boson in the W^+W^- decay mode". *Phys. Rev. Lett.*, **104** (2010) 061802.

[112] A.L. Read. "Modified frequentist analysis of search results (the CL_S method)". CERN-OPEN-2000-205 (2010).

[113] L. Moneta et al. "The RooStats project" (2010). `arXiv:physics.data-an/1009.1003`